Monthly Notices of the ROYAL ASTRONOMICAL SOCIETY

MNRAS **474,** 961–1017 (2018) doi:10.1093/mnras/stx2679
Advance Access publication 2017 October 13

Systematic study of magnetar outbursts

Francesco Coti Zelati,[1,2,3,4★] Nanda Rea,[1,2] José A. Pons,[5] Sergio Campana[3] and Paolo Esposito[2]

[1]*Institute of Space Sciences (IEEC–CSIC), Campus UAB, Carrer de Can Magrans, E-08193 Barcelona, Spain*
[2]*Anton Pannekoek Institute for Astronomy, University of Amsterdam, Postbus 94249, NL-1090-GE Amsterdam, the Netherlands*
[3]*INAF – Osservatorio Astronomico di Brera, via Bianchi 46, I-23807 Merate (LC), Italy*
[4]*Dipartimento di Scienza e Alta Tecnologia, Università dell'Insubria, via Valleggio 11, I-22100 Como, Italy*
[5]*Departament de Física Aplicada, Universitat d'Alacant, Ap. Correus 99, E-03080 Alacant, Spain*

Accepted 2017 October 11. Received 2017 October 11; in original form 2017 August 1

ABSTRACT

We present the results of the systematic study of all magnetar outbursts observed to date, through a reanalysis of data acquired in about 1100 X-ray observations. We track the temporal evolution of the outbursts' soft X-ray spectral properties and the luminosities of the single spectral components as well as of the total emission. We model empirically all outburst light curves, and estimate the characteristic decay time-scales as well as the energetics involved. We investigate the link between different parameters (e.g. the luminosity at the peak of the outburst and in quiescence, the maximum luminosity increase, the decay time-scale and energy of the outburst, the neutron star surface dipolar magnetic field and characteristic age, etc.), and unveil several correlations among these quantities. We discuss our results in the context of the internal crustal heating and twisted bundle models for magnetar outbursts. This study is complemented by the Magnetar Outburst Online Catalogue (http://magnetars.ice.csic.es), an interactive data base where the user can plot any combination of the parameters derived in this work, and download all data.

Key words: methods: data analysis – methods: observational – techniques: spectroscopic – stars: magnetars – stars: magnetic field – X-rays: stars.

1 INTRODUCTION

Magnetars are strongly magnetized (up to $B \sim 10^{14}$–10^{15} G) isolated X-ray pulsars with luminosities $L_X \sim 10^{31}$–10^{36} erg s^{-1}. They rotate at comparatively long periods ($P \sim 0.3$–12 s) with respect to the general pulsar population, and are typically characterized by large secular spin-down rates ($\dot{P} \sim 10^{-15}$ to 10^{-10} s s^{-1}). According to the magnetar scenario, their emission is ultimately powered by the decay and the instability of their ultra-strong magnetic field (e.g. Duncan & Thompson 1992; Paczyński 1992; Thompson & Duncan 1993, 1995, 1996, 2001; see Turolla, Zane & Watts 2015; Kaspi & Beloborodov 2017, for recent reviews). The hallmark of magnetars is the unpredictable and highly variable bursting/flaring activity in the X-/gamma-ray energy range, which encompasses a wide interval of time-scales (from a few milliseconds up to tens of seconds) and luminosities (10^{39}–10^{47} erg s^{-1} at the peak; Turolla et al. 2015). The bursting episodes are often accompanied by large and rapid enhancements of the persistent X-ray emission (typically by a factor of ∼10–1000), which then decline and attain the quiescent level on a time-scale ranging from a few weeks up to several years. We will refer to these phases as outbursts, to distinguish from the bursting/flaring activity (see Rea & Esposito 2011, for an observational review).

At the moment of writing (2017 July), 26 isolated X-ray pulsars have unambiguously shown magnetar-like activity, including the rotation-powered pulsars PSR J1846−0258 and PSR J1119−6127 (Gavriil et al. 2008; Kumar & Safi-Harb 2008; Kuiper & Hermsen 2009; Archibald et al. 2016a; Göğüş et al. 2016; Archibald et al. 2017a), the low-field magnetars SGR 0418+5729 and Swift J1822.3−1606 (e.g. Rea et al. 2010, 2012a), and the central compact object 1E 161348−5055 (D'Aì et al. 2016; Rea et al. 2016). These discoveries demonstrate how magnetar activity might have a larger spread within the neutron star population.

The soft X-ray ($\lesssim$10 keV) emission of magnetars is typically well described by a combination of a thermal component (a blackbody with temperature $kT \sim 0.3$–0.9 keV) plus a power law with photon index $\Gamma \sim 2$–4, commonly interpreted in terms of repeated resonant cyclotron up-scattering of thermal photons from the star surface on to charged particles flowing in a twisted magnetosphere (e.g. Thompson, Lyutikov & Kulkarni 2002; Nobili, Turolla & Zane 2008a,b). In some cases, a multiple-blackbody model provides an adequate description as well, and it is usually ascribed to thermal emission from regions of different temperature and

★E-mail: francesco.cotizelati@brera.inaf.it

size on the star surface (e.g. Tiengo, Esposito & Mereghetti 2008; Alford & Halpern 2016).

In the last decades and especially following the advent of the new generation of imaging instruments on board *Swift*, *Chandra* and *XMM–Newton*, several magnetar outbursts were monitored in the X-rays, leading to a number of unexpected breakthroughs which have changed our understanding of these strongly magnetized neutron stars (Turolla et al. 2015; Kaspi & Beloborodov 2017). The large field of view (FoV) and the fast response of the *Swift* satellite proved (and still prove) to be key ingredients to spot the bursting/flaring activity of magnetars and precisely track spectral variations since the very first active phases and on time-scales ranging from days to months. *Chandra* and *XMM–Newton* have revealed to be of paramount importance to characterize adequately the X-ray emission of faint outbursts particularly at later stages, thanks to dedicated follow-up observational programmes and the large collecting area of their instruments. In some cases, the monitoring campaigns covered the whole outburst evolution, and disclosed the source quiescent level. Although the cooling pattern varies significantly from outburst to outburst, the spectral softening throughout the decay seems an ubiquitous characteristic for these events (Rea & Esposito 2011).

1.1 Magnetar outbursts: mechanisms

Although it is widely accepted that magnetar outbursts are attributable to some form of heat deposition in a restricted region of the star surface which then cools, the mechanism responsible for their activation, as well as the energy supply responsible for sustaining their long-term emission, still remain somewhat elusive. They are probably triggered by local internal magnetic stresses strong enough to deform irreversibly part of the stellar crust, possibly in the form of a prolonged avalanche of plastic failures (Li, Levin & Beloborodov 2016). An additional contribution may be provided by magnetospheric Alfvén waves created during flaring activity (Parfrey, Beloborodov & Hui 2013). According to Li & Beloborodov (2015), these waves are impulsively transmitted inside the star, and induce a strong oscillating plastic flow in the crust that subsists for a few ms, after which the waves are damped.

Regardless of the triggering mechanism, the plastic flows induced in the crust lead to transient thermoplastic waves that move the crust, convert mechanically its magnetic energy into heat and relieve the stresses (Beloborodov & Levin 2014). A fraction of the deposited heat is then conducted up to the surface and radiated, producing a delayed thermal afterglow emission that can be sustained up to a few years, also depending on the flare rate (see also Beloborodov & Li 2016). The crustal cooling time-scale chiefly depends on the thermal properties of the outer crust, the depth at which the energy is released and the neutrino emission processes operating in the crust (Pons & Rea 2012; Li et al. 2016). Moreover, the crustal displacements implant a strong external magnetic twist, presumably confined to a bundle of current-carrying closed field lines anchored in the crust. Additional heating of the surface layers is then produced as the currents flowing along the field lines of the twisted bundle impact upon the star (e.g. Thompson et al. 2002; Beloborodov & Thompson 2007; Beloborodov 2009). As the energy reservoir stored in the star interior is progressively depleted, the twist must decay to support its currents. Consequently, the spatial extent of the bundle gets gradually more and more limited, the area on the star surface hit by the charges shrinks and the luminosity decreases. The time-scale of the resistive untwisting can be of the order of a few years if the crustal motions take place at high latitudes and the footpoints of the bundle are positioned close to the magnetic poles (Beloborodov 2009).

Both heating mechanisms – internal and external – are likely at work during outbursts.

1.2 Motivation of the study and plan of the paper

Although several detailed studies were conducted for each of these events, an overall systematic and homogeneous analysis of the spectral properties of these stars, from the very first active phases of their outbursts throughout their decays, is still missing. A systematic reanalysis of all data sets is required to compare properly these properties, model accurately the outbursts cooling curves in a consistent way and unveil possible correlations among different parameters such as maximum luminosity, quiescent luminosity, luminosity increase during the outburst, energetics, decay time-scale, magnetic field, rotational energy loss rate and age.

This paper presents the results of the X-ray spectral modelling for 23 magnetar outbursts from 17 different sources using all the available data acquired by the *Swift*, *Chandra* and *XMM–Newton* X-ray observatories, as well as data collected in a handful of observations by the instruments aboard *BeppoSAX*, *Roentgen Satellite* (*ROSAT*) and *RXTE*. This sums up to about 1100 observations, for a total dead-time corrected on source exposure time of more than 12 Ms. The paper is structured as follows: in Section 2 we introduce the sample of magnetars considered in this study, and the monitoring campaigns that were activated following the detection of their outbursts. In Section 3 we describe the data reduction and extraction procedures. In Section 4 we report details on the spectral analysis. In Section 5 we exploit the results of our analysis to extract the light curves for each outburst and estimate the outburst energetics and decay time-scale. In Section 6 we report on accurate estimates of peak and quiescent luminosities of magnetars, including those showing only subtle variability on top of their persistent emission. In Section 7 we present the results of a search for possible (anti)correlations between several different parameters. In Section 8 we discuss the results of our study. A brief description of the Magnetar Outburst Online Catalogue (MOOC) follows in Section 9. The results of the detailed modelling of the outbursts evolution with physically motivated models will be presented in a forthcoming work.

2 THE SAMPLE

This section summarizes the properties of the 17 magnetars that so far have undergone at least one outburst. The sources are listed according to the chronological order of their (first) outburst activation, except for the three sources PSR J1119−6127, PSR J1846−0258 and 1E 161348−5055, which are described at the end of the section. Details about the prompt and follow-up X-ray observations used in this work are reported in a series of tables in Appendix A. In the following, all the values reported for the magnetic field are computed using the spin-down formula for force-free magnetospheres by Spitkovsky (2006), and assuming an aligned rotator. They refer to the dipolar component of the magnetic field at the polar caps (this is a factor of ∼2 larger than the value computed at the equator).

2.1 SGR 1627−41

SGR 1627−41 was discovered on 1998 June 15 (Kouveliotou et al. 1998), when three consecutive bursts were detected by the Burst and Transient Source Experiment (BATSE) aboard the

Compton Gamma Ray Observatory. More than 100 bursts were recorded from the same location within the subsequent 6 weeks, and the X-ray counterpart was identified 2 months later by the narrow field instruments on board *BeppoSAX* (Woods et al. 1999). The burst detections marked the onset of an outburst, which gradually recovered the quiescent level over the course of the ensuing decade (see Table A1).

On 2008 May 28 the Burst Alert Telescope (BAT; Barthelmy et al. 2005) aboard *Swift* triggered on dozens of bursts from SGR 1627−41 (Palmer et al. 2008). A conspicuous enhancement of the persistent X-ray flux was measured (a factor of about 100 larger with respect to 3 months and a half before), and the magnetar nature of the source was incontrovertibly settled with the detection of 2.59-s X-ray pulsations in *XMM–Newton* data sets (with $\dot{P} \sim 1.9 \times 10^{-11}$ s s^{-1}; Esposito et al. 2009b). Table A2 reports the log of the X-ray observations carried out after the second outburst. We assume a distance of 11 kpc throughout the paper.

2.2 1E 2259+586

After more than two decades of rather persistent X-ray emission since its discovery at the centre of the supernova remnant (SNR) G109.1−1.0 (CTB 109) in 1979 December (Fahlman & Gregory 1981), the 6.98-s X-ray pulsar 1E 2259+586 attracted attention on 2002 June 18, when more than 80 bursts were detected within 3 h of observing time by the *Rossi X-ray Timing Explorer* (*RXTE*), and the persistent flux rose by a factor of ∼10 compared to the quiescent level (Kaspi et al. 2003). Eight *XMM–Newton* observations were carried out to study the subsequent evolution of the outburst (see Table A3).

Nearly 10 yr later, on 2012 April 21, the Gamma-ray Burst Monitor (GBM) on board *Fermi* triggered on a single 40-ms long event (Foley et al. 2012), which was accompanied by an increase in the soft X-ray flux (as observed about a week later by the X-ray Telescope (XRT) on board *Swift*; see Table A4 for a journal comprising this and all the follow-up observations of the first ∼1400 d since the outburst onset). We assume a distance of 3.2 kpc throughout the paper.

2.3 XTE J1810−197

Originally a soft and faint X-ray source serendipitously recorded by the *ROSAT* during four observations between 1991 and 1993, the transient nature of XTE J1810−197 was disclosed in 2003, when the *RXTE* detected it at an X-ray flux a factor about 100 larger with respect to the pre-outburst level. X-ray pulsations were measured at a period of 5.54 s (Ibrahim et al. 2004). Radio pulsations at the spin period were detected in 2006 (about 3 yr later), a property never observed before in any other magnetar, which definitely proved that pulsed radio emission could be produced even in sources with magnetar-strength fields (Camilo et al. 2006). Although the initial phases of the outburst were missed, XTE J1810−197 has been studied in great detail over the last 12 yr, especially with the *XMM–Newton* observatory and up to the return to quiescence (see Table A5).[1] We assume a distance of 3.5 kpc throughout the paper.

[1] The source was observed also with *Chandra* for 12 times and with *Swift* for 5 times. We focus here on the *XMM–Newton* pointings alone, because they provide a good coverage of the whole outburst evolution down to the quiescent level, as well as the spectra with the largest counting statistics. Note that a recent *Swift* XRT observation performed in 2017 February caught the source again at the historical quiescent flux.

2.4 SGR 1806−20

Initially catalogued as a classical γ-ray burst (GRB 790107) based on observations by the *Konus* experiment (Mazets et al. 1981) and other all-sky monitors of the interplanetary network (Laros et al. 1986), SGR 1806−20 was recognized to be a member of a distinct class of astrophysical transients after the detection of more than 100 bursts of soft γ-rays between 1979 and 1986 (Laros et al. 1987). Two observations were carried out by the *Advanced Satellite for Cosmology and Astrophysics* (*ASCA*) soon after an intense bursting activity in 1993 October (as unveiled by BATSE), leading to the identification of a previously uncatalogued, persistent, point-like X-ray counterpart (Murakami et al. 1994; Sonobe et al. 1994). The spin period, ∼7.5 s, was measured in 1996 November by means of five *RXTE* observations that were performed following another reactivation of the source (Kouveliotou et al. 1998).

SGR 1806−20 experienced an exceptionally intense flare on 2004 December 27 with a peak luminosity of a few 10^{47} erg s^{-1} (for a distance of 8.7 kpc and under the assumption of isotropic emission; Hurley et al. 2005; Palmer et al. 2005), which then decayed by a factor of ∼50 per cent, and stabilized at an approximately steady level over the subsequent 7 yr (Younes, Kouveliotou & Kaspi 2015). Table A6 reports a log of all 10 *XMM–Newton* observations tracking the post-flare evolution (no *Swift* observations were performed during the first 2 months of the outburst). We assume a distance of 8.7 kpc throughout the paper.

2.5 CXOU J164710.2−455216

CXOU J164710.2−455216 was discovered in 2005 during an X-ray survey of the young cluster of massive stars Westerlund 1, and tentatively identified as a magnetar candidate based on the value of its spin period, 10.61 s, and the X-ray spectral properties (Muno et al. 2006). The case was clinched the following year, when a rather intense burst lasting about 20 ms was fortuitously detected by the *Swift* BAT from the direction of the source, on 2006 September 21 (Krimm et al. 2006). This episode was indeed associated with an abrupt enhancement of the X-ray flux, which marked the onset of a magnetar-like outburst. Table A7 reports a summary of all follow-up X-ray observations.

The source underwent another weaker outburst on 2011 September 19, when four more sporadic bursts were detected from the source position (Baumgartner et al. 2011; Rodríguez Castillo et al. 2014). Table A8 lists the few X-ray observations of this outburst. We assume a distance of 4 kpc throughout the paper.

2.6 SGR 0501+4516

SGR 0501+4516 joined the magnetar family on 2008 August 22, after the *Swift* BAT detection of a series of short bursts of soft γ-rays (<100 keV; Barthelmy et al. 2008) and the discovery of pulsations at a period of 5.76 s from the X-ray counterpart (Göğüş, Woods & Kouveliotou 2008). The source continued to be active over the following 36 h, showing a total of about 30 bursts. It was soon recognized that the bursting activity was related to the onset of an outburst, and several X-ray observations were promptly undertaken (see Table A9). We assume a distance of 1.5 kpc throughout the paper.

2.7 1E 1547−5408

Discovered by the *Einstein* satellite on 1980 March 2 during a search for X-ray counterparts of unidentified γ-ray sources (Lamb & Markert 1981), 1E 1547−5408 (aka SGR 1550−5418) was later suspected to be a magnetar candidate based on its X-ray spectral properties, the observed long-term X-ray variability between 1980 and 2006, and its putative association with the SNR G327.24−0.13 (Gelfand & Gaensler 2007). The 'smoking gun' in favour of this classification came with the measurement of 2.07-s pulsations from the radio counterpart (Camilo et al. 2007), later confirmed also in the X-rays (Halpern et al. 2008).

On 2008 October 3, the *Swift* BAT triggered on and localized a short burst from a position consistent with that of 1E 1547−5408 (Krimm et al. 2008). *Swift* executed a prompt slew, and the XRT started observing the field only 99 s after the BAT trigger, catching the source at a flux a factor about 20 above that in quiescence (see Table A10 for the log of all the follow-up X-ray observations).

No further bursts were reported until 2009 January 22, when the source resumed a new state of extreme bursting activity (Connaughton & Briggs 2009; Gronwall et al. 2009), culminating in a storm of more than 200 soft γ-ray bursts recorded by the *International Gamma-Ray Astrophysics Laboratory* (*INTEGRAL*) in a few hours (Mereghetti et al. 2009), and characterized by a considerable increase in the persistent X-ray flux. The source was repeatedly observed in the X-rays after the burst trigger (especially with *Swift*), leading to one of the most intensive samplings of a magnetar outburst ever performed (see Table A11).[2] We assume a distance of 4.5 kpc throughout the paper.

2.8 SGR 0418+5729

SGR 0418+5729 was discovered after the detection of a couple of short hard X-ray bursts on 2009 June 5 with *Fermi* GBM and other instruments sensitive to the hard X-ray range (van der Horst et al. 2010). Coherent X-ray pulsations were observed at a period of 9.1 s 5 d later during an *RXTE* pointing (Göğüş, Woods & Kouveliotou 2009). Since then, *Swift*, *Chandra* and *XMM–Newton* observed the field of the new source for a total of 39 pointings (see Table A12). It took more than 3 yr of continuous monitoring to establish unambiguously the first derivative of the spin period, making this source the magnetar with the lowest inferred surface dipolar magnetic field known to date, $\sim 1.2 \times 10^{13}$ G (Rea et al. 2013a). We assume a distance of 2 kpc throughout the paper.

2.9 SGR 1833−0832

SGR 1833−0832 was discovered on 2010 March 19, when the *Swift* BAT triggered on and localized a short (<1 s) hard X-ray burst in a region close to the Galactic plane (Gelbord et al. 2010; Göğüş et al. 2010a) and the fast slew of the XRT promptly detected a previously unnoticed 7.57-s X-ray pulsator (Esposito et al. 2011; Göğüş et al. 2010a). Starting right after its discovery, *Swift* and *XMM–Newton* pointed their instruments towards the source multiple times for the first $\sim$160 d of the outburst decay (see Table A13). We assume an arbitrary distance of 10 kpc throughout the paper.

2.10 Swift J1822.3−1606

On 2011 July 14, the detection of a magnetar-like burst by the *Swift* BAT and of an associated bright and persistent XRT counterpart heralded the existence of a new magnetar, Swift J1822.3−1606 (Cummings et al. 2011), with a spin period of 8.43 s (Göğüş, Kouveliotou & Strohmayer 2011a). Swift J1822.3−1606 was densely monitored in the X-rays until 2012 November 17, covering a time span of $\sim$1.3 yr (see Table A14). With an estimated surface dipolar magnetic field of $\sim 6.8 \times 10^{13}$ G (Rodríguez Castillo et al. 2016, and references therein), it also belongs to the sub-class of the so called 'low-$\dot{P}$ magnetars'. We assume a distance of 1.6 kpc throughout the paper.

2.11 Swift J1834.9−0846

The BAT aboard *Swift* was triggered by a short SGR-like burst on 2011 August 7 (D'Elia et al. 2011). This episode was not isolated: a second burst from the same direction on the sky was recorded by the *Fermi* GBM approximately 3.3 h later (Guiriec, Kouveliotou & van der Horst 2011), and another similar event triggered the BAT again on August 29 (Hoversten et al. 2011). The magnetar nature of this newly discovered source was nailed down with the discovery of pulsations at 2.48 s from the X-ray counterpart (Göğüş & Kouveliotou 2011). *Swift*, *Chandra* and *XMM–Newton* observed this new SGR for a total of 25 times since the first burst detection (see Table A15).

Swift J1834.9−0846 represents a unique case among magnetars. It is indeed embedded in a patch of diffuse X-ray emission with a complex spatial structure consisting of a symmetric component within $\sim$50 arcsec around the magnetar, and an asymmetric component stretched towards the south–west of the point source and extending up to $\sim$150 arcsec. The former was interpreted as a halo created by the scattering of X-rays by intervening dust (dust-scattering halo; Kargaltsev et al. 2012; Esposito et al. 2013). The latter was attributed to a magnetar-powered wind nebula based on its highly absorbed power-law-like X-ray spectrum, the flux constancy and the absence of statistically significant variations in the spectral shape over a time span of 9 yr, between 2005 and 2014 (Younes et al. 2016). Swift J1834.9−0846 would then provide the first observational evidence for the existence of wind nebulae around magnetically powered pulsars (see also Granot et al. 2017; Torres 2017). We assume a distance of 4.2 kpc throughout the paper.

2.12 1E 1048.1−5937

The discovery of 1E 1048.1−5937 dates back to 1979 July 13, when *Einstein* detected 6.44-s pulsed X-ray emission from a point-like source in the Carina Nebula (Seward, Charles & Smale 1986). With five long-term outbursts shown to date, this source holds the record as the most prolific outbursting magnetar hitherto known. The first three flux enhancements were observed in 2001, 2002 and 2007 by *RXTE*, which monitored this source about twice per month from 1999 February to 2011 December (see

[2] *Swift* and *XMM–Newton* observations performed from 2007 June to October caught the magnetar while recovering from another outburst likely occurred prior to 2007 June (Halpern et al. 2008). We do not include the analysis of this outburst in this study owing to the unknown epoch of the episode onset and the sparse X-ray coverage. Our analysis of the 2009 event is limited to the first 1000 d of the outburst, but the source is currently being observed by *Swift*. However, a preliminary extraction of the long-term light curve with the *Swift* online tool (see below), reveals an extremely slow decay which is consistent with the extrapolation of our long-term light curve, giving no significant differences in the estimate of the total energetics and decay time-scale.

Dib & Kaspi 2014, and references therein). An additional flux increase was observed in 2011, and the subsequent evolution was the object of a prolonged monitoring campaign with *Swift*, to which two *Chandra* and one *XMM–Newton* observations have to be added (see Table A16 for the observations of the first ∼1000 d of the outburst decay). The last outburst from this source dates back to 2016 July 23 (Archibald et al. 2016b), and its evolution was again densely monitored thanks to the ongoing *Swift* campaign (see Table A17). The outbursts are remarkably periodic, with a recurrence time of about 1800 d (Archibald et al. 2015). In this study we focus on the last two outbursts. We assume a distance of 9 kpc throughout the paper.

2.13 SGR 1745−2900

At a projected separation of ∼0.1 pc from the supermassive black hole at the Centre of the Milky Way, Sagittarius A* (hereafter Sgr A*), the magnetar SGR 1745−2900 is the closest neutron star to a black hole ever observed, and it spins at a period of about 3.76 s (e.g. Coti Zelati et al. 2015a, 2017). According to numerical simulations and to the recently detected proper motion, it is likely in a bound orbit around Sgr A* (Rea et al. 2013b; Bower et al. 2015).

SGR 1745−2900 is the object of an ongoing intensive monitoring campaign by *Chandra* (see Table A18), still more than 3 yr after the detection of the first ∼30 ms long soft gamma-ray burst from the source on 2013 April 25 (Kennea et al. 2013a). We assume a distance of 8.3 kpc throughout the paper.

2.14 SGR 1935+2154

The most recent addition to the magnetar class is represented by SGR 1935+2154, whose existence was announced on 2014 July 5 once more through the detection of low-Galactic latitude short bursts by *Swift* BAT (Stamatikos et al. 2014). A deep follow-up observation carried out by *Chandra* enabled to determine its spin period (3.24 s; Israel et al.2014), and the post-outburst behaviour was then observed with *Swift*, *Chandra* and *XMM–Newton*. On 2015 February 22 the BAT triggered on another burst from the source (D'Avanzo et al. 2015), which led to further monitoring through 14 observations with *Swift* and two with *XMM–Newton*. Another 50-ms long burst was detected in 2015 December by *INTEGRAL* in the soft gamma rays (Mereghetti et al. 2015), albeit no concurrent increase in the X-ray emission over the long-term behaviour was observed (Coti Zelati et al. 2015b). The source reactivated once more on 2016 May 16 (Barthelmy et al. 2016), and bursting activity was observed over the following ∼5 d. Some of these flux enhancements were recently studied in detail by Younes et al. (2017). See Table A19 for the log of the observations. We assume a distance of 9 kpc throughout the paper.

2.15 PSR J1119−6127

The 0.4-s radio pulsar PSR J1119−6127 was discovered in the *Parkes* multibeam 1.4-GHz survey (Camilo et al. 2000), and it is likely associated with the SNR G292.2−0.5 (Crawford et al. 2001). The dipolar surface magnetic field implied by the timing parameters is about 8.2×10^{13} G, among the highest known among radio pulsars. On 2016 July 27 and 28 two magnetar-like bursts signalled the onset of an outburst from this source (Archibald et al. 2016a; Kennea et al. 2016; Younes, Kouveliotou & Roberts 2016). Table A20 lists the follow-up *Swift* observations analysed in this work. Interestingly, simultaneous radio and X-ray observations about 1 month after the outburst onset revealed a significant anticorrelation between the emission in the two bands: the rotation-powered radio emission switched off during periods of multiple magnetar-like X-ray bursts (Archibald et al. 2017a). We assume a distance of 8.4 kpc throughout the paper.

2.16 PSR J1846−0258

PSR J1846−0258 is a young (<1 kyr) rotation-powered pulsar located at the centre of the SNR Kesteven 75 (Gotthelf et al. 2000). It rotates at a period of ∼326 ms (Livingstone et al. 2011a) and is endowed with a surface dipolar magnetic field of $\sim 1 \times 10^{14}$ G, which is higher than the vast majority of rotation-powered pulsars. On 2006 June 8 several magnetar-like X-ray bursts were detected in the time series of the *RXTE* data sets, and a sudden X-ray outburst took place (Gavriil et al. 2008; see also Kumar & Safi-Harb 2008; Kuiper & Hermsen 2009). The source then returned to the quiescent state in about 6 weeks. In this study we will adopt the values estimated by Gavriil et al. (2008) for the total energy released during the outburst, as well as the time-scale of the decay (see Table 1). We assume a distance of 6 kpc throughout the paper.

2.17 1E 161348−5055

The source 1E 161348−5055 near the geometrical centre of the SNR RCW 103 defied any interpretation for more than two decades because of its puzzling phenomenology (in particular, a periodicity at 6.67 h and the lack of an optical/infrared counterpart; De Luca et al. 2006, 2008). On 2016 June 22, the *Swift* BAT detected a magnetar-like burst from 1E 161348−5055, also coincident with a large long-term X-ray outburst (D'Aì et al. 2016). The long-term light curve of the source from 1999 to 2016 July was already extracted by Rea et al. (2016; see in particular their fig. 2) in a way completely consistent with the procedure reported in this work for the other magnetar outbursts, and shows that the source experienced another major outburst in 2000 February. In the following, we will thus refer to that publication when quoting our estimates for the energetics and decay time-scale for the first outburst. On the other hand, the *Swift* XRT monitoring campaign of this object is ongoing on a monthly cadence and we are currently tracking the decay of the second outburst to refine the time-scale and energetics of this episode. The outburst is showing a slower evolution with respect to that we predicted in Rea et al. (2016), and in the following we will consider our updated values for the energetics and time-scales (up to mid-July 2017; see Table 1). We assume a distance of 3.3 kpc throughout the paper.

3 DATA REDUCTION AND EXTRACTION

This section describes the standard procedures employed to extract the scientific products (source and background spectra) and create or assign the response and auxiliary files starting from the raw *Swift*, *XMM–Newton* and *Chandra* data files publicly available. In addition to these data sets, we also looked at other few observations carried out with the Medium-Energy Concentrator Spectrometer (MECS; Boella et al. 1997) on board *BeppoSAX*, the *ROSAT* Position Sensitive Proportional Counter (PSPC; Pfeffermann et al. 1987), and the Proportional Counter Array (PCA; Jahoda et al. 2006) instrument of the *RXTE*. In particular, we focused on the data concerning the quiescent stages (pre-outburst observations), or the very early phases, of the outbursts. These data sets revealed to be crucial to

Table 1. Results of the empirical modelling of the outburst decays for the 0.3–10 keV luminosities of the single spectral components (BB, PL, BB1, BB2, BB3) and for the total bolometric thermal luminosities. The cooling curves were fitted with one or multiple exponential functions plus a constant (see the text for details). Uncertainties on the best-fitting parameters are quoted at the 1σ c.l. for a single parameter of interest. The total outburst energy is also reported. The values for PSR J1846−0258 and the first outburst of 1E 161348−5055 are taken from Gavriil et al. (2008), Rea et al. (2016), respectively. The values for the second outburst of 1E 161348−5055 are taken from the ongoing *Swift* XRT monitoring campaign.

Source	Component	Best-fitting decay model	τ (d)	$\tau_1/\tau_2/\tau_3$ (d)	E (erg)
SGR 1627−41 (1998)	BB/bol	2EXP	–	234^{+37}_{-38} / 1307^{+373}_{-245}	2×10^{42}
1E 2259+586 (2002)	BB1	EXP	1.41 ± 0.05	–	–
	BB2	EXP	47^{+40}_{-16}	–	–
	bol	EXP	21 ± 13	–	10^{41}
XTE J1810−197	BB1	EXP	376^{+72}_{-58}	–	–
	BB2	EXP	372^{+33}_{-29}	–	–
	bol	EXP	328^{+44}_{-38}	–	4×10^{42}
SGR 1806−20	bol	EXP	349 ± 52	–	2×10^{43}
CXOU J1647−4552 (2006)	BB	3EXP	–	2.9 ± 0.7 / 91^{+54}_{-27} / 225^{+32}_{-57}	–
	PL	2EXP	–	3 ± 1 / 458^{+64}_{-60}	–
	bol	3EXP	–	$2.4^{+0.8}_{-0.6}$ / 53 ± 3 / 238^{+13}_{-17}	10^{42}
SGR 1627−41 (2008)	BB/bol	3EXP	–	$0.56^{+0.07}_{-0.06}$ / 31^{+5}_{-4} / 508^{+45}_{-43}	10^{42}
SGR 0501+4516	BB	EXP	33 ± 2	–	–
	PL	2EXP	–	9^{+3}_{-2} / 345^{+68}_{-51}	–
	bol	2EXP	–	13 ± 2 / 147^{+12}_{-11}	9×10^{40}
1E 1547−5408 (2009)	BB	2EXP	–	$4.8^{+0.7}_{-0.6}$ / 1131^{+156}_{-120}	–
	PL	EXP	364 ± 15	–	–
	bol	3EXP	–	3 ± 1 / 109 ± 8 / 2870^{+528}_{-416}	2.4×10^{43}
SGR 0418+5729	BB/bol	EXP	76 ± 1	–	8×10^{40}
SGR 1833−0832	BB/bol	EXP	128^{+26}_{-4}	–	10^{42}
Swift J1822.3−1606	BB	3EXP	–	$0.78^{+0.4}_{-0.3}$ / $16.7^{+1.0}_{-0.9}$ / 207^{+12}_{-11}	–
	PL	2EXP	–	14.6 ± 0.8 / 817^{+54}_{-47}	–
	bol	3EXP	–	7 ± 2 / 28^{+4}_{-3} / 460^{+35}_{-31}	3×10^{41}
Swift J1834.9−0846	BB/bol	2EXP	–	0.08 ± 0.01 / 17.7 ± 0.4	2×10^{41}
CXOU J1647−4552 (2011)	BB/bol	EXP	47 ± 16	–	6×10^{40}
1E 1048.1−5937 (2011)	BB/bol	2EXP	–	39^{+26}_{-16} / 382^{+45}_{-31}	8×10^{42}
1E 2259+586 (2012)	BB1	EXP	79^{+59}_{-35}	–	–
	BB2	EXP	33.7^{+9}_{-8}	–	–
	bol	EXP	206^{+115}_{-74}	–	3×10^{41}
SGR 1745−2900	BB/bol	2EXP	–	81^{+6}_{-20} / 324^{+27}_{-17}	10^{43}
1E 1048.1−5937 (2016)	BB/bol	2EXP	–	42^{+8}_{-6} / 264^{+30}_{-29}	4×10^{42}
PSR J1119−6127	bol	3EXP	–	0.25 ± 0.06 / 18 ± 2 / 73 ± 2	8.5×10^{41}
PSR J1846−0258	bol	EXP	56 ± 6	–	4.5×10^{41}
1E 161348−5055 (2000)	bol	2EXP	–	110^{+13}_{-15} / 856^{+29}_{-27}	10^{43}
1E 161348−5055 (2016)	bol	2EXP	–	$0.5^{+0.2}_{-0.1}$ / 507^{+59}_{-49}	2.6×10^{42}

estimate fluxes and luminosities for the magnetar XTE J1810−197 during quiescence or for other magnetars (i.e. SGR 1627−41 during its 1998 event and SGR 0418+5729) at the very early stages of the outburst decay, and were reduced and analysed as described by Esposito et al. (2008, 2010a) and Rea et al. (2009, 2012a).

3.1 *Swift* data

XRT (Burrows et al. 2005) on board the *Swift* satellite uses a front-illuminated charge-coupled device (CCD) detector sensitive to photons with energies between 0.2 and 10 keV, with an effective area of about 110 cm^2 at 1.5 keV. Two readout modes are now available: photon counting (PC) and windowed timing (WT). In the former, the entire CCD is read every ∼2.5 s, whereas in the latter 10 rows are compressed in one, and only the central 200 (out of 600) columns are read out. One-dimensional imaging is preserved, achieving a time resolution of ∼1.7 ms and thus providing a larger dynamic range of measurable source intensities (see Hill et al. 2004 for a detailed description of the XRT readout modes).

We processed the data with standard screening criteria (see Capalbi et al. 2005) and generated exposure maps with the task XRTPIPELINE (version 0.13.3) from the FTOOLS package

(Blackburn 1995), using the spacecraft attitude file. We selected events with grades 0–12 and 0 for the PC and WT data,[3] respectively, and extracted the source and background spectra using XSELECT (v. 2.4). We accumulated the source counts from a circular region centred on the source position and with a radius of 20 pixels (one XRT pixel corresponds to about 2.36 arcsec). Noteworthy exceptions are represented by the magnetar Swift J1834.9−0846 and the source 1E 161348−5055, for which we opted for a circle of radius 6 and 10 pixels, respectively, to minimize the contribution from the surrounding diffuse emission (see Section 2.11). To estimate the background in the PC-mode data, we extracted the events within an annulus centred on the source position with inner and outer radius of 40 and 80 pixels, respectively (12 and 19 pixels for Swift J1834.9−0846, 10 and 20 pixels for 1E 161348−5055). For the observations targeting the 2009 outburst of 1E 1547−5408 we considered instead a circle as far as possible from the source, to reduce the contamination by the three expanding dust scattering X-ray rings (see Tiengo et al. 2010). For the WT-mode data we adopted a region far from the target and of the same size as that used for the source.

For all the observations we built exposure-corrected and background-subtracted light curves using XRTLCCORR and LCMATH (the latter accounting also for different areas of the source and background extraction regions). We binned them with different time resolutions, and removed possible bursts/flares episodes by applying intensity filters to the event lists. This procedure aims at minimizing flux overestimates, and avoiding possible spectral distortions induced by the bursting emission, which is typically harder than that of the underlying continuum.

In case an observation in PC mode suffered from photon pile-up (typically this occurs when the source net count rate exceeds $\sim$0.6 counts s^{-1}), we determined the extent of the piled-up region as follows. First, we modelled the wings of the radial profile of the source point-spread function (at a distance $>$15 arcsec from the centre) with a King function reproducing the PSF of the XRT (Moretti et al. 2005). We then extrapolated the model back to the core of the PSF, and compared it to the data points. The region where the observed PSF lies underneath the extrapolation of the King function was then excluded from our analysis.[4]

We created the observation-specific ancillary response files with XRTMKARF (v. 0.6.3), thereby correcting for the loss of counts due to hot columns and bad pixels, and accounting for different extraction regions, telescope vignetting and PSF corrections. We then assigned the appropriate redistribution matrix available in the HEASARC calibration data base, and excluded bad spectral channels (at energy $<$0.3 keV). We co-added individual spectra and responses for contiguous observations with very few counts and that were carried out with the same observing mode, to improve the statistics quality and increase the signal-to-noise ratio.[5] For extensively monitored outbursts we also constructed the long-term 0.3–10 keV count rate light curves (using the online *Swift* XRT data products generator; see Evans et al. 2009 for details), to gauge the decay time-scales (see Appendix B).

[3] Because of issues in the modelling of the response matrix files, spectra of heavily absorbed sources ($N_{\rm H} \gtrsim 10^{22}$ cm^{-2}) occasionally are known to exhibit a bump and/or turn-up at low energy (typically below 1 keV) in WT mode for events with grades $\geq$1. See http://www.swift.ac.uk/analysis/xrt/digest_cal.php

[4] See http://www.swift.ac.uk/analysis/xrt/xrtpileup.php

[5] Ancillary response files were weighted by the net number of counts of the source in each observation.

3.2 *XMM–Newton* data

The *XMM–Newton* satellite carries three co-aligned X-ray telescopes, each with an European Photon Imaging Camera (EPIC) imaging spectrometer at the focus. Two of the EPIC spectrometers use Metal Oxide Semiconductor CCD arrays (MOS cameras; Turner et al. 2001) and one uses pn CCDs (pn camera; Strüder et al. 2001). They all cover the 0.1–15 keV energy range with an effective area of about 500 cm^2 for each MOS and 1400 cm^2 for the pn at 1.5 keV. In this work we shall consider only data acquired with the pn camera, which provides the spectra with the highest counting statistics owing to its larger effective area.

The pn camera can operate in different modes. In full frame mode (FF; 73.4-ms time resolution), all pixels of the 12 CCDs are read out simultaneously and the full FoV is covered. In large window mode (LW; 47.7-ms time resolution), only half of the area in all CCDs is read out and in small window mode (SW; 5.7-ms time resolution) just part of one single CCD is used to collect data. The pn can also operate in timing mode, where data from a pre-defined area on one CCD chip are collapsed into a one-dimensional row to be read every 30 μs.

We retrieved the raw observation data files from the *XMM–Newton* Science Archive, and processed them to produce calibrated, concatenated photon event lists using the EPPROC tool of the *XMM–Newton* Science Analysis System (SAS v. 15.0; Gabriel et al. 2004) and the most up to date calibration files available (XMM-CCF-REL-332). For each observation we built a light curve of single pixel events (PATTERN = 0) for the entire FoV, and discarded episodes (if any) of strong soft-proton flares of solar origin using intensity filters. We then estimated the amount of residual contamination in each event file by comparing the area-corrected count rates in the in- and out-of-FoV regions of the detector,[6] and verified that it was negligible or low in all cases (here 'negligible' and 'low' are defined following De Luca & Molendi 2004). We extracted the source photons from a circular region centred on the source position and with a typical radius of 20–30 arcsec, depending on the source brightness, the presence of closeby sources and the distance from the edge of the CCD. The background was extracted from a circle located on the same CCD, and the position and size of the region were determined so as to guarantee similar low-energy noise subtraction and avoid detector areas possibly contaminated by out-of-time events from the source or too near to the CCD edges (we used the EBKGREG tool, which typically yielded larger radii for the cases where the source was particularly faint, e.g. SGR 1627−41 or SGR 0418+5729 close to the quiescent level). The case of Swift J1834.9−0846 stands apart owing to the surrounding extended emission (see Section 2.11), and the photon counts were collected within similar regions as those adopted by Younes et al. (2016).

We built background-subtracted and exposure-corrected light curves with different time binnings using the EPICLCCORR task, which also corrects the time series for any relevant instrumental effect such as bad pixels, chip gaps, PSF variation, vignetting, quantum efficiency and dead-time, and accounts for the different sizes

[6] We used the script provided by the *XMM–Newton* EPIC Background working group available at http://www.cosmos.esa.int/web/xmm-newton/epic-scripts#flare.

of the source and background extraction regions. We then removed possible source flaring episodes by applying ad hoc intensity filters on the light curves.

We estimated the potential impact of pile-up by comparing the observed event pattern distribution as a function of energy with the theoretical prediction in the 0.3–10 keV energy interval, by means of the EPATPLOT task. For piled-up sources, we selected the most suitable annular extraction region for the source counts via an iterative procedure, by excising larger and larger portions of the inner core of the source PSF until a match was achieved between the observed and expected distributions at the 1σ confidence level (c.l.) for both single and double pixel events.

We employed the standard filtering procedure in the extraction of the scientific products, retaining only single and double pixel events optimally calibrated for spectral analysis (PATTERN $\leq$ 4), and excluding border pixels and columns with higher offset for which the pattern type and the total energy are known with significantly lower precision (FLAG = 0). We calculated the area of source and background regions using the BACKSCALE tool, and generated the redistribution matrices and effective area files with RMFGEN and ARFGEN, respectively. We used the EPISPECCOMBINE task to co-add the spectra and average the response files of closeby observations carried out with the same instrumental setup (i.e. same observing mode and optical blocking filter in front of the pn CCD) and with a scarce number of counts, to obtain a reasonable number of spectral bins for a meaningful spectral analysis.

3.3 *Chandra* data

The *Chandra X-Ray Observatory* includes two focal plane instruments: the Advanced CCD Imaging Spectrometer (ACIS; Garmire et al. 2003) and the High Resolution Camera (HRC; Zombeck et al. 1995). The ACIS operates in the 0.2–10 keV energy range with an effective area of about 340 cm^2 at 1 keV. It consists of an imaging (ACIS-I) and a spectroscopic (ACIS-S) CCD arrays. The HRC covers the 0.1–10 keV interval with an effective area of about 225 cm^2 at 1 keV and comprises the HRC-I and the HRC-S detectors. The former optimized for wide-field imaging, and the latter designed for spectroscopy.[7]

The ACIS detectors enable two modes of data acquisition: the timed exposure (TE) mode, and the continuous clocking (CC) mode. In the former, each chip is exposed for a nominal time of 3.241 s (or a sub-multiple, if only a sub-array of a chip is being read-out). In the latter, data are transferred from the imaging array to the frame store array every 2.85 ms, at the expense of one dimension of spatial information.

We analysed the data following the standard analysis threads for a point-like source with the *Chandra* Interactive Analysis of Observations software (CIAO, v. 4.8; Fruscione et al. 2006) and the calibration files stored in the *Chandra* CALDB (v. 4.7.1). Only non-dispersed (zeroth-order) spectra were extracted for observations where a grating array was used. We used the CHANDRA_REPRO script to reprocess the data and generate new 'level 2' events files with the latest time-dependent gain, charge transfer inefficiency correction and sub-pixel adjustments. For TE-mode data and on-axis targets, we collected the source photons from a circular region around the source position with a radius of 2 arcsec. An important outlier is SGR 1745−2900 amid the Galactic Centre, for which the counts were accumulated within a 1.5-arcsec radius circular region. A larger radius would have included too many counts from Sgr A* (see Coti Zelati et al. 2015a, 2017 for details). The *Chandra* PSF exhibits significant variations in size and shape across the focal plane. Therefore, for the few cases where the target of interest was located far from the position of the aim point, we proceeded as follows. First, we accurately measured the coordinates of the source centroid by applying the CIAO source detection algorithm WAVDETECT (Freeman et al. 2002) to the exposure-corrected image. We adopted the default 'Ricker' wavelet ('Mexican Hat' wavelet) functions with scales ranging from 1 to 16 pixels with a $\sqrt{2}$ step size and the default value for the source pixel threshold (SIGTHRESH $= 10^{-6}$). We then calculated the off-axis angle from the pointing direction, and used the CIAO tool PSFSIZE_SRCS to estimate the radius of the 90 per cent encircled counts fraction at 3 keV. In all cases the background was extracted from an annulus centred on the source location. For observations with the ACIS set in CC mode, source events were instead collected through a rectangular region of dimension 4 arcsec along the readout direction of the CCD. Background events were extracted within two similar boxes oriented along the image strip, symmetrically placed with respect to the target and sufficiently far from the position of the source, to minimize the contribution from the PSF wings.

We filtered the data for flares from particle-induced background (e.g. Markevitch et al. 2003) by running the DEFLARE routine on the light curves, and estimated the impact of photon pile-up in the TE-mode observations using the PILEUP_MAP tool. On the other hand, the fast readout of the ACIS in the CC-mode ensured in all cases that the corresponding spectra were not affected by pile-up. Because of the sharp *Chandra* PSF, discarding photons in the core of the PSF to correct for pile-up effects results in a significant loss of counts. Spectral distortions were then mitigated directly in the spectral modelling, as described in Section 4.

We created the source and background spectra, the associated redistribution matrices and ancillary response files using the SPECEXTRACT script.[8] Spectra and auxiliary and response files for contiguous observations with low counting statistics were combined using the COMBINE_SPECTRA script.

4 SPECTRAL ANALYSIS

We generally grouped the background-subtracted spectra to have at least 20 counts in each spectral bin using GRPPHA, to allow for fitting using the χ^2 statistics. For the spectra with the largest number of counts (typically those extracted from *XMM–Newton* and *Chandra* observations, but in some cases also from *Swift* pointings at the earliest stages of the most powerful outbursts), we adopted a higher grouping minimum and the optimal binning prescription of Kaastra & Bleeker (2016).[9] For the spectra with too few counts for the χ^2-fitting, we opted to group the data to a lower degree (or even not to group them in the case of the *Swift* XRT spectra of SGR 1627−41 and Swift J1834.9−0846), and use the Cash statistics (*C*-statistics; Cash 1979).

We performed the spectral analysis separately for the *Swift*, *Chandra* and *XMM–Newton* data, owing to known cross-calibration

[7] Observations performed with the HRC-I were not analysed because this camera provides only a limited energy resolution on the detected photons.

[8] Ancillary response files are automatically corrected to account for continuous degradation in the ACIS CCD quantum efficiency.

[9] See http://cms.unige.ch/isdc/ferrigno/developed-code

uncertainties (e.g. Tsujimoto et al. 2011) and their remarkably different effective areas and energy dependence, which translate into different counting statistics and therefore best-fitting models in most cases (the larger the statistics available, the larger the number of spectral components required to properly fit the data).

For the spectral modelling we employed the XSPEC spectral fitting package (v. 12.9.1; Arnaud 1996), and applied the Levenberg–Marquardt minimization algorithm (Press et al. 1992). We restricted our analysis to the energy interval whereby the calibration of the spectral responses is best known, i.e. 0.3–10 keV for *Swift* XRT and *XMM–Newton* EPIC (with some exceptions for the XRT WT-mode data; see below), 0.3–8 keV for *Chandra*, 1.8–10 keV for *BeppoSAX* MECS, 0.1–2.4 keV for *ROSAT* PSPC and 3–10 keV for *RXTE* PCA. For the faintest outbursts (e.g. those of CXOU J164710.2−455216 and the 2008 event from 1E 1547−5408) and heavily absorbed sources (e.g. SGR 1833−0832 and Swift J1834.9−0846), we further limited our study to photons with energy above 1–2 keV, owing to the few available counts at lower energy. On the other hand, the spectra of SGR 0418+5729 softened significantly as the source approached the quiescent phase. The few photons at energy $\gtrsim$3 keV were overwhelmed by the background and hence discarded. In some cases, spectra acquired by *Swift* and with the XRT configured in WT mode exhibited some residual bumps due to calibration uncertainties below ~1 keV. Because these features would yield a misleading (systematically underestimated) value for the absorption column density, we decided to filter out the spectral channels at low energy (<0.8 keV).

4.1 Spectral models

For the continuum emission we tested a set of different single and double-component empirical models: a blackbody (BBODYRAD; BB), a power-law (PL), a blackbody plus a power-law (BB+PL), the superposition of two blackbodies (2BB) and resonant cyclotron scattering models. In particular, we applied the NTZ model developed by Nobili et al. (2008a,b), which is based on three-dimensional Monte Carlo simulations. The topology of the magnetic field is assumed to be a globally twisted, force-free dipole in the model, and its parameters are the surface temperature (assumed to be the same over the whole surface), the bulk motion velocity of the charged particles in the magnetosphere (assumed constant through the magnetosphere), the twist angle and a normalization constant. This model has the same number of free parameters as the empirical two-component models mentioned above (2BB and BB+PL). In the cases of XTE J1810−197 and the 2002 outburst of 1E 2259+586, the higher statistics quality available from *XMM–Newton* observations allowed us to probe more complicated models, such as the sum of three thermal components (3BB). Because the internal calibration accuracy of the pn CCD for on-axis sources is estimated to be better than 2 per cent at the 1σ c.l. (Smith 2016[10]), we added an extra 2 per cent systematic error term to each spectral channel in these cases, as also recommended by the online threads. We then assessed the number of required spectral components by means of the Fisher test (e.g. Bevington 1969), setting a minimum threshold of 3σ (99.7 per cent) for the statistical significance of the improvement in the fit.

If pile-up was detected in a *Chandra* observation (typically at the early stages of the outburst), the multiplicative pile-up model of Davis (2001) was included, as implemented in XSPEC. Following the prescriptions reported in '*The Chandra ABC Guide to Pile-up*',[11] the only parameters allowed to vary were the grade-migration parameter and the fraction of events within the central, piled up, portion of the source PSF.

The photoelectric absorption by the interstellar medium along the line of sight was described through the Tuebingen–Boulder model (TBABS in XSPEC), and we adopted the photoionization cross-sections from Verner et al. (1996) and the chemical abundances from Wilms, Allen & McCray (2000). The choice of these abundances typically translates into values for the column density about 30 per cent larger than those estimated assuming the solar abundance tables from Anders & Grevesse (1989).

For SGR 1745−2900 the FGCDUST model was also included to correct for the effects of scattering of X-ray photons on interstellar dust grains located along the line of sight towards the source (likely in the Galactic disc and a few kpc away from the Galactic Centre according to Jin et al. 2017; see also Coti Zelati et al. 2017). For SGR 1833−0832 and Swift J1834.9−0846, i.e. the most absorbed sources of our sample besides SGR 1745−2900 (see Table 2), we tested the inclusion of the XSCAT model (Smith, Valencic & Corrales 2016) to account for the effect of dust scattering of spreading the photons along the line of sight around the source, an effect that is more relevant for the most heavily absorbed objects.[12]

Although both the adoption of different chemical abundances and the correction for dust scattering opacity yield some differences in the values for the hydrogen column density and hence the unabsorbed fluxes, they provide only a secondary source of systematic error on the estimate of the luminosities compared to the uncertainties on the sources distances (see Section 5). Furthermore, we checked that they did not translate into significantly different decay patterns and estimates for the total energy released during the outburst.

4.2 Spectral fits

For each outburst, we started by fitting together the absorbed BB+PL and 2BB models to the spectra acquired by *Swift* XRT[13] (with the exception of XTE J1810−197, the 2008 outburst of SGR 1627−41, SGR 0418+5729, SGR 1833−0832, Swift J1834.9−0846, the 2011 outburst of CXOU J164710.2−455216, SGR 1935+2154 and PSR J1119−6127, for which a single absorbed blackbody model provided an acceptable fit across the entire data set). All parameters of the BB and PL components were left free to vary from observation to observation. The absorption column density was left free to vary as well, but with the request to be the same at all stages of the outburst evolution. For extensively monitored sources (i.e. SGR 0501+4516, 1E 1547−5408 during the 2009 outburst, Swift J1822.3−1606, 1E 1048.1−5937, 1E 2259+586 during the 2012 outburst, SGR 1935+2154 and PSR J1119−6127), the joint modelling was performed on groups of 20 spectra, to reduce the time-scale of the convergence of the fit and of the computation of parameter uncertainties.

[10] See http://xmm2.esac.esa.int/docs/documents/CAL-TN-0018.pdf

[11] See http://cxc.harvard.edu/ciao/download/doc/pileup_abc.pdf

[12] We assumed different models for the dust composition and grain size distribution (see Mathis, Rumpl & Nordsieck 1977; Weingartner & Draine 2001; Zubko, Dwek & Arendt 2004).

[13] For SGR 1745−2900, we considered instead *Chandra* data alone, because only the exquisitely sharp PSF of the ACIS instrument enables to single out the magnetar counterpart in the crowded region of the Galactic Centre. See Coti Zelati et al. (2015a, 2017) for details.

Table 2. Spectral fitting results of magnetar outbursts. The year of the outburst onset is indicated in parentheses. NTZ denotes the resonant cyclotron scattering code by Nobili et al. (2008a,b), and was applied only in the cases where a power-law component was needed when fitting 'empirical' models to the data. To account for interstellar absorption, we adopted the TBABS model, cross-sections from Verner et al. (1996) and abundances from Wilms et al. (2000). The hydrogen column density was tied up among all the observations targeting a specific source and the associated uncertainty is quoted at the 1σ c.l.

Source	Observatory (# obs)	Best-fitting model	N_H (emp) (10^{22} cm^{-2})	N_H (NTZ)	Reference
SGR 1627−41 (1998)	*BeppoSAX* (4)	BB	6 ± 1	–	Table A1
	XMM–Newton (2)	BB	6^{+2}_{-1}	–	
	Chandra (4)	BB	10^{+2}_{-1}	–	
1E 2259+586 (2002)	*XMM–Newton* (8)	3BB	0.816 ± 0.007	–	Table A3
XTE J1810−197 (2003)	*XMM–Newton* (22)	3BB (1–11)	1.22 ± 0.02	–	Table A5
		2BB (11–22)		–	
SGR 1806−20 (2004)	*XMM–Newton* (10)	2BB	8.5 ± 0.1	–	Table A6
CXOU J164710.2−455216 (2006)	*Swift* (18)	BB+PL	3.06 ± 0.08	$2.43^{+0.04}_{-0.03}$	Table A7
	XMM–Newton (5)[a]	BB+PL	3.01 (fixed)	2.39 (fixed)	
	Chandra (5)	BB+PL	3.01 ± 0.04	$2.39^{+0.02}_{-0.01}$	
SGR 1627−41 (2008)	*Swift* (21)	BB	9 ± 2	–	Table A2
	XMM–Newton (2)	2BB	10^{+3}_{-2}	–	
	Chandra (4)	BB	10 ± 2	–	
SGR 0501+4516 (2008)	*Swift* (62)[b]	BB+PL (1–20)	1.319 (fixed)	$0.708^{+0.007}_{-0.006}$	Table A9
		BB+PL (21–40)	1.319 (fixed)	0.71 ± 0.03	
		BB+PL (41–62)	1.319 (fixed)	0.708 (fixed)	
	XMM–Newton (6)	BB+PL	1.319 ± 0.009	0.705 ± 0.004	
	Chandra (1)	BB+PL	1.33 ± 0.03	0.85 ± 0.01	
1E 1547−5408 (2008)	*Swift* (15)	BB+PL	4.9 ± 0.1	$4.65^{+0.05}_{-0.07}$	Table A10
	Chandra (5)	BB+PL	5.1 ± 0.2	4.83 ± 0.06	
1E 1547−5408 (2009)	*Swift* (97)	BB+PL (1–20)	$4.91^{+0.03}_{-0.13}$	4.59 ± 0.09	Table A11
		BB+PL (21–40)	4.91 (fixed)	4.59 (fixed)	
		BB+PL (41–60)	4.91 (fixed)	4.59 (fixed)	
		BB+PL (61–80)	4.91 (fixed)	4.59 (fixed)	
		BB+PL (81–97)	4.91 (fixed)	4.59 (fixed)	
	XMM–Newton (2)[a]	BB+PL	4.9 (fixed)	4.65 (fixed)	
	Chandra (3)	BB+PL	5.0 ± 0.1	$4.71^{+0.10}_{-0.07}$	
SGR 0418+5729 (2009)	*Swift* (24)	BB	0.57 (fixed)	–	Table A12
	XMM–Newton (11)	2BB (1)	$0.57^{+0.04}_{-0.03}$	–	
		BB (2–11)	0.57 (fixed)	–	
	Chandra (4)	BB	0.57 (fixed)	–	
SGR 1833−0832 (2010)	*Swift* (27)	BB	13.1 ± 0.9	–	Table A13
	XMM–Newton (3)	BB	15.5 ± 0.4	–	
	Chandra (1)	BB	13.7 ± 0.9	–	
Swift J1822.3−1606 (2011)	*Swift* (60)	BB+PL (1–20)	0.68 (fixed)	0.289 (fixed)	Table A14
		BB+PL (21–40)	0.68 (fixed)	0.289 (fixed)	
		BB+PL (40–60)	0.68 (fixed)	0.289 (fixed)	
	XMM–Newton (5)	BB+PL	0.68 ± 0.01	0.289 ± 0.004	
	Chandra (5)	BB+PL	0.62 ± 0.02	0.283 ± 0.005	
Swift J1834.9−0846 (2011)	*Swift* (19)	BB	19 (fixed)	–	Table A15
	XMM–Newton (3)	BB	15 ± 1	–	
	Chandra (4)	BB	19 ± 1	–	
CXOU J164710.2−455216 (2011)	*Swift* (7)	BB	2.6 ± 0.3	–	Table A8
	XMM–Newton (1)	2BB	2.5 ± 0.1	–	
	Chandra (1)	BB	2.8 ± 0.1	–	
1E 1048.1−5937 (2011)	*Swift* (55)	BB (1–20)	0.61 ± 0.02	–	Table A16
		BB (21–40)	0.61 (fixed)	–	
		BB (40–55)	0.56 (fixed)	–	
1E 2259+586 (2012)	*Swift* (44)	2BB (1–20)	0.38 ± 0.01	–	Table A4
		2BB (21–44)	0.38 (fixed)	–	
SGR 1745−2900 (2013)	*Chandra* (35)	BB	18.7 ± 0.1	–	Table A18
SGR 1935+2154 (2014)	*Swift* (45)	BB (1–20)	2.3 ± 0.2	–	Table A19
		BB (21–45)	2.3 (fixed)	–	
	XMM–Newton (9)	2BB	2.37 ± 0.07	–	

Table 2 – *continued*

Source	Observatory (# obs)	Best-fitting model	$N_{\rm H}$ (emp) (10^{22} cm^{-2})	$N_{\rm H}$ (NTZ)	Reference
	Chandra (3)	2BB	2.8 ± 0.1		
1E 1048.1−5937 (2016)	*Swift* (60)	BB (1–20)	0.56 ± 0.04	–	Table A17
		BB (21–40)	0.59 ± 0.04	–	
		BB (40–60)	0.56 (fixed)	–	
PSR J1119−6127 (2016)	*Swift* (35)	BB (1–20)	0.69 ± 0.05	–	Table A20
		BB (21–36)	0.69 (fixed)	–	
1E 161348−5055 (1999, 2016)	*Chandra* (25), *XMM–Newton* (2), *Swift* (129)	2BB	2.05 ± 0.05	–	Rea et al. (2016)

Notes. [a]The absorption column density was fixed to a value compatible with that inferred from the fits of the data sets from the other X-ray instruments, because a significant excess in the fit residuals was detected below about 1 keV independently on the choice of the background region and of the adopted spectral model (see e.g. Bernardini et al. 2009 for this issue). We obtained acceptable fits in all cases.
[b]The absorption column density was fixed to the value obtained from the fit to the *XMM–Newton* spectra, because the XRT was operating in WT in all cases and bumps of instrumental origin were present at ∼0.8–1 keV (see the text). We obtained acceptable fits in all cases.

In most cases, spectra of observations carried out at late stages of the outburst were described adequately by an absorbed blackbody alone and the addition of a second component was not statistically required. However, we decided to retain the second component in the spectral fits, and freeze its pivotal parameter (the power-law photon index in the BB+PL model or the temperature of the second, hotter, blackbody in the 2BB model) to the value inferred for the spectrum of the last pointing where the second component is significantly detected. Alternatively, this parameter was tied up between all these data sets. For both alternative strategies, the normalizations of the spectral components were left free to vary. We then derived stringent upper limits on the contribution of the additional spectral component, and verified that the fits to the single spectra yielded values for the parameters consistent with those inferred from the joint modelling.

The above-mentioned fitting procedure was subsequently repeated for the *XMM–Newton* and *Chandra* data sets. Table 2 reports the best-fitting models. Appendix C reports a series of Fig. C1 showing a set of high-quality X-ray spectra and the best-fitting empirical models for several outbursts that were repeatedly monitored by the *XMM–Newton* or *Chandra* observatories.

For the cases where the *C*-statistics was employed, we evaluated the quality of the fit by Monte Carlo simulations. We used the GOODNESS command within XSPEC to simulate a total of 1000 spectra (based on a Gaussian distribution of parameters centred on the best-fitting model parameters and with Gaussian width set by the 1σ uncertainties on the parameters), and determined the percentage of simulations having a *C*-statistics value much lower or higher than that obtained from the best fit of the data.

5 LIGHT CURVES

For each fitted spectrum, we calculated the absorbed flux for the total source emission, as well as the unabsorbed flux and the luminosity for the single spectral components and for the total source emission (all in the 0.3–10 keV energy range). Unabsorbed fluxes were calculated using the convolution model CFLUX, and converted to luminosities (as measured by an observer at infinity) assuming isotropic emission and the most reliable value for the distance of the source (see Section 2 and Table 3). All the uncertainties are quoted at the 1σ c.l. for a single parameter of interest ($\Delta\chi^2 = 1$; Lampton, Margon & Bowyer 1976) throughout this work, whereas upper limits are reported at the 3σ c.l. For each outburst, we checked that the unabsorbed fluxes inferred for observations carried out with different instruments approximately at the same epoch were consistent with each other within the cross-correlation uncertainties.

The determination of unabsorbed fluxes from models comprising absorbed power-law components is known to overestimate the source flux by a large factor, owing to the divergence of the power-law component at low energy. We hence considered the results obtained from the NTZ model (Nobili et al. 2008a, Nobili et al.2008b) to estimate bolometric (0.01–100 keV) luminosities for the cases where a power-law spectral component was required in the spectral fits. In all cases the bolometric fluxes were determined after having defined dummy response matrices with the DUMMYRSP command in XSPEC. An uncertainty of 15 per cent was assigned to each flux. We note that, in some cases, an additional spectral component was observed in the hard X-rays at the outburst peak, which then became undetectable within the following few weeks. However, the paucity of hard X-ray monitorings of magnetar outbursts prevents a proper study of the appearance, disappearance and total energetics of this component over the whole class. If we consider all the hard X-ray observations of magnetar outbursts performed so far by *INTEGRAL*, *Suzaku* and *NuSTAR* (for SGR 0501+4516, SGR 1806−20, 1E 1547−5408, SGR 1745−2900, SGR 1935+2154, PSR J1119−6127, 1E 161348−5055; see Esposito et al. 2007; Rea et al. 2009; Enoto et al. 2010a,b; Kuiper et al. 2012; Kaspi et al. 2014; Archibald et al. 2016a; Rea et al. 2016; Younes et al. 2017; see Enoto et al. 2017, for a review of all these cases), our values for the bolometric fluxes neglecting this component are underestimated (only close to the outburst peak though) by a factor $\lesssim$20 per cent in all cases but SGR 1806−20 and 1E 1547−5408. For these two cases we might be underestimating our bolometric flux at the outburst peak by a factor of ∼2–3; however the lack of a proper monitoring of the hard X-ray component precludes an accurate modelling of the time evolution of the hard X-ray emission.

All cooling curves are shown in a series of figures in Appendix D (see Figs D1–D20), and include the evolution of the absorbed fluxes, of the 0.3–10 keV luminosities (for the single spectral components and for the total emission) and of the bolometric luminosities.

Fig. 1 shows the temporal decays of the bolometric luminosities for all outbursts. We refer each curve to the epoch of the outburst onset, defined as the time of the first burst detection from the source

Table 3. Distances, timing properties and timing-inferred parameters for all magnetars, high magnetic field pulsars, central compact objects, rotation-powered pulsars and X-ray dim isolated neutron stars included in our correlation study (see http://magnetars.ice.csic.es). Sources that underwent major and extensively monitored magnetar-like outbursts are marked in bold.

Source	Class	D (kpc)	P (s)	$\dot{P}$ (10^{-11} s s^{-1})	$B_{\rm p,\,dip}$[a] (10^{14} G)	$\dot{E}_{\rm rot}$[b] (erg s^{-1})	$\tau_{\rm c}$[c] (kyr)	Reference
SGR 1627−41[d]	Magnetars	11	2.59	1.9	4.5	4.3×10^{34}	2	Esposito et al. (2009a)
1E 2259+586		3.2	6.98	0.048	1.2	1.3×10^{32}	230	Dib & Kaspi (2014)
XTE J1810−197		3.5	5.54	0.283	2.6	6.7×10^{32}	31	Camilo et al. (2016)
SGR 1806−20		8.7	7.55	76.95	49	7.0×10^{34}	0.2	Younes et al. (2015)
CXOU J164710.2−455216		4	10.61	0.097	2.1	3.2×10^{31}	173	Rodríguez Castillo et al. (2014)
SGR 0501+4516		1.5	5.76	0.594	3.7	1.2×10^{33}	15	Camero et al. (2014)
1E 1547−5408		4.5	2.07	4.77	6.4	2.1×10^{35}	0.7	Dib et al. (2012)
SGR 0418+5729		2	9.08	0.0004	0.1	2.1×10^{29}	∼36 000	Rea et al. (2013a)
SGR 1833−0832[e]		10	7.57	0.35	3.3	3.2×10^{32}	34	Esposito et al. (2011)
Swift J1822.3−1606		1.6	8.44	0.013	0.7	8.4×10^{30}	1030	Rodríguez Castillo et al. (2016)
Swift J1834.9−0846		4.2	2.48	0.806	2.9	2.1×10^{34}	5	Esposito et al. (2013)
1E 1048.1−5937		9	6.46	2.18	7.6	3.2×10^{33}	4.7	Dib & Kaspi (2014)
SGR 1745−2900		8.3	3.76	3.06	6.9	2.2×10^{34}	1.9	Coti Zelati et al. (2017)
SGR 1935+2154		9	3.24	1.43	4.4	1.6×10^{34}	3.6	Israel et al. (2016)
SGR 1900+14		12.5	5.20	9.2	14.0	2.6×10^{34}	0.9	Olausen & Kaspi (2014)
4U 0142+614		3.6	8.69	0.20	2.7	1.3×10^{32}	69	Olausen & Kaspi (2014)
1E 1841−045		8.5	11.79	4.09	13.8	9.9×10^{33}	4.6	Olausen & Kaspi (2014)
1RXS J170849.0−4009		3.8	11.01	1.95	9.3	5.8×10^{32}	9.1	Olausen & Kaspi (2014)
CXOU J010043.1−721		62.4	8.02	1.88	7.9	1.4×10^{33}	6.8	Olausen & Kaspi (2014)
CXOU J171405.7−3810		13.2	3.83	6.40	10.0	4.5×10^{34}	0.95	Olausen & Kaspi (2014)
SGR 0526−66		49.7	8.05	3.8	11.0	2.9×10^{33}	3.4	Olausen & Kaspi (2014)
PSR J1119−6127	High-*B* pulsars	8.4	0.41	0.4	0.82	2.5×10^{36}	1.6	Viganò et al. (2013)
PSR J1846−0258		6.0	0.33	0.71	0.98	8.1×10^{36}	0.7	Viganò et al. (2013)
PSR J0726−2612		1.0	3.44	0.03	0.64	2.5×10^{32}	190	Viganò et al. (2013)
PSR J1819−1458		3.6	4.26	0.057	1.0	3.2×10^{32}	120	Viganò et al. (2013)
PSR J1718−3718		4.5	3.38	0.16	1.5	1.6×10^{33}	33	Viganò et al. (2013)
1E 161348−5055	CCOs	3.3	24030	<70	<2600	$<2 \times 10^{24}$	>540	Rea et al. (2016)
CXOU J185238.6+0040		7.1	0.105	0.00000087	0.00061	3.2×10^{32}	∼190000	Viganò et al. (2013)
1E 1207.4−5209		2.1	0.424	0.00000220	0.00196	1.2×10^{31}	∼302000	Viganò et al. (2013)
RX J0822−4300		2.2	0.112	0.00000093	0.00058	1.9×10^{32}	∼254000	Viganò et al. (2013)
RX J0420.0−502	XDINSs	0.34	3.45	0.004	0.2	2.5×10^{31}	∼2000	Viganò et al. (2013)
RX J1856.5−375		0.12	7.06	0.003	0.3	3.2×10^{30}	∼3800	Viganò et al. (2013)
RX J2143.0+065		0.43	9.43	0.004	0.4	2.0×10^{30}	∼3600	Viganò et al. (2013)
RX J0720.4−312		0.29	8.39	0.007	0.5	4.7×10^{30}	∼1900	Viganò et al. (2013)
RX J0806.4−412		0.25	11.37	0.0055	0.5	1.6×10^{30}	∼3300	Viganò et al. (2013)
RX J1308.6+212		0.50	10.31	0.01	0.7	4.0×10^{30}	∼1500	Viganò et al. (2013)
RX J1605.3+324		0.35	3.39	0.16	1.5	1.6×10^{33}	34	Viganò et al. (2013)
PSR J0538+281	RPPs	1.3	0.143	0.0005	0.015	5.0×10^{34}	620	Viganò et al. (2013)
PSR B1055−52		0.73	0.197	0.0006	0.02	3.2×10^{34}	540	Viganò et al. (2013)
PSR J0633+174		0.25	0.237	0.001	0.03	3.2×10^{34}	340	Viganò et al. (2013)
PSR B1706−44		2.6	0.102	0.009	0.06	3.2×10^{36}	17	Viganò et al. (2013)
PSR B0833−45		0.28	0.089	0.01	0.07	6.3×10^{36}	11	Viganò et al. (2013)
PSR B0656+14		0.28	0.385	0.0055	0.09	4.0×10^{34}	110	Viganò et al. (2013)
PSR B2334+61		3.1	0.495	0.02	0.2	6.3×10^{34}	41	Viganò et al. (2013)
PSR J1740+100		1.4	0.154	0.2	0.4	2.5×10^{37}	1.2	Viganò et al. (2013)

Notes. [a]Assuming a force-free magnetosphere and an aligned rotator, a star radius $R = 10$ km and moment of inertia $I = 10^{45}$ g cm^2, the dipolar component of the surface magnetic field at the polar caps is given by $B_{\rm p,dip} \sim 2 \cdot (3c^3 I P \dot{P} / 8\pi^2 R^6)^{1/2} \sim 6.4 \times 10^{19} (P\dot{P})^{1/2}$ G. Relativistic magnetohydrodynamic simulations of pulsar magnetospheres have shown that the estimate offered by this formula is correct within a factor of ∼2–3 (Spitkovsky 2006).
[b]With the same assumptions, the rotational energy loss is given by $\dot{E}_{\rm rot} = 4\pi^2 I \dot{P} P^{-3} \sim 3.9 \times 10^{46} \dot{P} P^{-3}$ erg s^{-1}.
[c]With the same assumptions and assuming that the spin period at birth was much smaller than the current value, the characteristic age is given by $\tau_{\rm c} = P/2\dot{P}$.
[d]The spin period and its derivative were detected only following the 2008 re-activation of the source. We assume the same spin period derivative also for the 1998 outburst, and consider the same values for $B_{\rm p,\,dip}$, $\dot{E}_{\rm rot}$ and $\tau_{\rm c}$ in our searches for correlations.
[e]The value for the distance is assumed.

(mostly with *Swift* BAT or *Fermi* GBM), or of the giant flare in the case of SGR 1806−20 (note however that the source flux already doubled during the first half of 2004 with respect to the quiescent level; Mereghetti et al. 2005). For XTE J1810−197 and 1E 1048.1−5937, for which no bursts were detected prior to their outbursts (see Sections 2.3 and 2.12, respectively), we adopted the epoch of the observation where an increase in the X-ray flux was first measured as the reference epoch.

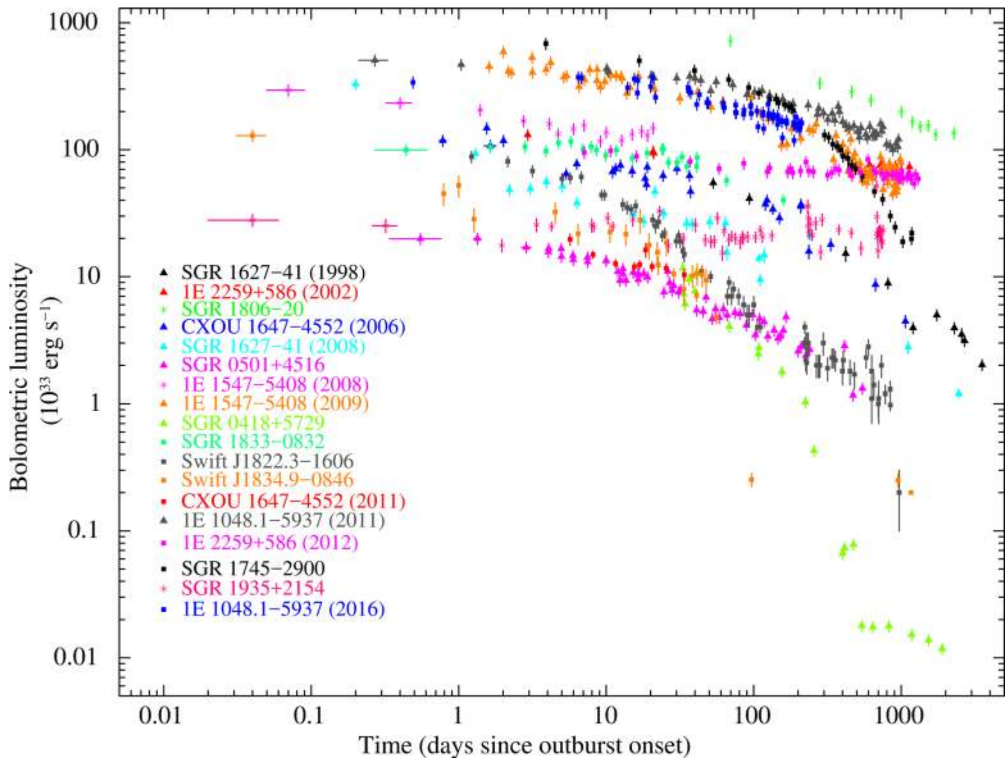

Figure 1. Temporal evolution of the bolometric (0.01–100 keV) luminosities for all outbursts re-analysed in this work. The distances assumed are those quoted in Table 3.

5.1 Phenomenological modelling

We modelled the decays of the X-ray luminosities of the single spectral components and of the total bolometric luminosities using a constant (dubbed L_q and representing the quiescent level; see Table 4) plus one or more exponential functions (dubbed EXP, 2EXP, and 3EXP in the following) of the form

$$L(t) = L_q + \sum_{i=1}^{j} A_i \times \exp(-t/\tau_i), \tag{1}$$

with $j \leq 3$ (τ_i denotes the e-folding time). The number of required exponential functions was evaluated by means of the F-test, i.e. an additional exponential was included only if it yielded an improvement in the fit of at least 3σ. A superexponential function of the form

$$L(t) = L_q + B \times \exp[-(t/\tau)^\alpha] \tag{2}$$

was also tested as an alternative to the double-exponential model in several cases, leading however to an extrapolated luminosity at the very early stages of the outburst systematically overestimated compared to that obtained with the double-exponential function. We assume conservatively that the peak luminosity attains a value not so different from that measured in the earliest observation available, and favour the double-exponential model in the following.

L_q was fixed at the quiescent value or, in cases of non-detections, constrained to be lower than the upper limit (see Table 4 for our estimates of the quiescent bolometric luminosities). There are however two exceptions for the modelling of the bolometric light curves: in the case of the 2008 outburst of 1E 1547−5408 and of the 1998 outburst of SGR 1627−41, the sources did not reach the historical quiescent level while recovering from the outburst. In these cases the constant term was held fixed at the quiescent value reached after that particular outburst (which is larger than the historical minimum reported in Table 4).

Although other alternative phenomenological models such as broken power laws or those consisting in the combination of one or multiple linear and power law terms could satisfactorily reproduce the decays of several outbursts, we opted to fit exponential functions to all light curves, to allow a direct comparison of the decay time-scales (i.e. the τ parameter) among different outbursts. On the other hand, the estimate of the outburst energetics is not sensitive to the model used to fit the luminosity decay.

5.2 Outburst energetics

We estimated the total outburst impulsive energetics by integrating the best-fitting model for the bolometric light curves over the whole duration of the event, and extrapolating it to the quiescent value for the cases where the observational campaign was not extended enough to follow completely the return to the pre-outburst state:

$$E = \int_0^{t_q} L_{bol}(t)\, dt, \tag{3}$$

where t_q is the epoch of the recovery of the quiescent state expressed as time since the outburst onset. For the sources that are still recovering from their outbursts (i.e. 1E 1547−5408, SGR 1745−2900, 1E 1048.1−5937, PSR J1119−6127 and 1E 161348−5055), we assumed no changes in the decay pattern down to quiescence for the estimate of the time-scales and energetics (in these cases the derived decay time-scale and the total outburst energetics should be considered as upper limits). Fig. 2 shows the best-fitting models (see also the right-hand panels of Figs D5–D17 for the individual cases), and Table 1 reports the corresponding parameters. The assumed 15 per cent error on each bolometric value is likely an

Table 4. Quiescent fluxes and luminosities (0.3–10 keV) for magnetars showing major outbursts or variations in their persistent emission. Bolometric luminosities are also listed. Magnetars are ordered as in Table 5. Uncertainties are reported at the 1σ c.l., upper limits at the 3σ c.l.

Source	Date	Observatory	Obs. ID	Exposure (ks)	Abs/Unabs flux (erg cm^{-2} s^{-1})	$L_{X,q}$ (erg s^{-1})	$L_{bol,q}$
SGR 1627−41	2015 Feb 18	*XMM–Newton*	0742650101	19.1	$4.2^{+0.2}_{-2.1} \times 10^{-14}$ $(8 \pm 1) \times 10^{-14}$	$(1.2 \pm 0.1) \times 10^{33}$	$\sim 1.2 \times 10^{33}$
SGR 1900+14	2005 Sep 22	*XMM–Newton*	0305580201	19.1	$(3.92 \pm 0.05) \times 10^{-12}$ $(6.7 \pm 0.2) \times 10^{-12}$	$(1.25 \pm 0.04) \times 10^{35}$	$\sim 1.4 \times 10^{35}$
1E 2259+586[a]	2014 Nov 04 to 2015 Nov 17	*Swift*	00032035087-114	40.1	$(3.55 \pm 0.02) \times 10^{-11}$ $(4.74 \pm 0.03) \times 10^{-11}$	$(5.8 \pm 0.3) \times 10^{34}$	$\sim 6.1 \times 10^{34}$
XTE J1810−197	1993 Apr 03	*ROSAT*/PSPC	RP900399N00	5.3	$\sim 5.3 \times 10^{-13}$ $\sim 1.7 \times 10^{-11}$	$\sim 2.5 \times 10^{34}$	$\sim 3.2 \times 10^{34}$
SGR 1806−20	2011 Mar 23	*XMM–Newton*	0654230401	22.4	$(5.49 \pm 0.07) \times 10^{-12}$ $(9.0 \pm 0.3) \times 10^{-12}$	$(8.2 \pm 0.3) \times 10^{34}$	$\sim 1.4 \times 10^{35}$
CXOU J1647−4552	2009 Aug 24	*XMM–Newton*	0604380101	38.2	$(8.0 \pm 0.2) \times 10^{-13}$ $(1.72 \pm 0.08) \times 10^{-12}$	$(3.3 \pm 0.2) \times 10^{33}$	$\sim 3.5 \times 10^{33}$
4U 0142+61	2004 Jul 24	*XMM–Newton*	0206670201	21.9	$(1.215 \pm 0.002) \times 10^{-10}$ $(2.309 \pm 0.003) \times 10^{-10}$	$(3.58 \pm 0.05) \times 10^{35}$	$\sim 3.8 \times 10^{35}$
SGR 0501+4516	2009 Dec 07 to 2010 Feb 21	*Swift*	0032117465–68	25.1	$(2.5 \pm 0.1) \times 10^{-12}$ $(4.4 \pm 0.3) \times 10^{-12}$	$(1.2 \pm 0.8) \times 10^{33}$	$\sim 1.3 \times 10^{33}$
1E 1547−5408	2006 Jul 01	*Chandra*	7287	9.5	$(3.2 \pm 0.3) \times 10^{-13}$ $(9 \pm 2) \times 10^{-13}$	$(2.2 \pm 0.5) \times 10^{33}$	$\sim 2.3 \times 10^{33}$
SGR 0418+5729	2014 Aug 13–18	*XMM–Newton*	0741970201–401	108.1	$(1.01 \pm 0.06) \times 10^{-14}$ $(1.6 \pm 0.2) \times 10^{-14}$	$(7 \pm 1) \times 10^{30}$	$\sim 8 \times 10^{30}$
SGR 1833−0832[b]	2006 Sep 16	*XMM–Newton*	0400910101	8.3	$<6 \times 10^{-14}$ $<7 \times 10^{-13}$	$<8 \times 10^{33}$	$<8 \times 10^{33}$
1E 1841−045	2000 Jul 29	*Chandra*[c]	730	10.5	$(2.33 \pm 0.03) \times 10^{-11}$ $(5.00 \pm 0.04) \times 10^{-11}$	$(4.32 \pm 0.03) \times 10^{35}$	$\sim 4.6 \times 10^{35}$
Swift J1822.3−1606	2014 Mar 08	*XMM–Newton*	0722520101	40.3	$(2.3 \pm 0.8) \times 10^{-13}$ $(6.5 \pm 1.0) \times 10^{-13}$	$(2.0 \pm 0.5) \times 10^{32}$	$\sim 2.3 \times 10^{32}$
Swift J1834.9−0846	2009 Jun 06	*Chandra*	10126	46.6	$<1 \times 10^{-14}$ $<1 \times 10^{-13}$	$<2 \times 10^{32}$	$<2 \times 10^{32}$
1E 1048.1−5937	2011 Aug 06	*XMM–Newton*	0654870101	21.9	$(5.56 \pm 0.04) \times 10^{-12}$ $(8.9 \pm 0.2) \times 10^{-12}$	$(8.6 \pm 0.2) \times 10^{34}$	$\sim 8.9 \times 10^{34}$
SGR 1745−2900	1999 Sep 21 – 2012 Oct 29	*Chandra*	129 obs[d]	4808.6	$<2 \times 10^{-14}$ $<1.5 \times 10^{-12}$	$<1 \times 10^{34}$	$<1 \times 10^{34}$
SGR 1935+2154[e]	2014 Oct 04	*XMM–Newton*	0722412701	16.1	$(8.6 \pm 0.2) \times 10^{-13}$ $(1.7 \pm 0.2) \times 10^{-12}$	$(1.6 \pm 0.1) \times 10^{34}$	$\sim 1.9 \times 10^{34}$
PSR J1119−6127	2004 Oct 31	*Chandra*	4676	60.5	$(4.8 \pm 0.6) \times 10^{-14}$ $(6.7 \pm 0.4) \times 10^{-14}$	$(5.7 \pm 0.3) \times 10^{32}$	$\sim 5.8 \times 10^{32}$
PSR J1846−0258	2000 Oct 15	*Chandra*	748	37.3	$(3.2 \pm 0.2) \times 10^{-12}$ $(3.6 \pm 0.1) \times 10^{-12}$	$(1.55 \pm 0.04) \times 10^{34}$	$\sim 2 \times 10^{34}$
1E 161348−5055	1999 Sep 26	*Chandra*	0123	13.4	$(9.8 \pm 0.6) \times 10^{-13}$ $(2.15 \pm 0.09) \times 10^{-12}$	$(2.8 \pm 0.1) \times 10^{33}$	$\sim 3 \times 10^{33}$

Notes. [a]The steady level of the source is slightly lower after the 2012 outburst (as measured with *Swift*) compared to that after the 2002 outburst (as measured with *XMM–Newton*), but they are however consistent with each other within the uncertainties. We then consider the more precise value derived from the *XMM–Newton* data sets.
[b]A distance of 10 kpc is assumed.
[c]The field around the source has been observed three times by *Chandra* (two with the ACIS set in TE mode and one in CC mode). We consider here the CC-mode observation to minimize pile-up issues.
[d]See http://www.sgra-star.com for the 2012 *Chandra* X-ray Visionary Project for HETGS Observations of Sgr A* (see e.g. table 1 by Neilsen et al. 2013 for the log of the observations).
[e]A distance of 9 kpc was assumed.

underestimate (the largest uncertainty arising from the poorly constrained distance of the source in almost all cases). For some extensively monitored outbursts we verified that the choice of larger uncertainties on these values yielded no significant alteration of the decay pattern and of our estimates for the characteristic time-scales and the amount of energy released during the event.

6 PEAK AND QUIESCENT LUMINOSITIES

Fig. 3 shows the maximum luminosity increase as a function of the quiescent (steady) X-ray luminosity for all magnetars that so far have displayed substantial enhancements and/or variability in their X-ray emission. To have a more complete sample, we have also included SGR 1900+14, 4U 0142+61 and 1E 1841−045. In fact, although extensive X-ray observations in the *Swift*, *XMM–Newton* and *Chandra* era did not detect major X-ray outbursts from these targets, re-brightenings or subtle variations around their persistent activity have been nevertheless reported throughout the last 15 yr. SGR 1900+14 exhibited a giant flare in 1998 (Hurley et al. 1999), and re-brightened in the X-rays on two occasions, 2001 April and 2006 March (Göğüş et al. 2011b, and references therein). Its flux decline was monitored by *Chandra* and *XMM–Newton* until 2008,

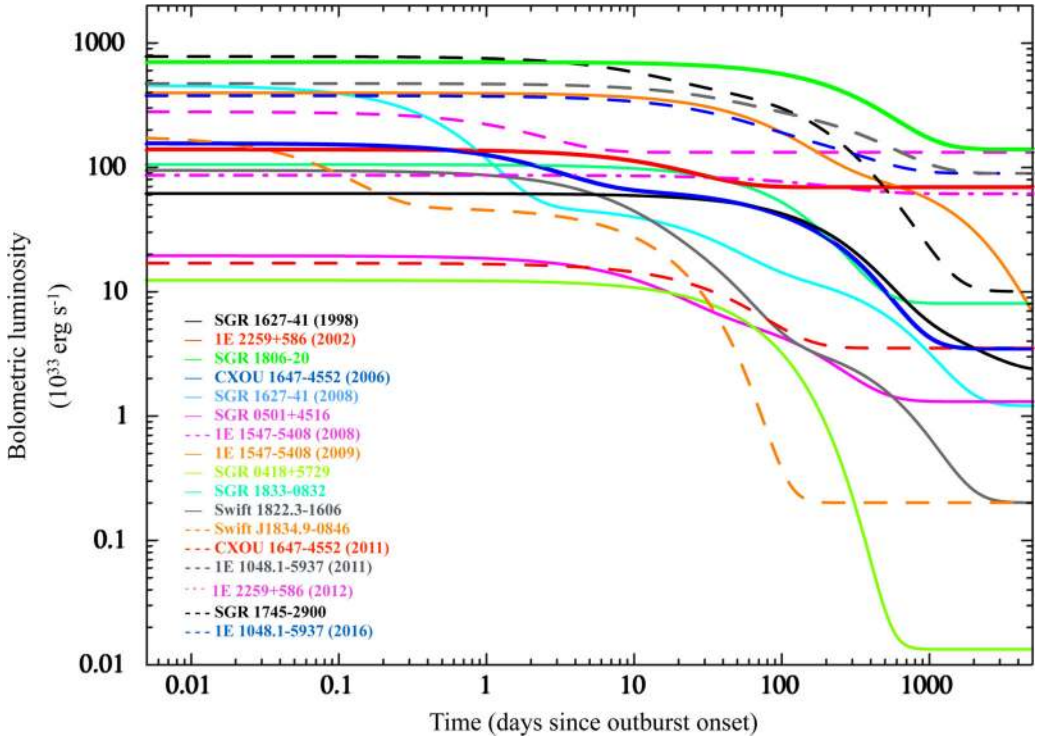

Figure 2. Models describing the temporal evolution of the bolometric (0.01–100 keV) luminosities for all outbursts re-analysed in this work.

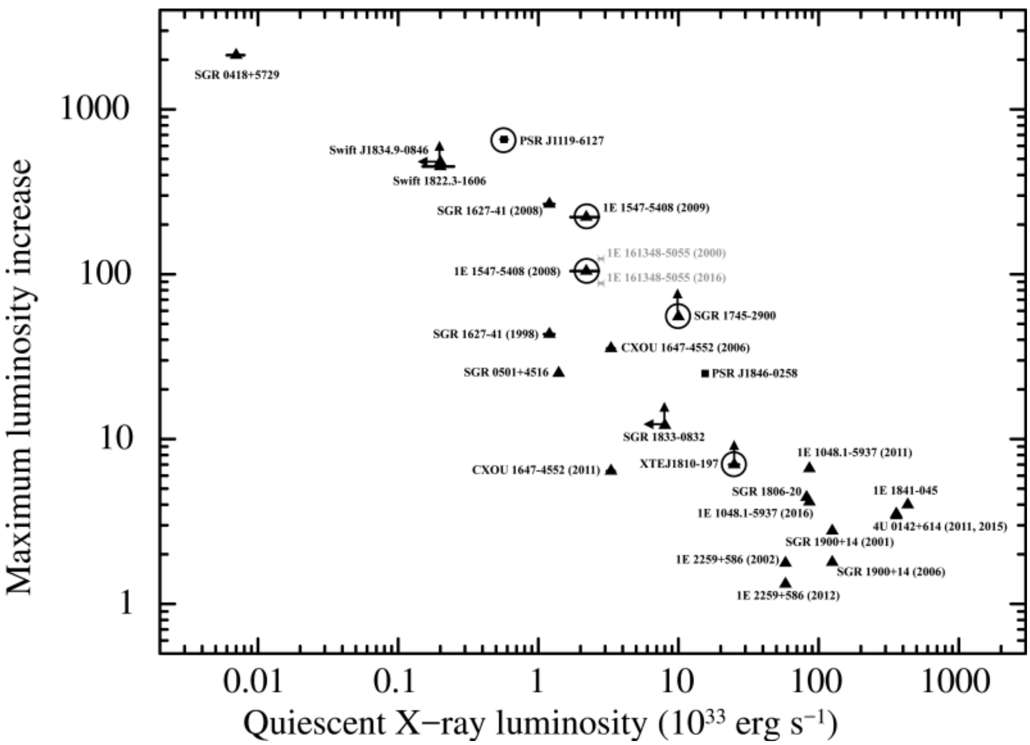

Figure 3. Maximum X-ray luminosity increase versus quiescent X-ray luminosity.

and after both episodes the source reached the same minimum flux level, which we identify as the bona fide quiescent one (see Fig. B1 for the *Swift* XRT light curve). 4U 0142+61 showed repeated low-level variability on top of its persistent emission on at least two occasions, in 2011 July and 2015 February (Archibald et al. 2017b).[14] 1E 1841−045 also showed sporadic bursting/flaring activity between 2010 May and 2011 July (a total of nine bursts

[14] An additional magnetar-like burst in 2017 July was recently reported by Hamburg (2017).

were indeed recorded by *Swift* BAT and *Fermi* GBM), and some deviation from the source historical persistent X-ray flux has been noticed between 2008 and 2011 (Lin et al. 2011). The source has been subsequently monitored by *Swift* XRT about 145 times until the end of 2017 April. Finally, a recent analysis by Scholz et al. (2014a) showed that the flux of magnetar 1RXS J170849.0−4009 remained constant within uncertainties between 2003 and 2013, in contradiction with what reported by Götz et al. (2007). In particular, the maximum variability for the X-ray flux is constrained to be lower than 10 per cent over this decade. We also verified that the source flux remained approximately steady between 2013 April and 2017 May by visually inspecting the long-term X-ray light curve generated using all the *Swift* XRT observations carried out during this period (which also covers the epoch of the detection of a magnetar-like burst, on 2017 February 17; see Archibald, Scholz & Kaspi 2017c). In light of these characteristics, we decided not to include this source in our sample.

For each magnetar, spectra relative to the first observation following the outburst onset were used to measure accurately fluxes and luminosities at the very early phases of the outburst. For the sources showing low-level variability (see above), we extracted and fitted the spectrum relative to the observation where the source is found at the highest flux ever. Table 5 lists the inferred values. The quiescent 0.3–10 keV fluxes and luminosities for all magnetars monitored so far are reported in Table 4. Bolometric luminosities are also quoted. We also calculated the flux during pre-outburst observations (if available), and considered the lowest value historically to estimate the quiescent level. For the sources where only low-level variability has been reported, we focused on the observations with high counting statistics to derive the persistent flux.

In all cases, the spectra were fitted using thermal models (i.e. one or multiple blackbody components) or the NTZ model, to avoid possible overestimates in the values for the fluxes introduced when fitting a power-law model to the data. For *ROSAT* data, we extrapolated the 0.3–2.4 keV fluxes using the DUMMYRSP tool. For the cases where the source is not detected, we applied the SRCFLUX task of CIAO (for the *Chandra* observations of Swift J1834.9−0846 and SGR 1745−2900) and the EUPPER tool of SAS (for the *XMM–Newton* observation of SGR 1833−0832) to derive 3σ upper limits on the net count rates at the source position (the background was estimated locally). We found values of 2×10^{-4}, 1.1×10^{-3} and 7×10^{-4} counts s^{-1} for Swift J1834.9−0846, SGR 1745−2900 and SGR 1833−0832, respectively. We then assumed a blackbody spectral model with $kT = 0.3$ keV (similarly to what observed in other quiescent magnetars; see e.g. table 3 by Olausen & Kaspi 2014), and the same column density derived from the joint spectral fits of the outburst decay, to infer upper limits on the fluxes with the Portable, Interactive Multi-Mission Simulator (PIMMS, v. 4.8; Mukai 1993).

7 SEARCH FOR CORRELATIONS

Our systematic analysis allows us to search for correlations between different parameters for all sources of our sample and their outbursts, in particular between parameters measured in this work (e.g. quiescent luminosity, maximum luminosity, maximum luminosity increase, outburst energetics and time-scale) and the timing-inferred parameters (e.g. surface dipolar magnetic field, rotational energy loss rate, characteristic age).

Table 3 reports the most up-to-date values for the spin period and the spin-down rate for our sample of magnetars, and for the other sources we included in our correlation study (see below). We list the strength of the surface dipolar component of the magnetic field at the pole, the spin-down luminosity and characteristic age (all estimated assuming simple magnetic dipole braking in vacuo, the initial spin period to be much smaller than the current value and no variation of the magnetic field in time). Several magnetars displayed a high level of timing noise in their rotational evolution across the outburst decay, and significant deviations from simple spin-down were often detected. For these cases we assumed a long-term average value for the spin-down rate to infer the characteristic parameters, following Olausen & Kaspi (2014).

Table 6 reports the significance for the (anti)correlations among several different combinations of parameters. The significance was evaluated from the two-sided null-hypothesis probability (p-value) obtained from the Spearman and Kendall τ rank correlation tests. We did not include upper limit measurements in our computations, but verified that the reported upper limits were consistent with the observed trend for all cases where a significant ($>2\sigma$) correlation or anticorrelation was observed. The table also reports on the shape of the (anti)correlation. The power-law index was estimated for each case via a power-law regression test based on the least squares fitting method (only for the cases where the significance for the correlation was above 2σ). The table also indicates whether the observed/unobserved correlation/anticorrelation fits either the internal crustal cooling model (Perna & Pons 2011; Pons & Perna 2011; Pons & Rea 2012) or the untwisting bundle model (Beloborodov 2009) proposed to account for the evolution of magnetar outbursts (see also Section 8).

All plots are shown in Figs 3–8. In all figures, the black triangles denote all magnetars of our sample; black squares represent the high-field rotation-powered pulsars that underwent an outburst (i.e. PSR J1119−6127 and PSR J1846−0258) and the grey cross denotes 1E 161348−5055. The year of outburst onset is indicated in parentheses for sources that underwent more than one luminosity enhancement. To have a more complete sample, we included also the other few magnetars (black stars), the central compact objects (grey crosses), the rotation-powered pulsars clearly showing a thermal component in their spectra (red diamonds) and the X-ray dim isolated neutron stars (orange crosses) already reported by Viganò et al. (2013; see in particular their table 1 for a list and their section 2 for the criteria adopted to select the sample). PSR J1119−6127 and the magnetars XTE J1810−197, 1E 1547−5408 and SGR 1745−2900, for which radio pulsed emission was detected (Camilo et al. 2006, 2007; Eatough et al. 2013), are marked by black circles. Upper and lower limits are indicated by black arrowheads.

8 DISCUSSION

We carried out the first systematic study of all sources experiencing magnetar-like outbursts up to the end of 2016, and for which extensive X-ray monitoring campaigns of their outbursts are available. We re-analysed in a coherent way about 1100 X-ray observations, adopting the same assumptions and spectral models throughout the whole sample. This work allows us to study possible correlations and anticorrelations between several different combinations of parameters, and put the results in the context of the models proposed to explain the triggering mechanism and evolution of magnetar outbursts.

Table 5. Maximum fluxes and luminosities (0.3–10 keV) for magnetars showing major outbursts or variations in their persistent emission. The table is ordered according to the chronological order of the outburst episodes, and the cases of the peculiar high *B*-field pulsars and the CCO 1E 161348−5055 are reported below the double horizontal line. Uncertainties are reported at the 1σ c.l.

Source	Date	Observatory	Obs. ID	Exposure (ks)	Abs/Unabs flux (erg cm^{-2} s^{-1})	$L_{X,p}$ (erg s^{-1})
SGR 1627−41	1998 Aug 07	*BeppoSAX*	70566001	44.9	$(2.4 \pm 0.1) \times 10^{-12}$ $(3.6 \pm 0.2) \times 10^{-12}$	$(5.2 \pm 0.3) \times 10^{34}$
SGR 1900+14	2001 Apr 22	*Chandra*	2458	20.1	$(1.02 \pm 0.02) \times 10^{-11}$ $(1.86 \pm 0.05) \times 10^{-11}$	$(3.48 \pm 0.09) \times 10^{35}$
1E 2259+586	2002 Jun 21	*XMM–Newton*	0155350301	18.4	$(5.87 \pm 0.01) \times 10^{-11}$ $(1.006 \pm 0.009) \times 10^{-10}$	$(1.23 \pm 0.01) \times 10^{35}$
XTE J1810−197	2003 Sep 08	*XMM–Newton*	0161360301	6.6	$(3.84 \pm 0.02) \times 10^{-11}$ $(1.19 \pm 0.01) \times 10^{-10}$	$(1.74 \pm 0.01) \times 10^{35}$
SGR 1806−20	2004 Oct 06	*XMM–Newton*	0164561101	12.9	$(2.68 \pm 0.02) \times 10^{-11}$ $(4.0 \pm 0.1) \times 10^{-11}$	$(3.62 \pm 0.09) \times 10^{35}$
SGR 1900+14	2006 Mar 29	*Chandra*	6709	40.0	$(6.10 \pm 0.09) \times 10^{-12}$ $(1.20 \pm 0.03) \times 10^{-11}$	$(2.24 \pm 0.06) \times 10^{35}$
CXOU J1647−4552	2006 Sep 21	*Swift*	00030806001	7.7	$(3.36 \pm 0.08) \times 10^{-11}$ $(6.1 \pm 0.5) \times 10^{-11}$	$(1.2 \pm 0.1) \times 10^{35}$
SGR 1627−41	2008 May 28	*Swift*	00312579001	2.0	$(1.2 \pm 0.2) \times 10^{-11}$ $(2.2 \pm 0.4) \times 10^{-11}$	$(3.2 \pm 0.6) \times 10^{35}$
SGR 0501+4516	2008 Aug 23	*XMM–Newton*	0560191501	33.8	$(4.03 \pm 0.01) \times 10^{-11}$ $(1.28 \pm 0.08) \times 10^{-10}$	$(3.4 \pm 0.2) \times 10^{34}$
1E 1547−5408	2008 Oct 03	*Swift*	00330353000	4.1	$(6.2 \pm 0.2) \times 10^{-11}$ $(9.4 \pm 0.7) \times 10^{-11}$	$(2.3 \pm 0.2) \times 10^{35}$
1E 1547−5408	2009 Jan 23	*Swift*	00340923000	1.7	$(8.2 \pm 0.5) \times 10^{-11}$ $2.0^{+1.4}_{-0.4} \times 10^{-10}$	$5^{+3}_{-1} \times 10^{35}$
SGR 0418+5729	2009 Jun 11	*RXTE*	94048-03-01-00	5.2	$(3.31 \pm 0.06) \times 10^{-11}$ $(3.41 \pm 0.06) \times 10^{-11}$	$(1.63 \pm 0.03) \times 10^{34}$
SGR 1833−0832[a]	2010 Mar 20	*Swift*	00416485000	29.0	$(4.0 \pm 0.2) \times 10^{-12}$ $(8.5 \pm 0.7) \times 10^{-12}$	$(1.02 \pm 0.08) \times 10^{35}$
1E 1841−045	2011 Jul 02	*Swift*	00456505000	1.4	$(2.0 \pm 0.2) \times 10^{-11}$ $(2 \pm 1) \times 10^{-10}$	$(1.7 \pm 0.9) \times 10^{36}$
Swift J1822.3−1606	2011 Jul 16	*Swift*	00032033001	1.6	$(2.35 \pm 0.04) \times 10^{-10}$ $(2.61 \pm 0.05) \times 10^{-10}$	$(8.0 \pm 0.2) \times 10^{34}$
4U 0142+61	2011 Jul 29	*Swift*	00458345000	3.9	$(6.7 \pm 0.3) \times 10^{-10}$ $(7.9 \pm 0.2) \times 10^{-10}$	$(1.23 \pm 0.03) \times 10^{36}$
Swift J1834.9−0846	2011 Aug 07	*Swift*	00458907000	1.5	$(3.2 \pm 0.6) \times 10^{-11}$ $(4.8 \pm 0.8) \times 10^{-11}$	$(1.0 \pm 0.2) \times 10^{35}$
CXOU J1647−4552	2011 Sep 25	*Swift*	00030806020	3.1	$(6.5 \pm 0.5) \times 10^{-12}$ $(1.1 \pm 0.2) \times 10^{-11}$	$(2.1 \pm 0.4) \times 10^{34}$
1E 1048.1−5937	2011 Dec 31	*Swift*	00031220066	2.0	$(4.6 \pm 0.3) \times 10^{-11}$ $(5.9 \pm 0.4) \times 10^{-11}$	$(5.7 \pm 0.4) \times 10^{35}$
1E 2259+586	2012 Apr 28	*Swift*	00032035021	3.9	$(5.7 \pm 0.1) \times 10^{-11}$ $(7.5 \pm 0.2) \times 10^{-11}$	$(9.2 \pm 0.2) \times 10^{34}$
SGR 1745−2900	2013 Apr 29	*Chandra*[b]	14701	9.7	$\sim 1.8 \times 10^{-11}$ $\sim 8.3 \times 10^{-11}$	$\sim 6.8 \times 10^{35}$
SGR 1935+2154[c]	2014 Jul 05	*Swift*	00603488000	3.4	$(1.7 \pm 0.2) \times 10^{-12}$ $(2.6 \pm 0.4) \times 10^{-12}$	$(2.5 \pm 0.4) \times 10^{34}$
4U 0142+61	2015 Feb 28	*Swift*	00632888000	0.5	$(6.5 \pm 0.3) \times 10^{-10}$ $(8.1 \pm 0.1) \times 10^{-10}$	$(1.26 \pm 0.02) \times 10^{36}$
1E 1048.1−5937	2016 Jul 29	*Swift*	00032923249	1.4	$(3.16 \pm 0.2) \times 10^{-11}$ $(3.8 \pm 0.1) \times 10^{-11}$	$(3.7 \pm 0.1) \times 10^{35}$
PSR J1119−6127	2016 Jul 28	*Swift*	00706396000	2.2	$(4.1 \pm 0.2) \times 10^{-11}$ $(4.4 \pm 0.1) \times 10^{-11}$	$(3.72 \pm 0.08) \times 10^{35}$
PSR J1846−0258[d]	2006 Jun 08	*RXTE*	92012-01-14-00	20.1	$\sim 1.2 \times 10^{-11}$ $\sim 9 \times 10^{-11}$	$\sim 3.9 \times 10^{35}$
1E 161348−5055	2000 Feb 08	*Chandra*	970	18.9	$(6.5 \pm 1.6) \times 10^{-11}$ $(2.66 \pm 0.06) \times 10^{-10}$	$(3.47 \pm 0.08) \times 10^{35}$
1E 161348−5055	2016 Jun 22	*Swift*	00030389032	0.6	$(1.4 \pm 0.1) \times 10^{-10}$ $(1.9 \pm 0.1) \times 10^{-10}$	$(2.5 \pm 0.1) \times 10^{35}$

Notes. [a]A distance of 10 kpc was assumed.
[b]The field around the source has been previously observed by *Swift*. In order to avoid contamination by nearby active X-ray sources, we consider here the first *Chandra* observation, which was carried out with the HRC. The flux was then estimated by assuming a blackbody model at 0.9 keV and the column density inferred from the joint fits of all *Chandra* data sets, i.e. $N_H = 1.87 \times 10^{23}$ cm^{-2}.
[c]A distance of 9 kpc was assumed.
[d]We used PIMMS to convert the absorbed 2–10 keV pulsed flux reported by Kuiper & Hermsen (2009) into unabsorbed 0.3–10 keV fluxes and luminosities.

Table 6. Results of the search for (anti)correlations between different parameters. Letters in parentheses indicate the case of a correlation (c) or an anticorrelation (a). The decay-time-scale is defined as the *e*-folding parameter (τ) and it refers to the larger value (the parameter τ_2 in Table 1) for the cases where the outburst decay curve was modelled by more than one exponential function. Values for the significance are not reported if below 2σ. The 'yes' / 'no' flag in the last column indicates if a correlation or anticorrelation is predicted by either the internal crustal cooling or the untwisting bundle models for the evolution of magnetar outbursts (see the text for more details).

First parameter	Second parameter	Corr (c) or anticorr (a), Significance (σ) for Spearman/Kendall τ tests	PL index	Reference figure	Correlation expected? Internal cooling / untwisting bundle
Quiescent X-ray luminosity	Maximum luminosity increase	(a), 5.7 / 4.9	−0.7	Fig. 3	Yes/yes
Spin-down luminosity	Quiescent bolometric luminosity	–	–	Fig. 4	No/no
Dipolar magnetic field	Quiescent bolometric luminosity	(c), 3.2 / 2.9	2.0	Fig. 4	Does not apply
Dipolar magnetic field	Maximum luminosity	(c), 2.5 / 2.4	0.5	Fig. 5	Yes/yes
Dipolar magnetic field	Decay time-scale	–	–	Fig. 5	Yes/yes
Dipolar magnetic field	Outburst energy	(c), 3.7 / 3.3	1.0	Fig. 6	Yes/yes
Characteristic age	Outburst energy	(a), 3.3 / 3.0	−0.4	Fig. 6	Yes/?
Maximum luminosity	Outburst energy	(c), 4.0 / 3.7	1.4	Fig. 6	Yes/yes
Quiescent bolometric luminosity	Outburst energy	–	–	Fig. 6	No/no
Maximum luminosity	Decay time-scale	–	–	Fig. 7	No/no
Outburst energy	Decay time-scale	(c), 3.9 / 3.6	0.5	Fig. 7	Yes/yes
Outburst energy	Maximum luminosity increase	–	–	Fig. 8	No/no
Decay time-scale	Maximum luminosity increase	–	–	Fig. 8	No/no

8.1 On the relation between the outburst luminosity increase and the quiescent luminosity

A few years ago, Pons & Rea (2012) showed how magnetars with low quiescent luminosities ($L_q \sim 10^{31}$–10^{33} erg s^{-1}) experience large luminosity increases during an outburst, whereas the brightest sources in quiescence ($L_q \sim 10^{34}$–10^{35} erg s^{-1}) undergo only subtle enhancements in luminosity. This discovery clarified that the distinction between 'transient' and 'persistent' sources within the magnetar population is deceptive, and only dependent on the initial quiescent luminosity of each source.

The anticorrelation between magnetars quiescent luminosities and their luminosity increases is observed at a significance of 5.7σ (according to the Spearman test; see Table 5 and Fig. 3), and suggests the existence of a limiting luminosity of $\sim 10^{36}$ erg s^{-1} for magnetar outbursts (regardless of the quiescent level of the source). This result was interpreted in the framework of the internal crustal heating model as the observational manifestation of the self-regulating effect resulting from the strong temperature-dependence of the neutrino emissivity (Pons & Rea 2012): the surface photon luminosity for injected energies larger than $\sim 10^{43}$ erg reaches a limiting value of $\sim 10^{36}$ erg s^{-1}, because the crust is so hot that most of the energy is released in the form of neutrinos before reaching the star surface. The observed anticorrelation is expected also in the untwisting magnetospheric bundle model, where the maximum theoretically predicted luminosity could be somewhat higher, a few 10^{36} erg s^{-1} for the generous case of a twist with $\psi \sim 1$ rad extended to a large part of the magnetospheric volume. The generally lower values observed for the peak luminosity are interpreted, in this model, as a consequence of the limited size of the current bundle and the twist (Beloborodov 2009).

We used our updated sample (see Fig. 3) to gauge the general trend of this anticorrelation via a power-law regression test:

$$\Delta L_{\rm X} \equiv \frac{L_{\rm X,peak}}{L_{\rm X,q}} \propto L_{X,{\rm q}}^{-0.7}. \quad (4)$$

We observed a similar trend when considering fluxes, suggesting a weak dependence on the sources distance.

We note that, although there is no observational bias in detecting large luminosity increases in sources with a high quiescent luminosity (see the empty regions on the top-right corners of Fig. 3), the lack of detections of weak outbursts in magnetars with a low quiescent level (see the empty regions on the bottom-left corners of Fig. 3) might follow from the lack of sufficient sensibility of the current all sky X-ray monitors in detecting relatively subtle outbursts in low-luminosity sources.

We also point out that, throughout this study, the epoch of the outburst onset was defined as the time of the first burst detection from the source (mostly with *Swift* BAT or *Fermi* GBM), or of the giant flare in the case of SGR 1806−20. This is a somewhat arbitrary choice, because the increase of the persistent flux during the time interval preceding the detection of magnetars bursting/flaring activity is usually missed by X-ray instruments. In some cases (e.g. CXOU J164710.2−455216 and SGR 1745−2900; see Muno et al. 2007 and Kennea et al. 2013b, respectively), the time-scale for the flux rise was constrained to be shorter than a couple of days, but this might not be necessarily the case for all magnetars. However, given the large sample, and the clear trend observed over several orders of magnitude, we do not expect to measure significantly different values for the outburst peak luminosity.

Different estimates on the time-scale of the luminosity increase were proposed in the past years. The internal crustal cooling models by Pons & Rea (2012) show that the internal heat wave takes some time to propagate from the location in the crust where the energy is injected up to the surface layers. Therefore, the luminosity increase is not instantaneous but relatively fast, and might range from a few hours up to a few days depending on the depth of the region where heat is released. On the other hand, simplified one-dimensional models show that the time-scale of magnetospheric twisting by a large thermoplastic wave (corresponding to the rise time of the outburst) can span from days to weeks (Li et al. 2016). Within the large uncertainties, both models are compatible with a typical rise time of a few days.

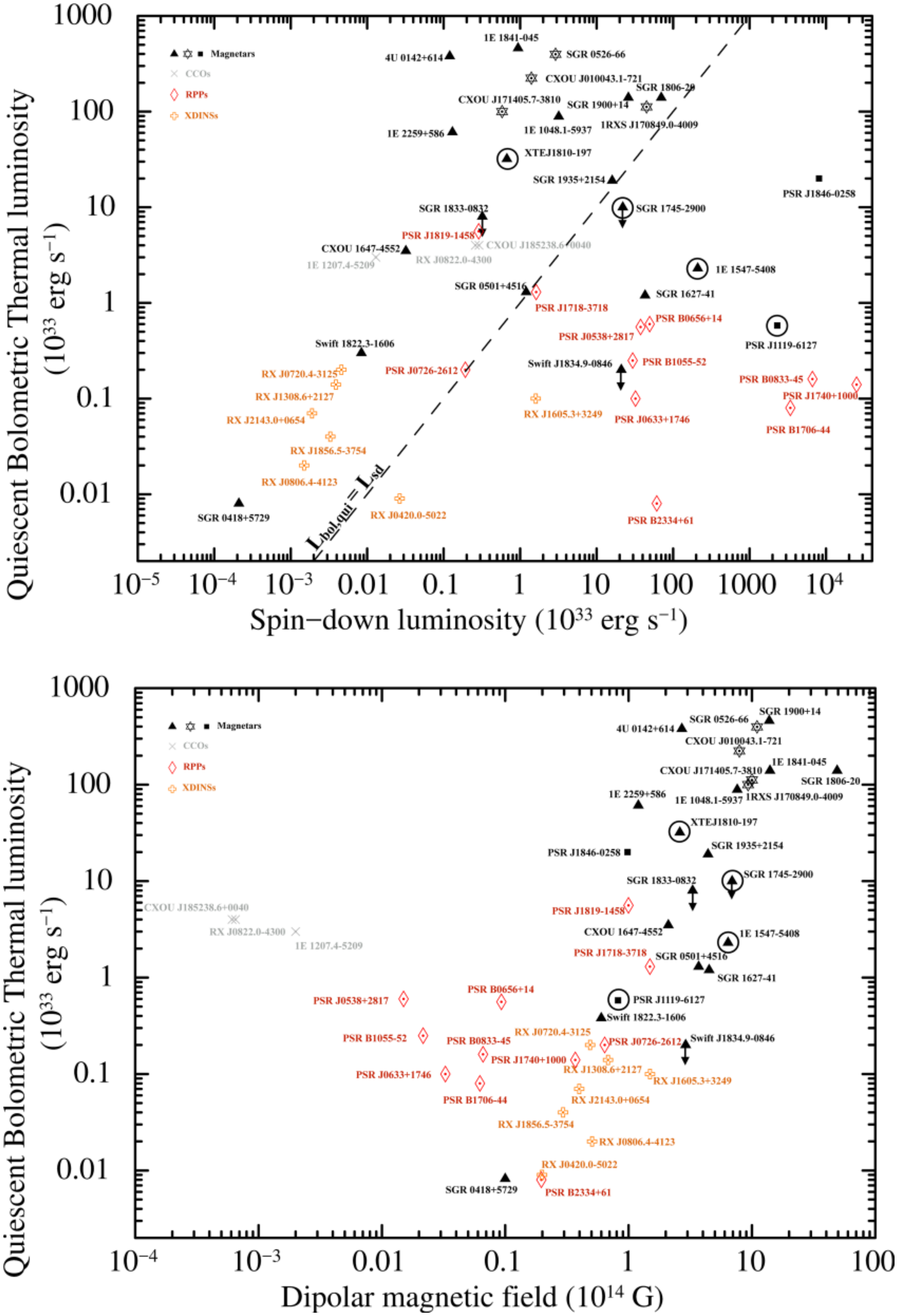

Figure 4. *Top panel*: quiescent bolometric luminosity relative to the thermal component versus the rotational energy loss rate for all isolated X-ray pulsars with clear thermal emission. The black dashed line marks the region on the diagram where the bolometric luminosity equals the spin-down luminosity. *Bottom panel*: quiescent bolometric luminosity relative to the thermal component versus the dipolar component of the magnetic field. In both figures, black triangles refer to the 'canonical' magnetars of our sample, black stars indicate magnetars that did not experience outburst activity, black squares denote the rotation-powered pulsars with high magnetic field that showed magnetar-like activity, light grey crosses are the central compact objects, red diamond the rotation-powered pulsars selected by Viganò et al. (2013) and orange crosses refer to the X-ray dim isolated neutron stars.

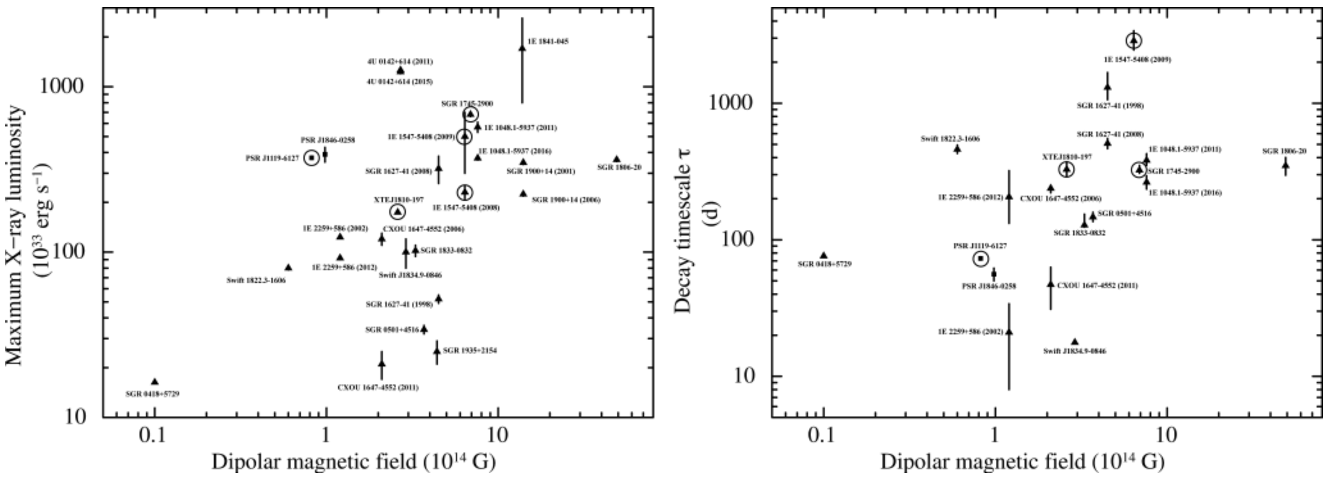

Figure 5. *Left-hand panel*: maximum X-ray luminosity as a function of the dipolar component of the magnetic field. *Right-hand panel*: decay time-scale as a function of the dipolar component of the magnetic field.

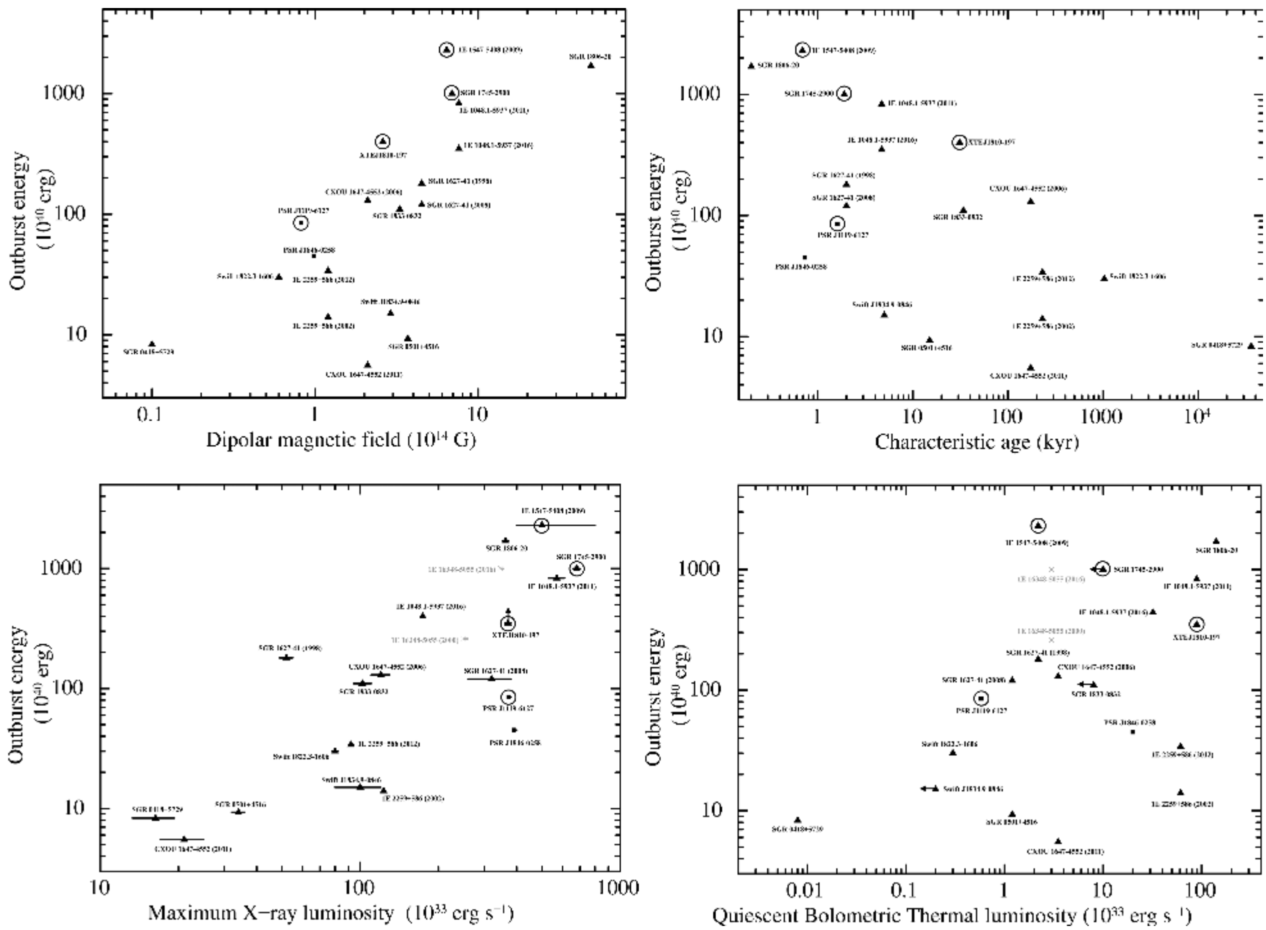

Figure 6. *Top panels*: total energy released during the outburst as a function of the dipolar component of the magnetic field (left), and total energy released during the outburst as a function of the characteristic age (right). *Bottom panels*: total energy released during the outburst versus maximum X-ray luminosity at the peak of the outburst (left), and total energy released during the outburst as a function of the quiescent bolometric luminosity relative to the thermal component (right).

8.2 On the quiescent luminosity versus the spin-down luminosity and the dipolar magnetic field

The top panel of Fig. 4 reports the quiescent thermal bolometric luminosity ($L_{\rm bol,\,q}$) of magnetars and of the other classes of isolated X-ray pulsars as a function of their spin-down luminosity ($\dot{E}_{\rm rot}$). The dashed line represents $L_{\rm bol,q} = \dot{E}_{\rm rot}$. The emission of all sources lying above the dashed line must be ultimately powered by magnetic energy. On the other hand, the emission of all sources located below the dashed line might be entirely rotation-powered, or switch between magnetar-like and rotation-powered emission. An interesting

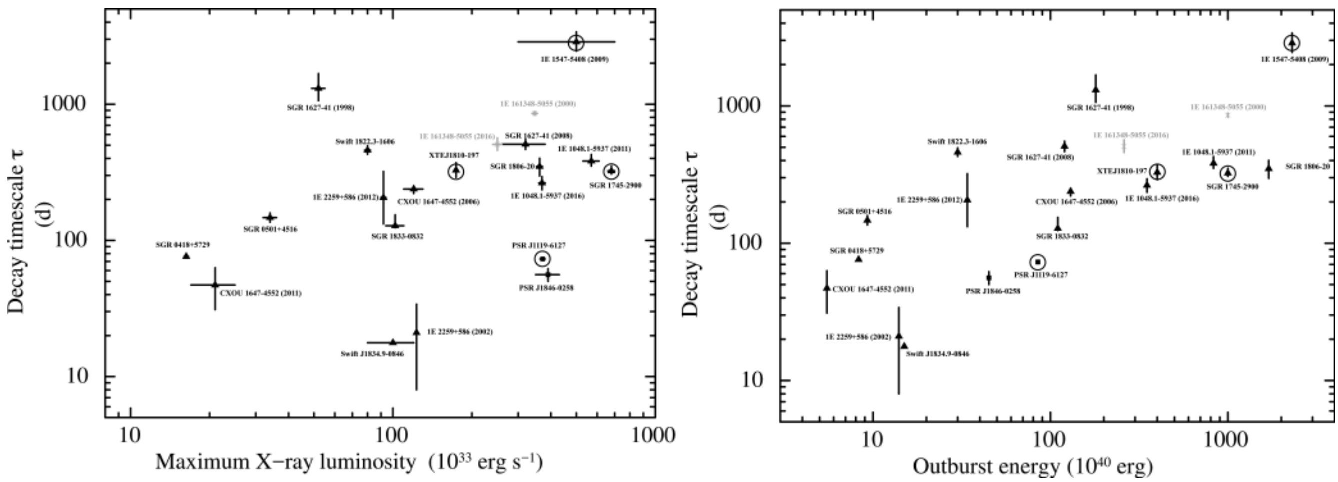

Figure 7. *Left-hand panel*: decay time-scale as a function of the maximum X-ray luminosity at the peak of the outburst. *Right-hand panel*: decay time-scale as a function of the total energy released during the outburst.

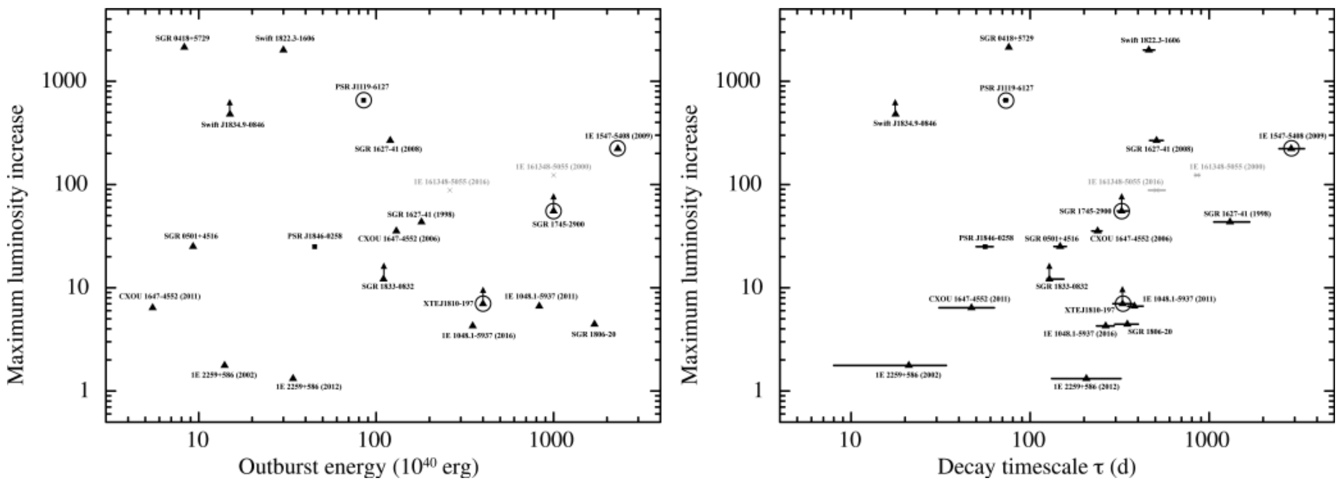

Figure 8. *Left-hand panel*: maximum luminosity increase as a function of the total energy released during the outburst. *Right-hand panel*: maximum luminosity increase as a function of the decay time-scale.

case is represented by the magnetar XTE J1810−197, whose steady, quiescent, luminosity, $L_{\rm bol,\,q} \sim 4 \times 10^{34}$ erg s^{-1} attained in the past $\sim$5 yr (see Fig. D3) is a factor of $\sim$60 larger than its spin-down luminosity $\dot{E}_{\rm rot} \sim 6.7 \times 10^{32}$ erg s^{-1}, accurately estimated from timing analysis of X-ray data taken over the last 12 yr (see Table 3). This result contradicts the prediction put forward by Rea et al. (2012b), according to which a magnetar with $L_{\rm X,q} \gtrsim \dot{E}_{\rm rot}$ is expected to be radio quiet, regardless of its possible X-ray outburst activity.

The bottom panel of Fig. 4 shows the quiescent thermal bolometric luminosity as a function of the surface dipolar magnetic field. We observe a significant correlation (3.2σ according to the Spearman test) when including all sources belonging to the different classes considered in this study (the correlation is 3.9σ after excluding the central compact objects). This correlation is naturally explained in terms of magnetic field decay and Joule heating (Pons, Miralles & Geppert 2009; Viganò et al. 2013). The central compact objects clearly depart from the general trend. The peculiar behaviour of these objects might be explained in the framework of the 'hidden magnetic field' scenario: hypercritical accretion on to the neutron star surface during the initial stages of the star life can bury a magnetic field of a few 10^{13} G into the inner crust, yielding a strength for the external magnetic field that is significantly lower than the internal 'hidden' magnetic field. The large luminosity observed for these objects is most probably due to the toroidal and higher order mulipolar components of the magnetic field trapped inside the crust (Geppert, Page & Zannias 1999; Ho 2011; Shabaltas & Lai 2012; Viganò & Pons 2012; Torres-Forné et al. 2016). The magnetic field will eventually re-emerge, after a few thousands of years, settling on a value comparable to that at birth. If this picture is correct, we would expect a 'shift' of the central compact objects towards the right in the quiescent luminosity versus dipolar magnetic field diagram, as the CCOs get older. Some of the rotation-powered pulsars also depart slightly from the observed trend (e.g. PSR J0538+2817, PSR B1055−52 and PSR J0633+1746). This might be possibly due to an additional contribution to the surface heating from slamming particles on to the stellar surface, as typically observed for pulsars with a high rotational energy loss rate.

We investigated the shape of the correlation via a power-law regression test, and found

$$L_{\rm bol,q} \propto B^2_{\rm p,dip} \qquad (5)$$

(see Table 6). This is in agreement with the dependence reported by Pons et al. (2007) using a reduced sample of sources.

8.3 On the dipolar magnetic field versus the outburst properties

We also investigated possible correlations between the strength of the surface dipolar magnetic field and all the outburst parameters derived in this work. There is no significant correlation between the magnetic field and either the maximum luminosity or the decay time-scale. Furthermore, in a few cases the same source was observed to undergo two different outbursts with distinct properties (see Fig. 5).

The correlation between the magnetic field and the outburst energetics is more evident (3.4σ according to the Spearman test; see Fig. 6), and supports the idea that the energy reservoir of the outbursts is mainly provided by the dissipation of the magnetic field. The two variables are linearly related (i.e. $E \propto B_{\rm p,\,dip}$). We observe a sort of limiting energy as a function of age. Young magnetars tend to experience more energetic outbursts than older magnetars, a characteristic that can be explained simply in terms of field decay. The expected energetics distribution was estimated by Perna & Pons (2011), who did not find a significant dependence of the energy of the events with age, but the fact that magnetic field decay limits the energy budget available for old magnetars, compared to young sources. They also estimated the recurrence times between consecutive outbursts, and found as a general trend that the older the object, the longer the average recurrence time.

8.4 On the outburst energy versus other properties

The outburst energy correlates with the peak luminosity reached during the outburst (at a significance of 4.0σ according to the Spearman test), but not with the quiescent X-ray luminosity ($<2\sigma$; see Fig. 6). These results suggest that a larger luminosity at the peak of the outburst results in a larger energy released during the entire outburst event, regardless of the quiescent level of the source, and reflect similar decay patterns for magnetar outbursts. This is expected in both internal crustal cooling and untwisting bundle scenarios, since it only reflects the normalization of the decay curve.

The energetics correlates significantly with the decay time-scale (at a significance of 3.9σ according to the Spearman test): the longer the outburst, the more energetic (Fig. 7). This suggests again that the decay pattern is similar from outburst to outburst. For example, we never observe a magnetar undergoing a rather weak outburst and then returning to quiescence over an extremely long time interval, or a magnetar showing an extremely powerful outburst and then rapidly decaying back to quiescence.

9 THE MAGNETAR OUTBURST ONLINE CATALOGUE

All the key parameters derived for the magnetar outbursts presented in this study, as well as the reduced spectral files, are available at the MOOC (http://magnetars.ice.csic.es). We have also included all important parameters for the other thermally emitting isolated X-ray pulsars (see Table 3; see also Viganò et al. 2013), to allow a direct comparison between the different classes of isolated neutron stars.

The webpage consists of three distinct sections: `Sources`, `Analysis` and `Download`. In the `Sources` section, the user can plot any combination of the parameters for all thermally emitting isolated X-ray pulsars. In the `Analysis` section, the user can plot the light curves for all magnetar outbursts, as well as any combination of the parameters characterizing these events.

In both the `Sources` and `Analysis` sections, a detailed description of all parameters is provided, and the user can download all values of the plotted parameters in the form of a *csv* table. Furthermore, restricted ranges of values can be selected and plotted using the 'Filter' task. The user can also create mathematical functions linking different parameters via the 'Create Function Field' tool, and download the resulting plot as an image or an ascii file.

Finally, in the `Download` section, the user can download the fits files relative to all the observations of magnetar outbursts analysed in this study, i.e. the source and background average spectra, the redistribution matrix files and the auxiliary response files. Each file is named according to the following general scheme: 'source name_name of the satellite_type of file_obsID.fits', where 'type of file' is either src_spectrum, bg_spectrum, rmf or arf. The user can perform a spectral analysis of the data by uploading these files in the XSPEC spectral fitting package.

The webpage will be updated periodically and expanded as new outbursts are observed.

ACKNOWLEDGEMENTS

We are indebted to Martin Folger and Santiago Serrano Elorduy from the Institute of Space Sciences (IEEC–CSIC) for designing the Magnetar Outburst Online Catalogue and implementing several plotting and analysis online tools. FCZ acknowledges Alice Borghese, Niccolò Bucciantini and Jason Hessels for useful suggestions that helped improving a preliminary version of the manuscript, Alexander Kaminker and Stefano Carignano for useful discussions, and Chichuan Jin for providing the *Chandra* ACIS-S version of the dust scattering model for Galactic Centre X-ray sources. We thank the referee for comments. The scientific results reported in this study are based on observations obtained with the *Chandra X-ray Observatory*, *XMM–Newton*, *Swift* and *RXTE*. *XMM–Newton* is an ESA science mission with instruments and contributions directly funded by ESA Member States and the National Aeronautics and Space Administration (NASA). *Swift* is a NASA/UK/ASI mission. *RXTE* is a NASA mission. This research has made extensive use of software provided by the *Chandra X-ray Center* [operated for and on behalf of NASA by the Smithsonian Astrophysical Observatory (SAO) under contract NAS8–03060] in the application package CIAO. The *XMM–Newton* SAS is developed and maintained by the Science Operations Centre at the European Space Astronomy Centre. We made use of data supplied by the UK *Swift* Science Data Centre at the University of Leicester and of the XRT Data Analysis Software (XRTDAS) developed under the responsibility of the ASI Science Data Center (ASDC), Italy. We also used softwares and tools provided by the High Energy Astrophysics Science Archive Research Center (HEASARC) Online Service, which is a service of the Astrophysics Science Division at NASA/GSFC and the High Energy Astrophysics Division of SAO. We made use of the McGill Online Magnetar Catalog (www.physics.mcgill.ca/~pulsar/magnetar/main.html) and NASA's Astrophysics Data System Bibliographic Services. FCZ, NR and PE acknowledge funding in the framework of the Netherlands Organization for Scientific Research (NWO) Vidi award number 639.042.321 (PI: N. Rea) and the European COST Action MP1304 (NewCOMPSTAR). FCZ and NR are also supported by grants AYA2015-71042-P and SGR2014-1073. JAP acknowledges support by grants AYA2015-66899-C2-2-P and PROMETEOII-2014-069.

REFERENCES

Alford J. A. J., Halpern J. P., 2016, ApJ, 818, 122
An H., Kaspi V. M., Archibald R. F., Cumming A., 2013, ApJ, 763, 82

An H., Kaspi V. M., Tomsick J. A., Cumming A., Bodaghee A., Gotthelf E. V., Rahoui F., 2012, ApJ, 757, 68
Anders E., Grevesse N., 1989, Geochim. Cosmochim. Acta, 53, 197
Archibald R. F. et al., 2013, Nature, 497, 591
Archibald R. F., Kaspi V. M., Ng C.-Y., Scholz P., Beardmore A. P., Gehrels N., Kennea J. A., 2015, ApJ, 800, 33
Archibald R. F., Kaspi V. M., Tendulkar S. P., Scholz P., 2016a, ApJ, 829, L21
Archibald R. F., Tendulkar S. P., Scholz P., Kaspi V. M., 2016b, Astron. Telegram, 9316, 1
Archibald R. F. et al., 2017a, ApJ, 849, 20
Archibald R. F., Kaspi V. M., Scholz P., Beardmore A. P., Gehrels N., Kennea J. A., 2017b, ApJ, 834, 163
Archibald R. F., Scholz P., Kaspi V. M., 2017c, Astron. Telegram, 10107, 1
Arnaud K. A., 1996, in Jacoby G. H., Barnes J., eds, ASP Conf. Ser. Vol. 101, Astronomical Data Analysis Software and Systems V. Astron. Soc. Pac., San Francisco, p. 17
Barthelmy S. D. et al., 2005, Space Sci. Rev., 120, 143
Barthelmy S. D. et al., 2008, Astron. Telegram, 1676, 1
Barthelmy S. D., Kennea J. A., Krimm H. A., Mangano V., Markwardt C. B., Marshall F. E., Maselli A., 2013, GCN Circ. 14443
Barthelmy S. D., D'Avanzo P., Kennea J. A., Melandri A., Palmer D. M., 2016, GCN Circ. 19447
Baumgartner W. H. et al., 2011, GCN Circ. 12359
Beloborodov A. M., 2009, ApJ, 703, 1044
Beloborodov A. M., Levin Y., 2014, ApJ, 794, L24
Beloborodov A. M., Li X., 2016, ApJ, 833, 261
Beloborodov A. M., Thompson C., 2007, ApJ, 657, 967
Bernardini F. et al., 2009, A&A, 498, 195
Bernardini F., Perna R., Gotthelf E. V., Israel G. L., Rea N., Stella L., 2011a, MNRAS, 418, 638
Bernardini F. et al., 2011b, A&A, 529, 19
Bevington P. R., 1969, Data Reduction and Error Analysis for the Physical Science. McGraw-Hill, New York
Blackburn J. K., 1995, in Shaw R. A., Payne H. E., Hayes J. J. E., eds, ASP Conf. Ser. Vol. 77, Astronomical Data Analysis Software and Systems IV. Astron. Soc. Pac., San Francisco, p. 367
Boella G. et al., 1997, A&AS, 122, 327
Bower G. C. et al., 2015, ApJ, 798, 120
Burrows D. N. et al., 2005, Space Sci. Rev., 120, 165
Camero A. et al., 2014, MNRAS, 438, 329
Camilo F., Kaspi V. M., Lyne A. G., Manchester R. N., Bell J. F., D'Amico N., McKay N. P. F., Crawford F., 2000, ApJ, 541, 367
Camilo F., Ransom S. M., Halpern J. P., Reynolds J., Helfand D. J., Zimmerman N., Sarkissian J., 2006, Nature, 442, 892
Camilo F., Ransom S. M., Halpern J. P., Reynolds J., 2007, ApJ, 666, 93
Camilo F. et al., 2016, ApJ, 820, 110
Capalbi M., Perri M., Saija B., Tamburelli F., Angelini L., 2005, Technical Report 1.2, The Swift XRT Data Reduction Guide
Cash W., 1979, ApJ, 228, 939
Connaughton V., Briggs M., 2009, GCN Circ. 8835, 1
Coti Zelati F. et al., 2015a, MNRAS, 449, 2685
Coti Zelati F., Campana S., Israel G. L., Rea N., Mereghetti S., Esposito P., Tiengo A., 2015b, Astron. Telegram, 8449, 1
Coti Zelati F. et al., 2017, MNRAS, 471, 1819
Crawford F., Gaensler B. M., Kaspi V. M., Manchester R. N., Camilo F., Lyne A. G., Pivovaroff M. J., 2001, ApJ, 554, 152
Cummings J. R., Burrows D., Campana S., Kennea J. A., Krimm H. A., Palmer D. M., Sakamoto T., Zane S., 2011, Astron. Telegram, 3488, 1
D'Aì A. et al., 2016, MNRAS, 463, 2394
D'Avanzo P., Burrows D. N., Gehrels N., Kennea J. A., Krimm H. A., Marshall F. E., Sakamoto T., Sbarufatti B., 2015, Astron. Telegram, 7123, 1
D'Elia V. et al., 2011, GCN Circ. 12253
Davis J. E., 2001, ApJ, 562, 575
De Luca A., Molendi S., 2004, A&A, 419, 837
De Luca A., Caraveo P. A., Mereghetti S., Tiengo A., Bignami G. F., 2006, Science, 313, 814
De Luca A., Mignani R. P., Zaggia S., Beccari G., Mereghetti S., Caraveo P. A., Bignami G. F., 2008, ApJ, 682, 1185
Dib R., Kaspi V. M., Scholz P., Gavriil F. P., 2012, ApJ, 748, 3
Dib R., Kaspi V. M., 2014, ApJ, 784, 37
Duncan R. C., Thompson C., 1992, ApJ, 392, L9
Eatough R. et al., 2013, Astron. Telegram, 5058, 1
Enoto T. et al., 2010a, PASJ, 62, 475
Enoto T. et al., 2010b, ApJ, 715, 665
Enoto T. et al., 2017, ApJS, 231, 8
Esposito P. et al., 2007, A&A, 476, 321
Esposito P. et al., 2008, MNRAS, 390, 34
Esposito P. et al., 2009a, ApJ, 690, L105
Esposito P. et al., 2009b, MNRAS, 399, 44
Esposito P. et al., 2010a, MNRAS, 405, 1787
Esposito P., Israel G. L., Stella L., Rea N., Tiengo A., 2010b, Astron. Telegram, 2494, 1
Esposito P. et al., 2011, MNRAS, 416, 205
Esposito P. et al., 2013, MNRAS, 429, 3123
Evans P. A. et al., 2007, A&A, 469, 379
Evans P. A. et al., 2009, MNRAS, 397, 1177
Fahlman G. G., Gregory P. C., 1981, Nature, 293, 202
Foley S., Kouveliotou C., Kaneko Y., Collazzi A., 2012, GCN Circ. 13280
Freeman P. E., Kashyap V., Rosner R., Lamb D. Q., 2002, ApJS, 138, 185
Fruscione A. et al., 2006, in Silva D. R., Doxsey R. E., eds, Proc. SPIE Conf. Ser. Vol. 6270, Observatory Operations: Strategies, Processes, and Systems. SPIE, Bellingham, p. 62701V
Gabriel C. et al., 2004, in F. Ochsenbein, M. G. Allen, D. Egret, eds, ASP Conf. Ser. Vol. 314, Astronomical Data Analysis Software and Systems (ADASS) XIII. Astron. Soc. Pac., San Francisco, p. 759
Garmire G. P., Bautz M. W., Ford P. G., Nousek J. A., Ricker G. R., Jr, 2003, in Truemper J. E., Tananbaum H. D., eds, Proc. SPIE Conf. Ser. Vol. 4851, X-Ray and Gamma-Ray Telescopes and Instruments for Astronomy. SPIE, Bellingham, p. 28
Gavriil F. P., Gonzalez M. E., Gotthelf E. V., Kaspi V. M, Livingstone M. A., Woods P. M., 2008, Science, 319, 1802
Gehrels N., 1986, ApJ, 303, 336
Gelbord J. M. et al., 2010, GCN Circ. 10526
Gelfand J. D., Gaensler B. M., 2007, ApJ, 667, 1111
Geppert U., Page D., Zannias T., 1999, A&A, 345, 847
Gotthelf E. V., Halpern J. P., 2005, ApJ, 632, 1075
Gotthelf E. V., Vasisht G., Boylan-Kolchin M., Torii K., 2000, ApJ, 542, 37
Gotthelf E. V., Halpern J. P., Buxton M., Bailyn C., 2004, ApJ, 605, 368
Götz et al., 2007, A&A, 475, 317
Göğüş E., Kouveliotou C., 2011, Astron. Telegram, 3542, 1
Göğüş E., Woods P., Kouveliotou C., 2008, Astron. Telegram, 1677, 1
Göğüş E., Woods P., Kouveliotou C., 2009, Astron. Telegram, 2121, 1
Göğüş E. et al., 2010a, ApJ, 718, 331
Göğüş E., Woods P. M., Kouveliotou C., Kaneko Y., Gaensler B. M., Chatterjee S., 2010b, ApJ, 722, 899
Göğüş E., Kouveliotou C., Strohmayer T., 2011a, Astron. Telegram, 3491, 1
Göğüş E., Güver T., Özel F., Eichler D., Kouveliotou C., 2011b, ApJ, 728, 160
Göğüş E. et al., 2016, ApJ, 829, 25
Granot J., Gill R., Younes G., Gelfand J., Harding A., Kouveliotou C., Baring M. G., 2017, MNRAS, 464, 4895
Gronwall C., Holland S. T., Markwardt C. B., Palmer D. M., Stamatikos M., Vetere L., 2009, GCN Circ. 8833
Guiriec S., Kouveliotou C., van der Horst A. J., 2011, GCN Circ. 12255
Halpern J. P., Gotthelf E. V., 2005, ApJ, 618, 874
Halpern J. P., Gotthelf E. V., Reynolds J., Ransom S. M., Camilo F., 2008, ApJ, 676, 1178
Hamburg R., 2017, GCN Circ. 21342
Hill J. E. et al., 2004, in Flanagan K. A., Siegmund O. H. W., eds, Proc. SPIE Conf. Ser. Vol. 5165, X-Ray and Gamma-Ray Instrumentation for Astronomy XIII. SPIE, Bellingham, p. 217
Ho W. C. G., 2011, MNRAS, 414, 2567
Hoversten E. A. et al., 2011, GCN Circ. 12316

Hurley K. et al., 1999, Nature, 397, 41
Hurley K. et al., 2005, Nature, 434, 1098
Ibrahim A. I. et al., 2004, ApJ, 609, 21
Israel G. L., Campana S., Dall'Osso S., Muno M. P., Cummings J., Perna R., Stella L., 2007, ApJ, 664, 448
Israel G. L. et al., 2010, MNRAS, 408, 1387
Israel G. L., Rea N., Coti Zelati F., Esposito P., Burgay M., Mereghetti S., Possenti A., Tiengo A., 2014, Astron. Telegram, 6370, 1
Israel G. L. et al., 2016, MNRAS, 457, 3448
Jahoda K., Markwardt C. B., Radeva Y., Rots A. H., Stark M. J., Swank J. H., Strohmayer T. E., Zhang W., 2006, ApJS, 163, 401
Jin C., Ponti G., Haberl F., Smith R., 2017, MNRAS, 468, 2532
Kaastra J. S., Bleeker J. A. M., 2016, A&A, 587, 151
Kargaltsev O. et al., 2012, ApJ, 748, 26
Kaspi V. M., Beloborodov A. M., 2017, ARA&A, 55, 261
Kaspi V. M., Gavriil F. P., Woods P. M., Jensen J. B., Roberts M. S. E., Chakrabarty D., 2003, ApJ, 588, 93
Kaspi V. M. et al., 2014, ApJ, 786, 84
Kennea J. A. et al., 2013a, Astron. Telegram, 5009, 1
Kennea J. A. et al., 2013b, ApJ, 770, 24
Kennea J. A., Lien A. Y., Marshall F. E., Palmer D. M., Roegiers T. G. R., Sbarufatti B., 2016, GCN Circ. 19735
Kouveliotou C., 1998, GCN Circ. 107
Kouveliotou C. et al., 1998, Nature, 393, 235
Kouveliotou C. et al., 2003, ApJ, 596, 79
Krimm H., Barthelmy S., Campana S., Cummings J., Israel G. L., Palmer D., Parsons A, 2006, Astron. Telegram, 894, 1
Krimm H. et al., 2008, GCN Circ. 8311
Kuiper L., Hermsen W., 2009, A&A, 501, 1031
Kuiper L., Hermsen W., den Hartog P. R., Urama J. O., 2012, ApJ, 748, 133
Kumar H. S., Safi-Harb S., 2008, ApJ, 678, 43
Lamb R. C., Markert T. H., 1981, ApJ, 244, 94
Lampton M., Margon B., Bowyer S., 1976, ApJ, 208, 177
Laros J. G., Fenimore E. E., Fikani M. M., Klebesadel R. W., Barat C., 1986, Nature, 322, 152
Laros J. G. et al., 1987, ApJ, 320, 111
Li X., Beloborodov A. M., 2015, ApJ, 815, 25
Li X., Levin Y., Beloborodov A. M., 2016, ApJ, 833, 189
Lin L. et al., 2011, ApJ, 740, 16
Livingstone M. A., Ng C.-Y., Kaspi V. M., Gavriil F. P., Gotthelf E. V., 2011a, ApJ, 730, 66
Livingstone M. A., Scholz P., Kaspi V. M., Ng C.-Y., Gavriil F. P., 2011b, ApJ, 743, 38
Markevitch M. et al., 2003, ApJ, 583, 70
Mathis J. S., Rumpl W., Nordsieck K. H., 1977, ApJ, 217, 425
Mazets E. P. et al., 1981, Ap&SS, 80, 3
Mereghetti S. et al., 2005, ApJ, 628, 938
Mereghetti S. et al., 2006, A&A, 450, 759
Mereghetti S., Esposito P., Tiengo A., 2007, Ap&SS, 308, 13
Mereghetti S. et al., 2009, ApJ, 696, L74
Mereghetti S., Götz D., Ferrigno C., Bozzo E., Borkowski J., 2015, GCN Circ. 18711, 1
Moretti A. et al., 2005, in Siegmund O. H. W., ed., Proc. SPIE Conf. Ser. Vol. 5898, UV, X-Ray, and Gamma-Ray Space Instrumentation for Astronomy XIV. SPIE, Bellingham, p. 348
Mukai K., 1993, Legacy, 3, 21
Muno M. P. et al., 2006, ApJ, 636, 41
Muno M. P., Gaensler B. M., Clark J. S., de Grijs R., Pooley D., Stevens I. R., Portegies Zwart S. F., 2007, MNRAS, 378, 44
Murakami T., Tanaka Y., Kulkarni S. R., Ogasaka Y., Sonobe T., Ogawara Y., Aoki T., Yoshida A., 1994, Nature, 368, 127
Neilsen J. et al., 2013, ApJ, 774, 42
Ng C.-Y. et al., 2011, ApJ, 729, 131
Nobili L., Turolla R., Zane S., 2008a, MNRAS, 386, 1527
Nobili L., Turolla R., Zane S., 2008b, MNRAS, 389, 989
Olausen S. A., Kaspi V. M., 2014, ApJS, 212, 6
Paczyński B., 1992, Acta Astron., 42, 145
Palmer D. M. et al., 2004, GCN Circ. 2925, 1
Palmer D. M. et al., 2005, Nature, 434, 1107
Palmer D. M. et al., 2008, Astron. Telegram, 1548, 1
Parfrey K., Beloborodov A. M., Hui L., 2013, ApJ, 774, 92
Perna R., Pons J. A., 2011, ApJ, 727, L51
Pfeffermann E. et al., 1987, in Koch E.-E., Schmahl G., eds, Proc. SPIE Conf. Ser. Vol. 733, Soft X-ray Optics and Technology. SPIE, Bellingham, p. 519
Pintore F. et al., 2016, MNRAS, 458, 2088
Pons J. A., Perna R., 2011, ApJ, 741, 123
Pons J. A., Rea N., 2012, ApJ, 750, L6
Pons J. A., Link B., Miralles J. A., Geppert U., 2007, Phys. Rev. Lett., 98, 071101
Pons J. A., Miralles J. A., Geppert U., 2009, A&A, 496, 207
Press W. H., Teukolsky S. A., Vetterling W. T., Flannery B. P., 1992, Numerical Recipes in FORTRAN: The Art of Scientific Computing, 2nd edn. Cambridge Univ. Press, Cambridge
Rea N., Esposito P., 2011, in Torres D. F., Rea N., eds, Astrophysics and Space Science Proceedings, High-Energy Emission from Pulsars and Their Systems, Vol. 21. Springer-Verlag, Berlin, p. 247
Rea N. et al., 2004, A&A, 425, 5
Rea N. et al., 2009, MNRAS, 396, 2419
Rea N. et al., 2010, Science, 330, 944
Rea N. et al., 2012a, ApJ, 754, 27
Rea N., Pons J. A., Torres D. F., Turolla R., 2012b, ApJ, 748, L12
Rea N. et al., 2013a, ApJ, 770, 65
Rea N. et al., 2013b, ApJ, 775, L34
Rea N., Borghese A., Esposito P., Coti Zelati F., Bachetti M., Israel G. L., De Luca A., 2016, ApJ, 828, L13
Rodríguez Castillo G. A., Israel G. L., Esposito P., Pons J. A., Rea N., Turolla R., Viganò D., Zane S., 2014, MNRAS, 441, 1305
Rodríguez Castillo G. A. et al., 2016, MNRAS, 456, 4145
Scholz P., Kaspi V. M., 2011, ApJ, 739, 94
Scholz P., Ng C.-Y., Livingstone M. A., Kaspi V. M., Cumming A., Archibald R. F., 2012, ApJ, 761, 66
Scholz P., Archibald R. F., Kaspi V. M., Ng C.-Y., Beardmore A. P., Gehrels N., Kennea J. A., 2014a, ApJ, 783, 99
Scholz P., Kaspi V. M., Cumming A., 2014b, ApJ, 786, 62
Seward F. D., Charles P. A., Smale A. P., 1986, ApJ, 305, 814
Shabaltas N., Lai D., 2012, ApJ, 748, 148
Smith, 2016, (available at http://xmm2.esac.esa.int/docs/documents/CAL-TN-0018.pdf)
Smith R. K., Valencic L. A., Corrales L., 2016, ApJ, 818, 143
Sonobe T., Murakami T., Kulkarni S. R., Aoki T., Yoshida A., 1994, ApJ, 436, 23
Spitkovsky A., 2006, ApJ, 648, L51
Stamatikos M., Malesani D., Page K. L., Sakamoto T., 2014, GCN Circ. 16520
Strüder L. et al., 2001, A&A, 365, 18
Thompson C., Duncan R. C., 1993, ApJ, 408, 194
Thompson C., Duncan R. C., 1995, MNRAS, 275, 255
Thompson C., Duncan R. C., 1996, ApJ, 473, 322
Thompson C., Duncan R. C., 2001, ApJ, 561, 980
Thompson C., Lyutikov M., Kulkarni S. R., 2002, ApJ, 574, 332
Tiengo A., Esposito P., Mereghetti S., Rea N., Stella L., Israel G. L., Turolla R., Zane S., 2005, A&A, 440, 63
Tiengo A., Esposito P., Mereghetti S., 2008, ApJ, 680, L133
Tiengo A. et al., 2010, ApJ, 710, 227
Torres D. F., 2017, ApJ, 835, 54
Torres-Forné A., Cerdá-Durán P., Pons J. A., Font J. A., 2016, MNRAS, 456, 3813
Tsujimoto M. et al., 2011, A&A, 525, 25
Turner M. J. L. et al., 2001, A&A, 365, 110
Turolla R., Zane S., Watts A., 2015, Rep. Progr. Phys., 78, 116901
van der Horst A. J. et al., 2009, Astron. Telegram, 2077, 1
van der Horst A. J. et al., 2010, ApJ, 711, 1
Verner D. A., Ferland G. J., Korista K. T., Yakovlev D. G., 1996, ApJ, 465, 487
Viganò D., Pons J. A., 2012, MNRAS, 425, 2487

Viganò D., Rea N., Pons J. A., Perna R., Aguilera D. N., Miralles J. A., 2013, MNRAS, 434, 123
Weingartner J. C., Draine B. T., 2001, ApJ, 548, 296
Wilms J., Allen A., McCray R., 2000, ApJ, 542, 914
Woods P. M., Kaspi V. M., Gavriil F. P., Airhart C., 2011, ApJ, 726, 37
Woods P. M. et al., 1999, ApJ, 519, 139
Woods P. M. et al., 2004, ApJ, 605, 378
Younes G., Kouveliotou C., Kaspi V. M., 2015, ApJ, 809, 165
Younes G., Kouveliotou C., Roberts O., 2016, GCN Circ. 19736
Younes G. et al., 2016, ApJ, 824, 138
Younes G. et al., 2017, ApJ, 847, 85
Zhu W., Kaspi V. M., Dib R., Woods P. M., Gavriil F. P., Archibald A. M., 2008, ApJ, 686, 520
Zombeck M. V., Chappell J. H., Kenter A. T., Moore R. W., Murray S. S., Fraser G. W., Serio S., 1995, in Siegmund O. H., Vallerga J. V., eds, Proc. SPIE Conf. Ser. Vol. 2518, EUV, X-Ray, and Gamma-Ray Instrumentation for Astronomy VI. SPIE, Bellingham, p. 96
Zubko V., Dwek E., Arendt R. G., 2004, ApJS, 152, 211

APPENDIX A: JOURNAL OF OBSERVATIONS

This Section provides a log of all observations carried out by the X-ray instruments on board the *Swift*, *XMM–Newton*, *Chandra* and *BeppoSAX* satellites, relative to the magnetar outbursts that were analysed in our study. The tables are reported following the chronological order of the outburst onsets (spanning a time interval of ~18 yr, from 1998 to 2016). We give references to previous papers where part of the listed observations have been already analysed. For every single observation, each table lists:

(i) the X-ray instrument (legend: XRT = X-ray Telescope on board *Swift*; EPN = pn CCD of the EPIC camera on board *XMM–Newton*; ACIS-S = Advanced CCD Imaging Spectrometer spectroscopic array on board *Chandra*; ACIS-I = Advanced CCD Imaging Spectrometer imaging array on board *Chandra*; MECS = Medium-Energy Concentrator Spectrometer on board *BeppoSAX*);

(ii) the operating mode of the X-ray instrument (legend: PC = photon counting; WT = windowed timing; FF = full frame; LW = large window: SW = small window; TE = timed exposure; CC = continuous clocking);

(iii) the mid-point of the observation expressed in modified Julian date (MJD);

(iv) the time (in units of days) elapsed from the outburst onset, which is defined as the epoch when the first burst was detected in the hard X-/soft γ-rays from the target of interest as reported by the 'Gamma-ray Burst Coordinates Network' (http://gcn.gsfc.nasa.gov/gcn3_archive.html) and/or 'The Astronomer's Telegram' website (http://www.astronomerstelegram.org/). Two exceptions to this definition are represented by the magnetars XTE J1810−197 and 1E 1048.1−5937, as discussed in Sections 2.3 and 2.12, respectively;

(v) the exposure time after filtering for intrinsic source flares and bursts and, in the case of the *XMM–Newton* and *Chandra* data sets, also for particle background flaring;

(vi) the background-subtracted count rate of the source (in units of counts s^{-1}) in the 0.3–10 keV energy band. Count rates are corrected for point spread function and vignetting effects, but not for pile-up.

Table A1. Log of all X-ray observations of SGR 1627−41 following the 1998 June outburst. The outburst onset occurred on MJD 50979.109 (Kouveliotou 1998). Two additional *XMM–Newton* observations (obs. ID: 0204500201, 0204500301, pn in FF mode) were not included because the source was detected at an off-axis angle of about 9.6 arcmin in these cases, leading to a too poor statistics for a meaningful spectral analysis. Part of these observations were already analysed by Woods et al. (1999), Kouveliotou et al. (2003), Mereghetti et al. (2006) and Esposito et al. (2008, 2009a,b).

Instrument	Mode	Obs. ID	Mid-point of observation (MJD)	Time since outburst onset (d)	Exposure (ks)	Source net count rate (counts s^{-1})
BeppoSAX/MECS[a]	–	70566001	51032.25	53.14	44.9	0.0200 ± 0.0008
BeppoSAX/MECS[a]	–	70566002	51072.51	93.41	30.4	0.0153 ± 0.0008
BeppoSAX/MECS[a]	–	70821005	51399.77	420.66	80.4	0.0060 ± 0.0005
BeppoSAX/MECS[a]	–	70821001	51793.58	814.47	61.3	0.0034 ± 0.0005
Chandra ACIS-S	TE	1981	52182.50	1203.39	48.9	0.0049 ± 0.0003
Chandra ACIS-S	TE	3877	52722.33	1743.22	25.7	0.0059 ± 0.0005
XMM–Newton EPN	SW	0202560101	53270.98	2291.87	35.9	0.023 ± 0.002
Chandra ACIS-S	TE	5573	53549.28	2570.17	9.8	0.0042 ± 0.0007
Chandra ACIS-S	TE	5574	53668.54	2689.43	10.0	0.0038 ± 0.0006
XMM–Newton EPN	FF	0502140101	54509.28	3530.17	47.5	0.0083 ± 0.0008

Note. [a]Data acquired by the LECS were not considered, owing to the large value for the column density towards the source direction (the LECS is best calibrated for spectral analysis in the 0.1–4 keV range).

Table A2. Log of all X-ray observations of SGR 1627−41 following the 2008 May outburst. The outburst onset occurred on MJD 54614.34841435 (Palmer et al. 2008). Part of these observations were already analysed by Esposito et al. (2008, 2009a,b) and An et al. (2012).

Instrument	Mode	Obs. ID	Mid-point of observation (MJD)	Time since outburst onset (d)	Exposure (ks)	Source net count rate (counts s^{-1})
Swift XRT	PC	00312579001	54614.55	0.20	2.0	0.058 ± 0.006
Swift XRT	PC	00312579002	54615.65	1.30	2.0	0.017 ± 0.003
Swift XRT	PC	00312579003	54616.55	2.21	1.9	0.007 ± 0.002
Swift XRT	PC	00312579004	54617.41	3.06	1.8	0.009 ± 0.003
Swift XRT	PC	00312579005	54618.27	3.93	2.0	0.010 ± 0.002
Swift XRT	PC	00312579006	54619.40	5.05	2.1	0.009 ± 0.002
Chandra ACIS-S	CC	9126	54620.68	6.33	40.0	0.029 ± 0.002
Swift XRT	PC	00312579007	54 623.48	9.13	0.6	< 0.01[a]
Swift XRT	PC	00312579008	54626.65	12.30	0.3	<0.02[a]
Swift XRT	PC	00312579009	54629.62	15.27	1.9	0.006 ± 0.002
Swift XRT	PC	00312579010	54632.26	17.91	3.8	0.005 ± 0.001
Swift XRT	PC	00312579011	54635.78	21.43	2.3	0.010 ± 0.002
Swift XRT	PC	00312579012	54638.88	24.54	5.2	0.007 ± 0.001
Swift XRT	PC	00312579013	54649.47	35.12	1.5	0.004 ± 0.002
Swift XRT	PC	00312579014	54652.78	38.43	5.6	0.005 ± 0.001
Swift XRT	PC	00312579015	54664.76	50.41	7.0	0.0047 ± 0.0009
Swift XRT	PC	00312579016	54678.64	64.29	5.2	0.006 ± 0.001
Swift XRT	PC	00312579017	54680.14	65.80	1.7	0.002 ± 0.001
Swift XRT	PC	00312579018	54723.19	108.84	3.2	0.003 ± 0.001
Swift XRT	PC	00312579019	54724.26	109.91	0.6	<0.007[a]
Swift XRT	PC	00312579020	54725.19	110.84	3.5	0.002 ± 0.001
Swift XRT	PC	00312579022	54732.09	117.75	3.2	0.005 ± 0.001
XMM–Newton EPN	FF	0560180401	54734.76	120.41	94.7	0.0226 ± 0.0005
Chandra ACIS-S	TE	10519	54856.86	242.51	6.6	0.018 ± 0.002
Chandra ACIS-I	TE	12528[b]	55728.17	1113.83	19.0	0.0026 ± 0.0004
Chandra ACIS-I	TE	12529[b]	55728.41	1114.06	19.0	0.0027 ± 0.0004
XMM–Newton EPN	FF	0742650101	57071.56	2457.21	19.1	0.0046 ± 0.0007

Notes. [a]The upper limit is quoted at the 3σ c.l., and is derived by applying the prescription for low number statistics given by Gehrels (1986). The corresponding upper limits on the fluxes and luminosities were estimated by assuming an absorbed blackbody spectral model with the same parameters as those of the spectra of the closeby observations.
[b]The spectral files and responses of these observations were combined to improve the fit statistics.

Table A3. Log of all X-ray observations of 1E 2259+586 following the 2002 June outburst. The outburst onset occurred on MJD 52443.66 (Kaspi et al. 2003). An additional *Chandra* observation (obs. ID: 6730, ACIS-S in TE mode) was not included owing to the combination of severe pile-up and extended emission (due to both the SNR surrounding the source and a halo from dust scattering) beyond a radial distance of about 4 arcsec. Part of these observations were already analysed by Woods et al. (2004) and Zhu et al. (2008).

Instrument	Mode	Obs. ID	Mid-point of observation (MJD)	Time since outburst onset (d)	Exposure (ks)	Source net count rate (counts s^{-1})
XMM–Newton EPN	SW	0155350301	52446.60	2.94	18.4	17.92 ± 0.03
XMM–Newton EPN	FF	0057540201	52464.45	20.79	5.7	4.52 ± 0.03
XMM–Newton EPN	FF	0057540301	52464.68	21.02	10.1	4.89 ± 0.02
XMM–Newton EPN	SW	0203550301	53055.63	611.97	3.8	10.47 ± 0.05
XMM–Newton EPN	SW	0203550601	53162.70	719.04	4.9	10.33 ± 0.05
XMM–Newton EPN	SW	0203550401	53178.66	735.00	3.6	10.41 ± 0.05
XMM–Newton EPN	SW	0203550501	53358.04	914.38	3.6	10.22 ± 0.05
XMM–Newton EPN	SW	0203550701	53580.00	1136.34	3.5	9.98 ± 0.05

Table A4. Log of X-ray observations of 1E 2259+586 following the 2012 April outburst and up to the return to quiescence. The outburst onset occurred on MJD 56038.34564479 (Foley et al. 2012). One *Chandra* observation was performed with the HRC-I (obs. ID: 15265), and was not included in our analysis. Part of these observations were already analysed by Archibald et al. (2013).

Instrument	Mode	Obs. ID	Mid-point of observation (MJD)	Time since outburst onset (d)	Exposure (ks)	Source net count rate (counts s^{-1})
Swift XRT	WT	00032035021	56045.45	7.10	3.9	1.74 ± 0.02
Swift XRT	WT	00032035022	56049.06	10.71	6.6	1.68 ± 0.02
Swift XRT	WT	00032035023	56054.41	16.07	3.9	1.65 ± 0.02
Swift XRT	WT	00032035026	56075.37	37.03	3.9	1.15 ± 0.02
Swift XRT	WT	00032035029	56096.55	58.20	1.1	1.47 ± 0.04
Swift XRT	WT	00032035033	56124.02	85.68	0.9	0.99 ± 0.03
Swift XRT	WT	00032035036	56161.80	123.46	1.9	1.44 ± 0.03
Swift XRT	WT	00032035037	56166.77	128.43	1.0	1.38 ± 0.04
Swift XRT	WT	00032035040	56208.62	170.28	2.9	0.86 ± 0.02
Swift XRT	WT	00032035041	56215.64	177.30	2.9	1.31 ± 0.02
Swift XRT	WT	00032035042	56222.54	184.20	2.7	1.21 ± 0.02
Swift XRT	WT	00032035046	56246.12	207.77	1.4	1.46 ± 0.03
Swift XRT	WT	00032035049	56264.91	226.56	3.3	1.34 ± 0.02
Swift XRT	WT	00032035051	56274.47	236.12	2.8	1.42 ± 0.02
Swift XRT	WT	00032035052	56292.33	253.98	3.2	1.13 ± 0.02
Swift XRT	WT	00032035055	56355.68	317.33	3.3	0.66 ± 0.01
Swift XRT	WT	00032035056	56376.48	338.13	2.9	1.31 ± 0.02
Swift XRT	WT	00032035057	56397.81	359.47	3.4	1.24 ± 0.02
Swift XRT	WT	00032035058	56418.11	379.77	3.7	1.30 ± 0.02
Swift XRT	WT	00032035061	56481.50	443.16	3.2	1.27 ± 0.02
Swift XRT	WT	00032035062	56502.49	464.15	3.5	1.28 ± 0.02
Swift XRT	WT	00032035065	56565.61	527.27	1.6	0.94 ± 0.02
Swift XRT	WT	00032035069	56632.89	594.55	1.5	1.38 ± 0.03
Swift XRT	WT	00032035072	56692.59	654.24	3.2	1.17 ± 0.02
Swift XRT	WT	00032035073	56712.55	674.20	3.3	1.25 ± 0.02
Swift XRT	WT	00032035076	56776.29	737.95	3.4	1.18 ± 0.02
Swift XRT	WT	00032035077	56797.59	759.25	2.7	1.22 ± 0.02
Swift XRT	WT	00032035079	56839.51	801.16	2.9	1.11 ± 0.02
Swift XRT	WT	00032035083	56902.72	864.38	3.5	1.25 ± 0.02
Swift XRT	WT	00032035084	56923.61	885.26	2.0	1.24 ± 0.03
Swift XRT	WT	00032035087	56965.22	926.88	3.3	1.16 ± 0.02
Swift XRT	WT	00032035088	56986.31	947.97	4.0	1.07 ± 0.02
Swift XRT	WT	00032035089	57007.77	969.43	2.6	1.17 ± 0.02
Swift XRT	WT	00032035091	57028.59	990.25	5.5	0.97 ± 0.01
Swift XRT	WT	00032035092	57049.20	1010.86	1.3	1.02 ± 0.03
Swift XRT	WT	00032035093	57070.48	1032.13	3.9	1.21 ± 0.02
Swift XRT	WT	00032035096	57133.39	1095.04	3.9	0.89 ± 0.02
Swift XRT	WT	00032035097	57154.58	1116.23	3.3	1.15 ± 0.02
Swift XRT	WT	00032035101	57196.43	1158.09	1.2	1.10 ± 0.03
Swift XRT	WT	00032035104	57204.93	1166.59	0.6	1.17 ± 0.05
Swift XRT	WT	00032035107	57260.71	1222.37	3.8	0.96 ± 0.02
Swift XRT	WT	00032035108	57286.61	1248.26	3.5	0.97 ± 0.02
Swift XRT	WT	00032035114	57343.45	1305.11	3.2	1.31 ± 0.02

Table A5. Log of all *XMM–Newton* observations of XTE J1810−197 following the 2003 outburst. The outburst onset was missed and is constrained to be in the range MJD 52595–52662 (Ibrahim et al. 2004). Part of these observations were already analysed by Rea et al. (2004), Gotthelf et al. (2004), Halpern & Gotthelf (2005), Gotthelf & Halpern (2005), Bernardini et al. (2009, 2011a), Alford & Halpern (2016), Camilo et al. (2016) and Pintore et al. (2016).

Instrument	Mode	Obs. ID	Mid-point of observation (MJD)	Time since outburst onset (d)	Exposure (ks)	Source net count rate (counts s^{-1})
XMM–Newton EPN	SW	0161360301	52890.61	229–296	6.6	10.04 ± 0.04
XMM–Newton EPN	LW	0161360501	53075.59	414–481	2.5	5.50 ± 0.05
XMM–Newton EPN	LW	0164560601	53266.66	605–672	21.5	3.57 ± 0.01
XMM–Newton EPN	LW	0301270501	53448.23	786–853	32.3	1.832 ± 0.008
XMM–Newton EPN	LW	0301270401	53633.68	972–1039	28.3	0.919 ± 0.006
XMM–Newton EPN	LW	0301270301	53807.03	1145–1212	21.3	0.641 ± 0.006
XMM–Newton EPN	LW	0406800601	54002.34	1340–1407	39.8	0.493 ± 0.004
XMM–Newton EPN	LW	0406800701	54166.12	1504–1571	36.7	0.459 ± 0.004
XMM–Newton EPN	LW	0504650201	54359.48	1698–1765	67.0	0.455 ± 0.003
XMM–Newton EPN	LW	0552800201	54896.02	2234–2301	30.3	0.418 ± 0.004
XMM–Newton EPN	LW	0605990201	55079.73	2418–2485	17.9	0.423 ± 0.005
XMM–Newton EPN	LW	0605990301	55081.66	2420–2487	16.3	0.418 ± 0.005
XMM–Newton EPN	LW	0605990401	55097.77	2436–2503	11.1	0.419 ± 0.006
XMM–Newton EPN	LW	0605990501	55295.23	2633–2700	3.5	0.43 ± 0.01
XMM–Newton EPN	LW	0605990601	55444.73	2783–2850	8.4	0.428 ± 0.007
XMM–Newton EPN	LW	0671060101	55654.19	2992–3059	16.0	0.430 ± 0.005
XMM–Newton EPN	LW	0671060201	55813.46	3152–3219	12.0	0.418 ± 0.006
XMM–Newton EPN	LW	0691070301	56177.07	3515–3582	14.6	0.423 ± 0.005
XMM–Newton EPN	LW	0691070401	56354.29	3692–3759	7.4	0.421 ± 0.008
XMM–Newton EPN	LW	0720780201	56540.98	3879–3946	18.0	0.429 ± 0.005
XMM–Newton EPN	LW	0720780301	56721.10	4059–4126	19.3	0.429 ± 0.005

Table A6. Log of all *XMM–Newton* observations of SGR 1806−20 following the 2004 December giant flare. We assume that the outburst onset occurred in concomitance with the pinnacle of the giant flare, i.e. on MJD 53366.89613426 (e.g. Palmer et al. 2004). Part of these observations were already analysed by Tiengo et al. (2005), Esposito et al. (2007), Mereghetti, Esposito & Tiengo (2007) and Younes et al. (2015).

Instrument	Mode	Obs. ID	Mid-point of observation (MJD)	Time since outburst onset (d)	Exposure (ks)	Source net count rate (counts s^{-1})
XMM–Newton EPN	SW	0164561301	53436.49	69.59	10.5	1.56 ± 0.01
XMM–Newton EPN	SW	0164561401	53647.62	280.72	22.8	1.101 ± 0.007
XMM–Newton EPN	SW	0406600301	53829.45	462.55	20.5	0.876 ± 0.007
XMM–Newton EPN	SW	0406600401	53988.61	621.71	22.3	0.911 ± 0.007
XMM–Newton EPN	SW	0502170301	54369.82	1002.92	21.3	0.736 ± 0.006
XMM–Newton EPN	SW	0502170401	54558.74	1191.84	22.7	0.600 ± 0.005
XMM–Newton EPN	FF	0554600301	54714.36	1347.46	25.9	0.560 ± 0.005
XMM–Newton EPN	FF	0554600401	54893.89	1526.99	22.6	0.516 ± 0.005
XMM–Newton EPN	FF	0604090201	55081.97	1715.07	23.2	0.474 ± 0.005
XMM–Newton EPN	FF	0654230401	55643.69	2276.79	22.4	0.423 ± 0.004

Table A7. Log of all X-ray observations of CXOU J164710.2−455216 following the 2006 September outburst. The outburst onset occurred on MJD 53999.06587963 (Krimm et al. 2006). Two *Swift* observations (obs. ID: 00030806003 and 00030806004) were carried with the XRT in both the PC and WT modes (indeed, count rates above 1 counts s^{-1} cause an automated shift of the PC to the WT mode, to prevent heavy pile-up). We then considered only the data from the mode which resulted in the largest counting statistics. Part of these observations were already analysed by Israel et al. (2007), Woods et al. (2011), An et al. (2013) and Rodríguez Castillo et al. (2014).

Instrument	Mode	Obs. ID	Mid-point of observation (MJD)	Time since outburst onset (d)	Exposure (ks)	Source net count rate (counts s^{-1})
Swift XRT	PC	00030806001	53999.85	0.78	7.7	0.523 ± 0.008
Swift XRT	WT	00030806002	54000.62	1.55	0.7	0.60 ± 0.03
XMM–Newton EPN	FF	0311792001	54000.70	1.64	26.2	3.80 ± 0.01
Swift XRT	WT	00030806003	54001.07	2.01	4.9	0.49 ± 0.01
Swift XRT	PC	00030806004	54004.41	5.35	2.5	0.30 ± 0.01
Chandra ACIS-S	CC	6724	54005.38	6.31	15.1	1.59 ± 0.01
Chandra ACIS-S	CC	6725	54010.11	11.04	20.1	1.301 ± 0.009
Swift XRT	WT	00030806006	54010.64	11.57	2.0	0.37 ± 0.01
Swift XRT	WT	00030806007	54011.56	12.49	2.0	0.36 ± 0.01
Swift XRT	WT	00030806008	54014.05	14.99	2.1	0.36 ± 0.01
Chandra ACIS-S	CC	6726	54017.42	18.35	25.1	1.221 ± 0.007
Swift XRT	WT	00030806009	54017.85	18.78	3.5	0.286 ± 0.009
Swift XRT	WT	00030806010	54018.05	18.99	2.8	0.33 ± 0.01
Swift XRT	WT	00030806011	54023.38	24.32	5.6	0.303 ± 0.008
Swift XRT	WT	00030806012	54029.24	30.17	5.5	0.276 ± 0.007
Swift XRT	WT	00030806013	54035.76	36.69	2.8	0.29 ± 0.01
Chandra ACIS-S	CC	8455	54036.39	37.32	15.1	0.981 ± 0.008
Swift XRT	WT	00030806014	54119.21	120.15	2.0	0.21 ± 0.01
Swift XRT	WT	00030806015	54122.13	123.06	3.8	0.219 ± 0.008
Chandra ACIS-S	CC	8506	54133.92	134.86	20.1	0.683 ± 0.006
XMM–Newton EPN	LW	0410580601	54148.47	149.41	17.3	1.224 ± 0.009
Swift XRT	WT	00030806016	54207.38	208.32	4.3	0.175 ± 0.007
Swift XRT	WT	00030806017	54208.23	209.16	2.2	0.183 ± 0.009
Swift XRT	PC	00030806018	54235.53	236.46	2.6	0.079 ± 0.006
Swift XRT	PC	00030806019	54237.53	238.47	1.1	0.13 ± 0.01
XMM–Newton EPN	LW	0505290201	54331.59	332.52	28.4	0.714 ± 0.005
XMM–Newton EPN	LW	0555350101	54698.68	699.61	28.4	0.292 ± 0.003
XMM–Newton EPN	LW	0604380101	55067.57	1068.50	38.2	0.163 ± 0.002

Table A8. Log of all X-ray observations of CXOU J164710.2−455216 following the 2011 September outburst. The outburst onset occurred on MJD 55823.88623843 (Baumgartner et al. 2011). Part of these observations were already analysed by An et al. (2013) and Rodríguez Castillo et al. (2014).

Instrument	Mode	Obs. ID	Mid-point of observation (MJD)	Time since outburst onset (d)	Exposure (ks)	Source net count rate (counts s^{-1})
Swift XRT	PC	00030806020	55829.58	5.69	3.1	0.103 ± 0.006
XMM–Newton EPN	LW	0679380501	55832.03	8.14	15.5	0.770 ± 0.007
Swift XRT	PC	00030806022	55835.46	11.57	4.3	0.063 ± 0.004
Swift XRT	PC	00030806023	55839.41	15.52	3.6	0.058 ± 0.004
Swift XRT	PC	00030806024	55840.72	16.83	3.7	0.065 ± 0.004
Swift XRT	PC	00030806025	55842.40	18.51	3.9	0.063 ± 0.004
Swift XRT	PC	00030806026	55844.37	20.48	4.0	0.064 ± 0.004
Swift XRT	PC	00030806027	55849.42	25.53	8.8	0.064 ± 0.003
Chandra ACIS-S	TE	14360	55857.78	33.90	19.1	0.244 ± 0.004

Table A9. Log of all X-ray observations of SGR 0501+4516 following the 2008 August outburst. The outburst onset occurred on MJD 54700.52915509 (Barthelmy et al. 2008). All reported count rates are not corrected for pile-up. One *Chandra* observation was performed with the HRC-I (obs. ID: 9131) and was not included in our analysis. Part of these observations were already analysed by Rea et al. (2009), Göğüş et al. (2010b) and Camero et al. (2014).

Instrument	Mode	Obs. ID	Mid-point of observation (MJD)	Time since outburst onset (d)	Exposure (ks)	Source net count rate (counts s^{-1})
Swift XRT	PC	00321174000	54701.08	0.55	37.1	0.738 ± 0.004
XMM–Newton EPN	SW	0560191501	54701.33	0.80	33.8	8.48 ± 0.02
Swift XRT	PC	00321174001	54701.87	1.34	14.6	0.651 ± 0.007
Chandra ACIS-S	CC	10164	54703.40	2.87	36.5	4.51 ± 0.01
Swift XRT	WT	00321174003	54704.59	4.06	9.0	0.80 ± 0.01
Swift XRT	WT	00321174004	54705.60	4.07	16.3	0.615 ± 0.006
Swift XRT	WT	00321174005	54705.48	4.96	10.6	0.780 ± 0.009
Swift XRT	WT	00321174006	54705.50	4.97	14.5	0.762 ± 0.006
Swift XRT	WT	00321174007	54706.49	5.96	25.0	0.756 ± 0.006
Swift XRT	WT	00321174008	54706.51	5.98	7.9	0.697 ± 0.009
XMM–Newton EPN	SW	0552971101	54707.44	6.91	17.1	7.12 ± 0.02
Swift XRT	WT	00321174009	54708.00	7.47	43.5	0.766 ± 0.004
Swift XRT	WT	00321174010	54708.02	7.49	20.7	0.669 ± 0.006
XMM–Newton EPN	SW	0552971201	54709.57	9.04	7.2	6.68 ± 0.03
Swift XRT	WT	00321174011	54710.55	10.02	67.6	0.728 ± 0.003
Swift XRT	WT	00321174012	54710.52	10.00	32.2	0.556 ± 0.004
XMM–Newton EPN	SW	0552971301	54711.54	11.01	14.3	6.05 ± 0.02
Swift XRT	WT	00321174013	54712.52	11.99	6.1	0.71 ± 0.01
Swift XRT	WT	00321174014	54712.93	12.40	2.0	0.58 ± 0.02
Swift XRT	WT	00321174017	54713.51	12.98	2.8	0.70 ± 0.02
Swift XRT	WT	00321174018	54713.52	12.99	16.7	0.695 ± 0.006
Swift XRT	WT	00321174019	54714.13	13.61	2.1	0.65 ± 0.02
Swift XRT	WT	00321174020	54715.78	15.25	1.3	0.36 ± 0.02
Swift XRT	WT	00321174021	54717.02	16.50	4.6	0.62 ± 0.01
Swift XRT	WT	00321174022	54717.00	16.47	44.0	0.640 ± 0.004
Swift XRT	WT	00321174023	54717.01	16.48	14.7	0.642 ± 0.007
Swift XRT	WT	00321174024	54718.50	17.97	1.8	0.53 ± 0.02
Swift XRT	WT	00321174025	54719.66	19.13	1.1	0.58 ± 0.02
Swift XRT	WT	00321174026	54725.19	24.66	1.0	0.39 ± 0.02
Swift XRT	WT	00321174027	54726.75	26.22	1.0	0.53 ± 0.02
Swift XRT	WT	00321174028	54727.47	26.94	1.7	0.47 ± 0.02
Swift XRT	WT	00321174029	54728.52	27.99	1.6	0.43 ± 0.02
Swift XRT	WT	00321174030	54729.19	28.66	1.3	0.45 ± 0.02
Swift XRT	WT	00321174032	54731.49	30.96	1.7	0.50 ± 0.02
Swift XRT	WT	00321174033	54732.56	32.04	1.1	0.46 ± 0.02
XMM–Newton EPN	LW	0552971401	54739.29	38.76	28.1	3.22 ± 0.01
Swift XRT	WT	00321174036	54741.57	41.04	0.9	0.29 ± 0.02
Swift XRT	WT	00321174037	54745.96	45.43	1.5	0.36 ± 0.02
Swift XRT	WT	00321174038	54748.09	47.57	1.0	0.26 ± 0.02
Swift XRT	WT	00321174039	54752.83	52.30	2.5	0.31 ± 0.01
Swift XRT	WT	00321174040	54755.54	55.01	3.8	0.36 ± 0.01
Swift XRT	WT	00321174041	54758.95	58.42	4.1	0.326 ± 0.009
Swift XRT	WT	00321174042	54762.86	62.34	3.7	0.35 ± 0.01
Swift XRT	WT	00321174043	54766.61	66.09	4.2	0.284 ± 0.008
Swift XRT	WT	00321174044	54775.16	74.63	2.9	0.31 ± 0.01
Swift XRT	WT	00321174045	54781.36	80.84	3.5	0.292 ± 0.009
Swift XRT	WT	00321174046	54789.69	89.16	3.3	0.254 ± 0.009
Swift XRT	WT	00321174047	54798.63	98.11	3.2	0.29 ± 0.01
Swift XRT	WT	00321174048	54803.13	102.60	2.4	0.25 ± 0.01
Swift XRT	WT	00321174049	54810.22	109.70	3.5	0.264 ± 0.009
Swift XRT	WT	00321174050	54818.20	117.68	3.6	0.242 ± 0.008
Swift XRT	WT	00321174051	54825.07	124.55	4.5	0.227 ± 0.007
Swift XRT	WT	00321174053	54838.18	137.65	4.4	0.237 ± 0.007
Swift XRT	WT	00321174054	54846.86	146.33	2.8	0.224 ± 0.009
Swift XRT	WT	00321174055	54852.51	151.98	4.5	0.251 ± 0.008
Swift XRT	WT	00321174056	54859.51	158.98	3.3	0.215 ± 0.008
Swift XRT	WT	00321174057	54866.12	165.60	3.3	0.253 ± 0.009
Swift XRT	WT	00321174058	54900.33	199.80	4.6	0.183 ± 0.006
Swift XRT	WT	00321174059	54910.38	209.85	6.0	0.177 ± 0.005

Table A9 – *continued*

Instrument	Mode	Obs. ID	Mid-point of observation (MJD)	Time since outburst onset (d)	Exposure (ks)	Source net count rate (counts s^{-1})
Swift XRT	WT	00321174060	54926.39	225.87	3.9	0.177 ± 0.007
Swift XRT	WT	00321174061	54940.56	240.04	5.2	0.126 ± 0.005
XMM–Newton EPN	SW	0604220101	55073.93	373.40	24.6	0.224 ± 0.003
Swift XRT	PC	00321174062	55111.81	411.29	3.3	0.074 ± 0.005
Swift XRT	PC	00321174063	55114.81	414.29	3.9	0.077 ± 0.004
Swift XRT	PC	00321174064	55115.29	414.76	6.0	0.100 ± 0.004
Swift XRT	PC	00321174065	55172.27	471.75	13.4	0.072 ± 0.002
Swift XRT	PC	00321174066	55245.45	544.92	2.3	0.073 ± 0.006
Swift XRT	PC	00321174067	55246.89	546.36	4.4	0.069 ± 0.004
Swift XRT	PC	00321174068	55248.62	548.10	5.0	0.065 ± 0.004

Table A10. Log of all X-ray observations of 1E 1547−5408 following the 2008 October outburst. The outburst onset occurred on MJD 54742.39453704 (Krimm et al. 2008). All reported count rates are not corrected for pile-up. Part of these observations were already analysed by Israel et al. (2010), Ng et al. (2011), Dib et al. (2012) and Kuiper et al. (2012).

Instrument	Mode	Obs. ID	Mid-point of observation (MJD)	Time since outburst onset (d)	Exposure (ks)	Source net count rate (counts s^{-1})
Swift XRT	PC	00330353000	54742.46	0.07	4.1	0.60 ± 0.01
Swift XRT	WT	00330353001	54742.80	0.40	14.2	0.539 ± 0.006
Swift XRT	WT	00330353002	54743.79	1.40	4.8	0.45 ± 0.01
Swift XRT	WT	00330353004	54745.14	2.75	10.5	0.389 ± 0.006
Swift XRT	WT	00330353005	54746.51	4.12	7.7	0.407 ± 0.007
Chandra ACIS-S	CC	8811	54746.60	4.21	12.1	1.39 ± 0.01
Swift XRT	WT	00330353006	54747.11	4.72	4.5	0.380 ± 0.009
Swift XRT	WT	00330353007	54748.39	6.00	3.7	0.314 ± 0.009
Swift XRT	WT	00330353008	54749.46	7.07	3.9	0.328 ± 0.009
Chandra ACIS-S	CC	8812	54749.50	7.11	15.1	1.209 ± 0.009
Swift XRT	WT	00330353010	54751.53	9.14	3.7	0.309 ± 0.009
Swift XRT	WT	00330353011	54752.40	10.01	3.4	0.31 ± 0.01
Swift XRT	WT	00330353012	54755.14	12.75	4.0	0.303 ± 0.009
Swift XRT	WT	00330353013	54757.38	14.99	5.0	0.352 ± 0.008
Chandra ACIS-S	CC	8813	54757.60	15.21	10.1	1.20 ± 0.01
Swift XRT	WT	00330353014	54759.80	17.41	3.9	0.322 ± 0.009
Chandra ACIS-S	CC	10792	54760.80	18.41	10.1	1.11 ± 0.01
Swift XRT	WT	00330353015	54761.43	19.04	3.9	0.35 ± 0.01
Swift XRT	WT	00330353016	54763.21	20.82	3.6	0.34 ± 0.01
Chandra ACIS-S	CC	8814	54765.10	22.71	23.1	1.032 ± 0.007

Table A11. Log of all X-ray observations of 1E 1547−5408 following the 2009 January outburst. The outburst onset occurred on MJD 54853.03740937 (Connaughton & Briggs 2009). All reported count rates are not corrected for pile-up. We did not include the following *Swift* observations: obs. ID 0003095041, because the source PSF falls on a column of bad pixels in this case; obs. ID 00030956050, 00090404025 and 00091032011, owing to the low number of net source counts (about 80 counts in the former two cases and 40 counts in the latter case). Part of these observations were already analysed by Bernardini et al. (2011b), Ng et al. (2011), Scholz & Kaspi (2011), Dib et al. (2012) and Kuiper et al. (2012).

Instrument	Mode	Obs. ID	Mid-point of observation (MJD)	Time since outburst onset (d)	Exposure (ks)	Source net count rate (counts s^{-1})
Swift XRT	PC	00340923000	54854.65	1.61	1.7	0.99 ± 0.02
Chandra/HETG	CC	10185	54855.04	2.00	10.1	1.04 ± 0.01
Swift XRT	WT	00090007026	54855.05	2.01	8.2	1.18 ± 0.01
Swift XRT	PC	00340986000	54855.21	2.17	2.9	0.77 ± 0.02
Swift XRT	PC	00030956031	54855.32	2.28	2.5	0.69 ± 0.02
Swift XRT	WT	00090007027	54856.19	3.15	3.3	1.10 ± 0.02
Swift XRT	PC	00341055000	54856.20	3.16	4.0	0.68 ± 0.01
Chandra ACIS-S	CC	10186	54856.73	3.70	12.1	3.33 ± 0.02
Swift XRT	PC	00341114000	54856.96	3.92	4.6	0.64 ± 0.01
Swift XRT	WT	00090007028	54857.25	4.21	3.5	0.99 ± 0.02
Swift XRT	PC	00030956032	54858.20	5.16	6.2	0.67 ± 0.01
Swift XRT	WT	00090007029	54858.43	5.39	1.8	0.86 ± 0.02
Swift XRT	PC	00030956033	54859.59	6.55	5.0	0.57 ± 0.01
Swift XRT	WT	00090007030	54859.91	6.87	1.9	0.55 ± 0.02
Swift XRT	PC	00030956034	54860.18	7.14	5.9	0.63 ± 0.01
Swift XRT	WT	00090007031	54860.78	7.74	2.1	0.83 ± 0.02
Chandra ACIS-S	CC	10187	54860.84	7.80	13.1	2.69 ± 0.01
Swift XRT	WT	00090007032	54861.69	8.65	2.9	0.74 ± 0.02
Swift XRT	WT	00030956035	54861.72	8.68	3.0	0.80 ± 0.02
Swift XRT	WT	00030956036	54862.18	9.14	3.0	0.72 ± 0.02
Swift XRT	WT	00090007033	54862.83	9.79	2.5	0.79 ± 0.02
Swift XRT	WT	00030956037	54863.61	10.57	2.0	0.68 ± 0.02
Swift XRT	WT	00090007034	54863.76	10.72	2.0	0.76 ± 0.02
Swift XRT	PC	00030956038	54865.66	12.62	5.9	0.474 ± 0.009
Swift XRT	PC	00341965000	54865.84	12.80	0.9	0.68 ± 0.03
XMM–Newton EPN	FF	0560181101	54866.09	13.06	48.9	4.99 ± 0.01
Swift XRT	PC	00030956039	54866.84	13.80	6.1	0.56 ± 0.01
Swift XRT	WT	00030956040	54867.57	14.53	6.1	0.60 ± 0.01
Chandra ACIS-S	CC	10188	54868.68	15.64	14.3	2.35 ± 0.01
Swift XRT	WT	00030956042	54869.59	16.55	1.6	0.68 ± 0.02
Swift XRT	WT	00090007036	54874.32	21.28	4.6	0.47 ± 0.01
Swift XRT	WT	00090007037	54884.63	31.59	4.6	0.55 ± 0.01
Swift XRT	WT	00090007038	54894.61	41.57	3.9	0.45 ± 0.01
Swift XRT	WT	00090007039	54904.45	51.41	4.0	0.46 ± 0.01
Swift XRT	WT	00090007040	54914.90	61.86	4.2	0.288 ± 0.008
Swift XRT	WT	00030956043	54950.47	97.43	1.7	0.44 ± 0.02
Swift XRT	WT	00030956044	54964.32	111.28	1.8	0.43 ± 0.02
Swift XRT	WT	00030956045	54978.52	125.48	2.2	0.36 ± 0.01
Swift XRT	PC	00030956047	55006.88	153.84	1.8	0.29 ± 0.01
Swift XRT	PC	00030956048	55020.80	167.76	2.5	0.29 ± 0.01
Swift XRT	PC	00030956049	55034.12	181.08	1.7	0.33 ± 0.01
Swift XRT	PC	00030956051	55062.11	209.07	2.4	0.30 ± 0.01
Swift XRT	WT	00030956053	55090.52	237.48	1.5	0.32 ± 0.01
Swift XRT	WT	00030956054	55104.63	251.59	3.3	0.35 ± 0.01
Swift XRT	WT	00030956055	55118.09	265.05	2.0	0.25 ± 0.01
Swift XRT	WT	00030956056	55200.35	347.31	1.9	0.28 ± 0.01
Swift XRT	WT	00030956057	55214.10	361.06	2.0	0.25 ± 0.01
Swift XRT	WT	00030956058	55228.87	375.83	2.0	0.26 ± 0.01
XMM–Newton EPN	LW	0604880101	55237.44	384.41	39.4	1.819 ± 0.007
Swift XRT	WT	00030956059	55256.06	403.02	2.0	0.25 ± 0.01
Swift XRT	WT	00030956060	55270.86	417.82	1.9	0.23 ± 0.01
Swift XRT	WT	00030956061	55284.96	431.92	2.0	0.28 ± 0.01
Swift XRT	PC	00090404001	55287.82	434.78	0.9	0.14 ± 0.01
Swift XRT	PC	00090404002	55291.37	438.33	3.6	0.180 ± 0.007
Swift XRT	PC	00090404003	55298.72	445.68	5.7	0.156 ± 0.005
Swift XRT	PC	00090404004	55307.90	454.86	3.5	0.195 ± 0.008
Swift XRT	PC	00090404005	55317.22	464.18	2.3	0.166 ± 0.009
Swift XRT	PC	00090404006	55327.63	474.59	3.0	0.171 ± 0.008
Swift XRT	PC	00090404007	55337.91	484.87	3.0	0.188 ± 0.008

Table A11 – *continued*

Instrument	Mode	Obs. ID	Mid-point of observation (MJD)	Time since outburst onset (d)	Exposure (ks)	Source net count rate (counts s^{-1})
Swift XRT	PC	00090404008	55347.50	494.46	2.9	0.187 ± 0.008
Swift XRT	WT	00030956062	55357.31	504.27	2.8	0.25 ± 0.01
Swift XRT	PC	00090404010	55377.39	524.35	2.8	0.181 ± 0.008
Swift XRT	PC	00090404011	55387.59	534.55	3.3	0.148 ± 0.007
Swift XRT	PC	00090404012	55398.77	545.73	3.2	0.167 ± 0.007
Swift XRT	PC	00090404013	55407.22	554.18	3.6	0.162 ± 0.007
Swift XRT	PC	00090404014	55417.41	564.37	3.0	0.193 ± 0.008
Swift XRT	PC	00090404015	55427.38	574.34	2.9	0.189 ± 0.008
Swift XRT	PC	00090404016	55436.25	583.21	3.6	0.171 ± 0.007
Swift XRT	PC	00090404017	55447.08	594.04	3.0	0.144 ± 0.007
Swift XRT	PC	00090404018	55457.53	604.49	3.1	0.180 ± 0.008
Swift XRT	PC	00090404019	55467.09	614.05	3.5	0.191 ± 0.007
Swift XRT	PC	00090404020	55477.26	624.22	3.5	0.159 ± 0.007
Swift XRT	PC	00090404021	55487.14	634.10	3.1	0.172 ± 0.007
Swift XRT	PC	00090404022	55493.86	640.82	2.8	0.186 ± 0.008
Swift XRT	PC	00090404023	55567.69	714.65	3.2	0.154 ± 0.007
Swift XRT	PC	00090404024	55578.14	725.10	3.0	0.179 ± 0.008
Swift XRT	PC	00090404026	55607.45	754.41	2.8	0.107 ± 0.006
Swift XRT	PC	00090404027	55617.27	764.23	3.2	0.134 ± 0.007
Swift XRT	PC	00090404028	55627.91	774.88	3.3	0.175 ± 0.007
Swift XRT	PC	00090404029	55637.86	784.82	2.3	0.148 ± 0.008
Swift XRT	PC	00090404030	55647.43	794.39	2.9	0.153 ± 0.007
Swift XRT	PC	00091032001	55656.33	803.29	2.5	0.128 ± 0.007
Swift XRT	PC	00091032002	55666.55	813.51	3.1	0.135 ± 0.007
Swift XRT	PC	00091032003	55676.45	823.41	3.3	0.141 ± 0.007
Swift XRT	PC	00091032004	55687.09	834.05	2.7	0.132 ± 0.007
Swift XRT	PC	00091032005	55696.83	843.79	3.2	0.148 ± 0.007
Swift XRT	PC	00091032006	55706.57	853.54	2.7	0.151 ± 0.008
Swift XRT	PC	00091032007	55716.46	863.42	2.8	0.138 ± 0.007
Swift XRT	PC	00091032008	55726.62	873.59	3.0	0.093 ± 0.006
Swift XRT	PC	00091032009	55736.73	883.69	2.3	0.156 ± 0.008
Swift XRT	PC	00091032011	55749.45	896.41	1.4	0.16 ± 0.01
Swift XRT	PC	00091032012	55756.27	903.23	3.0	0.154 ± 0.007
Swift XRT	PC	00091032013	55766.60	913.56	2.9	0.161 ± 0.008
Swift XRT	PC	00091032015	55780.15	927.11	1.5	0.14 ± 0.01
Swift XRT	PC	00091032016	55786.43	933.39	1.7	0.146 ± 0.009
Swift XRT	PC	00091032017	55790.71	937.68	3.3	0.164 ± 0.007
Swift XRT	PC	00091032018	55796.84	943.80	2.6	0.157 ± 0.008
Swift XRT	PC	00091032019	55806.41	953.37	2.9	0.150 ± 0.007
Swift XRT	PC	00091032020	55816.45	963.41	3.2	0.153 ± 0.007
Swift XRT	WT	00091032021	55826.23	973.20	2.6	0.25 ± 0.01
Swift XRT	WT	00091032022	55836.27	983.23	3.1	0.214 ± 0.008
Swift XRT	PC	00091032023	55846.88	993.84	3.0	0.146 ± 0.007
Swift XRT	PC	00091032024	55856.40	1003.36	2.7	0.129 ± 0.007

Table A12. Log of all X-ray observations of SGR 0418+5729 following the 2009 June outburst. The outburst onset occurred on MJD 54987.86167685 (van der Horst et al. 2009). Part of these observations were already analysed by Esposito et al. (2010a) and Rea et al. (2010, 2013a).

Instrument	Mode	Obs. ID	Mid-point of observation (MJD)	Time since outburst onset (d)	Exposure (ks)	Source net count rate (counts s^{-1})
Swift XRT	PC	00031422001	55020.91	33.05	2.9	0.241 ± 0.009
Swift XRT	PC	00031422002	55021.41	33.54	10.6	0.249 ± 0.005
Swift XRT	PC	00031422003	55022.15	34.29	5.6	0.188 ± 0.006
Swift XRT	WT	00031422004	55024.32	36.46	7.1	0.286 ± 0.006
Swift XRT	WT	00031422006	55027.81	39.95	7.7	0.321 ± 0.007
Swift XRT	WT	00031422007	55028.51	40.65	16.4	0.276 ± 0.004
XMM–Newton EPN	SW	0610000601	55056.26	68.40	45.0	1.480 ± 0.006
Swift XRT	PC	00031422008	55095.42	107.56	9.4	0.067 ± 0.003
Swift XRT	PC	00031422009	55096.50	108.64	7.6	0.077 ± 0.003
Swift XRT	PC	00031422010	55143.49	155.63	15.1	0.046 ± 0.002
Swift XRT	PC	00031422011[a1]	55210.51	222.64	3.6	0.020 ± 0.002
Swift XRT	PC	00031422012[a1]	55211.66	223.79	3.6	0.015 ± 0.002
Swift XRT	PC	00031422013[a1]	55212.45	224.59	4.0	0.021 ± 0.002
Swift XRT	PC	00031422014[a1]	55213.36	225.50	3.7	0.024 ± 0.003
Swift XRT	PC	00031422015[a2]	55241.84	253.97	4.5	0.020 ± 0.002
Swift XRT	PC	00031422016[a2]	55242.84	254.97	4.5	0.017 ± 0.002
Swift XRT	PC	00031422017[a2]	55243.30	255.44	4.5	0.017 ± 0.002
Swift XRT	PC	00031422018[a2]	55244.68	256.82	4.6	0.016 ± 0.002
Swift XRT	PC	00031422019[a2]	55245.81	257.95	3.4	0.018 ± 0.002
Swift XRT	PC	00031422020[a2]	55246.25	258.39	3.2	0.017 ± 0.002
Swift XRT	PC	00031422021[a3]	55386.63	398.77	3.6	0.005 ± 0.001
Swift XRT	PC	00031422022[a3]	55387.87	400.00	5.1	0.0023 ± 0.0007
Swift XRT	PC	00031422023[a3]	55388.30	400.44	5.0	0.0026 ± 0.0008
Swift XRT	PC	00031422024[a3]	55389.07	401.21	5.4	0.0032 ± 0.0008
Swift XRT	PC	00031422025[a3]	55390.14	402.28	4.8	0.0014 ± 0.0007
Chandra ACIS-S	TE	12312	55400.81	412.95	27.2	0.0170 ± 0.0008
XMM–Newton EPN	FF	0605852201	55463.31	475.45	8.6	0.040 ± 0.002
Chandra ACIS-S	TE	13148	55529.43	541.57	27.2	0.0045 ± 0.0004
XMM–Newton EPN	LW	0672670201	55630.34	642.48	11.6	0.007 ± 0.001
Chandra ACIS-S	TE	13235	55762.56	774.70	69.8	0.0034 ± 0.0002
XMM–Newton EPN	LW	0672670401[a4]	55813.84	825.98	25.9	0.0062 ± 0.0006
XMM–Newton EPN	LW	0672670501[a4]	55816.19	828.33	28.7	0.0070 ± 0.0006
Chandra ACIS-S	TE	13236	55891.94	904.08	68.0	0.0029 ± 0.0002
XMM–Newton EPN	LW	0693100101	56165.04	1177.18	54.3	0.0060 ± 0.0004
XMM–Newton EPN	LW	0723810101[a5]	56520.00	1532.14	32.7	0.0045 ± 0.0005
XMM–Newton EPN	LW	0723810201[a5]	56522.19	1534.33	35.3	0.0053 ± 0.0005
XMM–Newton EPN	LW	0741970201[a6]	56883.20	1895.34	36.0	0.0046 ± 0.0004
XMM–Newton EPN	LW	0741970301[a6]	56885.20	1897.33	41.2	0.0044 ± 0.0004
XMM–Newton EPN	LW	0741970401[a6]	56887.20	1899.34	30.9	0.0038 ± 0.0004

Note. [a]The spectral files and responses of these observations were combined to improve the fit statistics.

Table A13. Log of all X-ray observations of SGR 1833−0832 following the 2010 March outburst. The outburst onset occurred on MJD 55274.77418981 (Gelbord et al. 2010). Part of these observations were already analysed by Göğüş et al. (2010a) and Esposito et al. (2011).

Instrument	Mode	Obs. ID	Mid-point of observation (MJD)	Time since outburst onset (d)	Exposure (ks)	Source net count rate (counts s^{-1})
Swift XRT	PC	00416485000	55275.21	0.44	29.0	0.031 ± 0.001
Swift XRT	PC	00416485001	55276.41	1.64	10.7	0.036 ± 0.002
Swift XRT	WT	00416485002	55276.90	2.13	9.9	0.121 ± 0.004
Swift XRT	PC	00416485003	55277.60	2.82	13.3	0.038 ± 0.002
Chandra ACIS-I	TE	11114	55278.27	3.49	33.1	0.100 ± 0.002
XMM–Newton EPN	FF	0605851901	55278.67	3.90	18.5	0.320 ± 0.004
Swift XRT	PC	00416485004	55278.68	3.91	12.8	0.032 ± 0.002
Swift XRT	PC	00416485005	55279.52	4.75	10.3	0.034 ± 0.002
Swift XRT	PC	00416485006	55280.53	5.76	9.9	0.036 ± 0.002
Swift XRT	PC	00416485007	55281.73	6.96	10.0	0.032 ± 0.002
Swift XRT	PC	00416485008	55282.66	7.89	9.8	0.036 ± 0.002
Swift XRT	PC	00416485009	55283.38	8.60	10.9	0.034 ± 0.002
Swift XRT	PC	00416485010	55284.71	9.93	9.5	0.032 ± 0.002
Swift XRT	PC	00416485011	55286.49	11.72	7.9	0.030 ± 0.002
XMM–Newton EPN	FF	0605852001	55288.63	13.86	18.2	0.317 ± 0.005
Swift XRT	PC	00416485012	55289.80	15.03	10.0	0.026 ± 0.002
Swift XRT	PC	00416485013	55293.75	18.98	10.1	0.031 ± 0.002
Swift XRT	PC	00416485014	55298.67	23.90	5.1	0.026 ± 0.002
Swift XRT	PC	50041648015	55299.24	24.46	4.0	0.029 ± 0.003
XMM–Newton EPN	FF	0605852101	55299.30	24.53	14.6	0.266 ± 0.004
Swift XRT	PC	00416485016	55301.24	26.46	9.4	0.026 ± 0.002
Swift XRT	PC	00416485017	55304.96	30.19	8.8	0.025 ± 0.002
Swift XRT	PC	00416485018	55307.36	32.59	10.3	0.025 ± 0.002
Swift XRT	PC	00416485019	55310.05	35.28	7.6	0.027 ± 0.002
Swift XRT	PC	00416485020	55315.82	41.05	5.5	0.026 ± 0.002
Swift XRT	PC	00416485021	55316.16	41.39	4.4	0.030 ± 0.003
Swift XRT	PC	00416485022	55340.39	65.62	18.0	0.019 ± 0.001
Swift XRT	PC	00416485023[a]	55432.30	157.52	5.3	0.012 ± 0.002
Swift XRT	PC	00416485024[a]	55433.67	158.90	2.2	0.009 ± 0.002
Swift XRT	PC	00416485025[a]	55434.51	159.73	9.9	0.010 ± 0.001
Swift XRT	PC	00416485026[a]	55435.28	160.51	2.5	0.011 ± 0.002

Note. [a]The spectral files and responses of these observations were combined to improve the fit statistics.

Table A14. Log of all X-ray observations of Swift J1822.3−1606 following the 2011 July outburst. The outburst onset occurred on MJD 55756.53318403 (Cummings et al. 2011). We did not include the following *Swift* observations: obs. ID 00032033038, because the source was located at the edge of the detector and only a few counts were collected from the source; obs. ID 00032033041, because the source PSF falls on a column of bad pixels. Moreover, one *Chandra* observation was performed with the HRC-I (obs. ID: 13511), with no sufficient spectral information, and thus was not included in our analysis as well. Part of these observations were already analysed by Livingstone et al. (2011b), Rea et al. (2012a), Scholz et al. (2012), Scholz, Kaspi & Cumming (2014b) and Rodríguez Castillo et al. (2016).

Instrument	Mode	Obs. ID	Mid-point of observation (MJD)	Time since outburst onset (d)	Exposure (ks)	Source net count rate (counts s^{-1})
Swift XRT	PC	00032033001	55757.75	1.22	1.6	2.18 ± 0.04
Swift XRT	WT	00032033002	55758.68	2.15	2.0	5.16 ± 0.05
Swift XRT	WT	00032033003	55759.69	3.16	2.0	4.29 ± 0.05
Swift XRT	WT	00032033005	55761.54	5.01	0.5	3.98 ± 0.09
Swift XRT	WT	00032033006	55762.24	5.71	1.8	3.78 ± 0.05
Swift XRT	WT	00032033007	55763.30	6.77	1.6	3.46 ± 0.05
Swift XRT	WT	00032033008	55765.85	9.32	2.2	2.10 ± 0.03
Swift XRT	WT	00032033009	55766.28	9.75	1.7	2.98 ± 0.04
Chandra ACIS-S	CC	12612	55769.28	12.75	15.0	11.64 ± 0.03
Swift XRT	WT	00032033010	55769.50	12.97	2.1	2.54 ± 0.03
Swift XRT	WT	00032033011	55770.40	13.87	2.1	2.44 ± 0.03
Swift XRT	WT	00032033012	55771.23	14.70	2.1	2.38 ± 0.03
Swift XRT	WT	00032033013	55772.40	15.87	2.1	2.13 ± 0.03
Chandra ACIS-S	CC	12613	55777.22	20.68	13.6	7.45 ± 0.02
Swift XRT	WT	00032051001	55778.11	21.58	1.7	1.74 ± 0.03

Table A14 – *continued*

Instrument	Mode	Obs. ID	Mid-point of observation (MJD)	Time since outburst onset (d)	Exposure (ks)	Source net count rate (counts s^{-1})
Swift XRT	WT	00032051002	55779.19	22.66	1.7	1.66 ± 0.03
Swift XRT	WT	00032051003	55780.50	23.97	2.3	1.59 ± 0.03
Swift XRT	WT	00032051004	55781.50	24.97	2.3	1.57 ± 0.03
Swift XRT	WT	00032051005	55786.42	29.89	2.2	1.28 ± 0.02
Swift XRT	WT	00032051006	55787.59	31.06	2.2	1.29 ± 0.02
Swift XRT	WT	00032051007	55788.26	31.73	2.3	1.25 ± 0.02
Swift XRT	WT	00032051008	55789.66	33.13	2.2	1.17 ± 0.02
Swift XRT	WT	00032051009	55790.36	33.83	2.2	1.07 ± 0.02
Swift XRT	WT	00032033015	55800.86	44.33	2.9	0.85 ± 0.02
Swift XRT	WT	00032033016	55807.49	50.96	2.4	0.77 ± 0.02
Chandra ACIS-S	CC	12614	55822.80	66.26	10.0	2.68 ± 0.02
Swift XRT	PC	00032033017	55822.83	66.30	4.9	0.45 ± 0.01
Swift XRT	WT	00032033018	55824.71	68.18	1.5	0.60 ± 0.02
XMM–Newton EPN	LW	0672281801	55827.25	70.72	9.9	5.03 ± 0.02
Swift XRT	WT	00032033019	55829.45	72.92	2.3	0.61 ± 0.02
Swift XRT	WT	00032033020	55835.54	79.01	2.6	0.53 ± 0.01
Swift XRT	WT	00032033021	55842.06	85.53	4.2	0.44 ± 0.01
XMM–Newton EPN	LW	0672282701	55847.02	90.49	24.0	3.71 ± 0.01
Swift XRT	WT	00032033022	55849.62	93.09	3.4	0.40 ± 0.01
Swift XRT	WT	00032033023	55856.58	100.05	2.2	0.37 ± 0.01
Swift XRT	PC	00032033024	55862.59	106.06	10.2	0.263 ± 0.005
Chandra ACIS-S	CC	12615	55867.18	110.65	16.2	1.47 ± 0.01
Swift XRT	PC	00032033025	55977.17	220.64	6.2	0.152 ± 0.005
Swift XRT	WT	00032033026	55978.53	222.00	10.2	0.198 ± 0.005
Swift XRT	PC	00032033027	55981.99	225.46	11.0	0.137 ± 0.004
Swift XRT	WT	00032033028	55982.96	226.43	6.6	0.194 ± 0.006
Swift XRT	WT	00032033029	55985.18	228.65	7.0	0.201 ± 0.006
Swift XRT	WT	00032033030	55985.55	229.02	7.0	0.195 ± 0.006
Swift XRT	WT	00032033031	55991.09	234.56	6.8	0.193 ± 0.006
XMM–Newton EPN	LW	0672282901	56023.12	266.59	23.0	1.421 ± 0.008
Swift XRT	WT	00032033032	56031.14	274.61	4.2	0.236 ± 0.008
Chandra ACIS-S	CC	14330	56037.09	280.56	20.0	0.663 ± 0.006
Swift XRT	WT	00032033033	56052.66	296.13	5.1	0.242 ± 0.007
Swift XRT	WT	00032033034	56073.25	316.72	4.9	0.200 ± 0.007
Swift XRT	WT	00032033035	56095.59	339.67	5.6	0.179 ± 0.006
Swift XRT	WT	00032033036	56104.55	348.02	6.2	0.167 ± 0.005
Swift XRT	WT	00032033037	56114.30	357.77	6.8	0.146 ± 0.005
Swift XRT	WT	00032033039	56156.20	399.67	4.9	0.205 ± 0.007
Swift XRT	WT	00032033040	56161.70	405.17	5.0	0.214 ± 0.007
XMM–Newton EPN	LW	0672283001	56178.85	422.32	20.2	0.950 ± 0.007
Swift XRT	WT	00032033042	56206.01	449.48	5.0	0.147 ± 0.006
Swift XRT	WT	00032033043	56238.71	482.18	4.9	0.117 ± 0.005
Swift XRT	WT	00032051010	56334.76	578.23	9.5	0.114 ± 0.004
Swift XRT	WT	00032051011	56355.40	598.87	8.2	0.142 ± 0.004
Swift XRT	WT	00032051012	56386.91	630.38	2.7	0.157 ± 0.008
Swift XRT	WT	00032051013	56387.28	630.75	7.7	0.180 ± 0.005
Swift XRT	WT	00032051014	56409.09	652.55	8.4	0.105 ± 0.004
Swift XRT	WT	00032051016	56456.35	699.82	8.8	0.141 ± 0.004
Swift XRT	WT	00032051017	56459.66	703.13	7.1	0.104 ± 0.004
Swift XRT	WT	00032051018	56490.67	734.14	4.0	0.142 ± 0.006
Swift XRT	WT	00032051019	56491.52	734.98	18.0	0.165 ± 0.003
Swift XRT	WT	00032051020	56536.11	779.58	13.8	0.132 ± 0.003
Swift XRT	WT	00032051021	56598.52	841.99	6.3	0.119 ± 0.005
Swift XRT	WT	00032051022	56599.99	843.46	9.1	0.128 ± 0.004
XMM–Newton EPN	FF	0722520101	56724.58	968.05	40.3	0.139 ± 0.002

Table A15. Log of all X-ray observations of Swift J1834.9−0846 following the 2011 August outburst. The outburst onset occurred on MJD 55780.83178241 (D'Elia et al. 2011). We did not include two *Swift* XRT WT-mode observations carried out within 6 h since the outburst onset (obs. ID: 00458907001, 00458907002) because they lasted only 91 and 141 s, respectively, and provided a low number of counts for a meaningful spectral analysis. Part of these observations were already analysed by Kargaltsev et al. (2012) and Esposito et al. (2013).

Instrument	Mode	Obs. ID	Mid-point of observation (MJD)	Time since outburst onset (d)	Exposure (ks)	Source net count rate (counts s^{-1})
Swift XRT	PC	00458907000	55780.87	0.04	1.5	0.14 ± 0.01
Swift XRT	WT	00458907003	55781.62	0.79	1.7	0.05 ± 0.006
Swift XRT	WT	00458907004	55781.84	1.00	1.0	0.051 ± 0.008
Swift XRT	WT	00458907006	55782.10	1.27	2.7	0.053 ± 0.005
Swift XRT	WT	00458907007	55785.34	4.51	5.7	0.046 ± 0.003
Swift XRT	WT	00458907008	55787.28	6.45	5.4	0.033 ± 0.003
Swift XRT	WT	00458907009	55791.46	10.63	8.0	0.041 ± 0.002
Swift XRT	WT	00458907010	55794.43	13.60	2.5	0.038 ± 0.004
Chandra ACIS-S	TE	14329	55795.74	14.91	13.0	0.071 ± 0.002
Swift XRT	WT	00458907011	55797.81	16.98	0.9	0.033 ± 0.006
Swift XRT	WT	00458907012	55800.35	19.52	1.9	0.029 ± 0.004
Swift XRT	PC	00501752000	55803.06	22.23	2.6	0.010 ± 0.002
Swift XRT	WT	00458907013	55803.38	22.54	2.2	0.029 ± 0.004
Swift XRT	PC	00458907014	55806.47	25.64	2.1	0.016 ± 0.003
Chandra ACIS-S	TE	14055	55809.59	28.76	16.3	0.056 ± 0.002
Swift XRT	PC	00458907016	55814.45	33.61	2.0	0.007 ± 0.002
Swift XRT	WT	00032097001	55819.28	38.45	9.1	0.025 ± 0.002
XMM–Newton EPN	FF	0679380201	55821.80	40.96	23.7	0.116 ± 0.002
Swift XRT	WT	00032097002	55822.27	41.43	10.4	0.035 ± 0.002
Swift XRT	WT	00032097003	55825.60	44.77	7.7	0.033 ± 0.002
Swift XRT	WT	00032097004	55828.52	47.69	8.1	0.028 ± 0.002
Chandra ACIS-S	TE	14056	55836.71	55.88	24.5	0.023 ± 0.001
Chandra ACIS-S	TE	14057	55877.60	96.77	37.6	0.0014 ± 0.0002
XMM–Newton EPN	FF	0723270101	56733.38	952.54	58.0	0.0052 ± 0.0005
XMM–Newton EPN	FF	0743020201	56 946.78	1165.95	50.3	$< 0.003^{a}$

Note. [a]The upper limit is quoted at the 3σ c.l., and is derived by applying the EUPPER task of SAS. The corresponding upper limits on the fluxes and luminosities were estimated by assuming an absorbed blackbody spectral model with the same parameters as those of the spectrum of the penultimate *XMM–Newton* observation (obs. ID: 0723270101).

Table A16. Log of the X-ray observations of 1E 1048.1−5937 following the 2011 December outburst. No burst signalling the outburst onset was detected in this case. The outburst onset is thus considered to be occurred on MJD 55926, when an increase in the X-ray flux was measured (the previous *Swift* observation was carried out on MJD 55877.20). Part of these observations were already analysed by Archibald et al. (2015). We focus here on the observations covering the first ∼1000 d of the outburst. We did not include the *Swift* observation 00031220126, because the source PSF falls on a column of bad pixels in this case.

Instrument	Mode	Obs. ID	Mid-point of observation (MJD)	Time since outburst onset (d)	Exposure (ks)	Source net count rate (counts s^{-1})
Swift XRT	WT	00031220066	55926.27	0.27	2.0	0.96 ± 0.02
Swift XRT	WT	00031220067	55927.04	1.04	2.0	0.91 ± 0.02
Swift XRT	WT	00031220068	55936.07	10.07	2.2	0.88 ± 0.02
Swift XRT	WT	00031220069	55936.32	10.32	1.1	0.85 ± 0.03
Swift XRT	WT	00031220070	55937.04	11.04	1.3	0.66 ± 0.02
Swift XRT	WT	00031220071	55946.19	20.19	3.2	0.74 ± 0.02
Swift XRT	WT	00031220073	55947.12	21.12	2.2	0.64 ± 0.02
Swift XRT	WT	00031220074	55956.05	30.05	2.0	0.72 ± 0.02
Swift XRT	WT	00031220077	55962.84	36.84	6.3	0.72 ± 0.01
Swift XRT	WT	00031220078	55966.09	40.09	2.3	0.74 ± 0.02
Swift XRT	WT	00031220081	55969.86	43.86	7.4	0.73 ± 0.01
Swift XRT	WT	00031220085	55977.14	51.14	1.9	0.46 ± 0.02
Chandra ACIS-S	CC	14139	55980.95	54.95	6.1	3.09 ± 0.02
Swift XRT	WT	00031220086	55981.75	55.75	5.0	0.73 ± 0.01
Swift XRT	WT	00031220090	55998.15	72.15	1.8	0.58 ± 0.02
Swift XRT	WT	00031220095	56016.12	90.12	1.9	0.43 ± 0.02
Swift XRT	WT	00031220098	56027.44	101.44	2.0	0.61 ± 0.02
Chandra ACIS-S	CC	14140	56027.56	101.56	12.0	2.68 ± 0.02
Swift XRT	WT	00031220099	56040.21	114.21	1.3	0.60 ± 0.02
Swift XRT	WT	00031220102	56054.10	128.10	2.2	0.59 ± 0.02
Swift XRT	WT	00031220105	56068.25	142.25	0.6	0.60 ± 0.03
Swift XRT	WT	00031220110	56083.25	157.25	1.9	0.59 ± 0.02
Swift XRT	WT	00031220113	56097.24	171.24	1.6	0.55 ± 0.02
Swift XRT	WT	00031220116	56111.24	185.24	2.1	0.51 ± 0.02
Swift XRT	WT	00031220133	56160.05	234.05	1.6	0.53 ± 0.02
Swift XRT	WT	00031220147	56196.04	270.04	1.6	0.39 ± 0.02
Swift XRT	WT	00031220148	56202.05	276.05	1.5	0.41 ± 0.02
Swift XRT	WT	00031220158	56223.27	297.27	1.5	0.44 ± 0.02
Swift XRT	WT	00031220167	56244.28	318.28	1.8	0.47 ± 0.02
Swift XRT	WT	00031220177	56266.34	340.34	1.5	0.39 ± 0.02
Swift XRT	WT	00031220181	56280.31	354.31	1.5	0.39 ± 0.02
Swift XRT	WT	00031220189	56300.28	374.28	1.3	0.37 ± 0.02
Swift XRT	WT	00031220192	56307.12	381.12	1.2	0.37 ± 0.02
Swift XRT	WT	00031220201	56327.30	401.30	1.2	0.46 ± 0.02
Swift XRT	WT	00031220211	56349.39	423.39	1.4	0.42 ± 0.02
Swift XRT	WT	00031220220	56370.20	444.20	1.6	0.40 ± 0.02
Swift XRT	WT	00031220224	56403.25	477.25	1.0	0.35 ± 0.02
Swift XRT	WT	00031220231	56433.07	507.07	1.2	0.39 ± 0.02
Swift XRT	WT	00031220234	56446.39	520.39	1.1	0.37 ± 0.02
Swift XRT	WT	00031220238	56460.46	534.46	0.8	0.38 ± 0.02
XMM–Newton EPN	FF	0723330101	56496.13	570.13	48.3	2.395 ± 0.007
Swift XRT	WT	00031220246	56502.12	576.12	1.5	0.36 ± 0.02
Swift XRT	WT	00031220249	56516.07	590.07	1.4	0.32 ± 0.02
Swift XRT	WT	00032923002	56538.55	612.55	1.4	0.37 ± 0.02
Swift XRT	WT	00032923008	56566.38	640.38	1.3	0.33 ± 0.02
Swift XRT	WT	00032923012	56581.48	655.48	1.5	0.35 ± 0.02
Swift XRT	WT	00032923014	56594.45	668.45	1.6	0.37 ± 0.02
Swift XRT	WT	00032923016	56609.42	683.42	1.4	0.36 ± 0.02
Swift XRT	WT	00032923023	56650.12	724.12	1.4	0.28 ± 0.01
Swift XRT	WT	00032923026	56664.07	738.07	1.4	0.30 ± 0.01
Swift XRT	WT	00032923029	56678.27	752.27	0.8	0.20 ± 0.02
Swift XRT	WT	00032923039	56721.45	795.45	1.7	0.28 ± 0.01
Swift XRT	WT	00032923048	56763.87	837.87	1.4	0.31 ± 0.02
Swift XRT	WT	00032923058	56805.72	879.72	1.3	0.32 ± 0.02
Swift XRT	WT	00032923069	56848.78	922.78	1.8	0.31 ± 0.01
Swift XRT	WT	00032923078	56875.20	949.20	1.5	0.29 ± 0.01
Swift XRT	WT	00032923082	56885.53	959.53	1.2	0.27 ± 0.02

Table A17. Log of the X-ray observations of 1E 1048.1−5937 following the 2016 July outburst. No burst signalling the outburst onset was detected in this case. The outburst onset is thus considered to be occurred on ∼ MJD 57592, when an increase in the X-ray flux was measured (the previous *Swift* observation was carried out on MJD 57588; Archibald et al. 2016b). The source is currently being regularly monitored by *Swift*.

Instrument	Mode	Obs. ID	Mid-point of observation (MJD)	Time since outburst onset (d)	Exposure (ks)	Source net count rate (counts s^{-1})
Swift XRT	WT	00032923248	57592.49	0.49	1.2	0.85 ± 0.03
Swift XRT	WT	00032923249	57598.47	6.47	1.4	0.95 ± 0.03
Swift XRT	WT	00032923250	57598.80	6.80	1.1	0.81 ± 0.03
Swift XRT	WT	00032923251	57605.97	13.97	0.3	0.55 ± 0.04
Swift XRT	WT	00032923252	57607.53	15.53	0.9	0.78 ± 0.03
Swift XRT	WT	00032923253	57608.27	16.27	0.6	0.56 ± 0.03
Swift XRT	WT	00032923254	57608.38	16.38	1.0	0.65 ± 0.03
Swift XRT	WT	00032923255	57612.02	20.02	0.6	0.69 ± 0.03
Swift XRT	WT	00030912012	57612.65	20.65	1.4	0.87 ± 0.02
Swift XRT	WT	00030912013	57613.61	21.61	1.4	0.47 ± 0.02
Swift XRT	WT	00030912016	57627.91	35.91	0.1	0.59 ± 0.07
Swift XRT	WT	00030912019	57628.11	36.11	0.9	0.51 ± 0.02
Swift XRT	WT	00030912017	57629.45	37.45	1.2	0.63 ± 0.02
Swift XRT	WT	00030912020	57633.13	41.13	1.5	0.47 ± 0.02
Swift XRT	WT	00030912022	57634.82	42.82	0.6	0.67 ± 0.03
Swift XRT	WT	00030912025	57640.20	48.20	1.6	0.65 ± 0.21
Swift XRT	WT	00030912023	57640.50	48.50	1.4	0.51 ± 0.02
Swift XRT	WT	00030912024	57641.40	49.40	1.5	0.54 ± 0.02
Swift XRT	WT	00030912026	57654.15	62.15	1.5	0.58 ± 0.02
Swift XRT	WT	00030912027	57654.39	62.39	1.3	0.53 ± 0.02
Swift XRT	WT	00030912028	57655.15	63.15	1.4	0.52 ± 0.02
Swift XRT	WT	00030912029	57667.27	75.27	1.5	0.49 ± 0.02
Swift XRT	WT	00030912030	57667.41	75.41	1.1	0.44 ± 0.02
Swift XRT	WT	00030912031	57668.20	76.20	1.4	0.52 ± 0.02
Swift XRT	WT	00030912032	57677.45	85.45	1.1	0.52 ± 0.02
Swift XRT	WT	00030912033	57677.85	85.85	1.6	0.53 ± 0.02
Swift XRT	WT	00030912035	57687.12	95.12	1.4	0.53 ± 0.02
Swift XRT	WT	00030912036	57687.58	95.58	1.5	0.42 ± 0.02
Swift XRT	WT	00030912037	57688.17	96.17	1.5	0.52 ± 0.02
Swift XRT	WT	00030912038	57697.08	105.08	1.6	0.55 ± 0.02
Swift XRT	WT	00030912040	57698.84	106.84	1.4	0.35 ± 0.02
Swift XRT	WT	00030912041	57707.35	115.35	1.0	0.38 ± 0.02
Swift XRT	WT	00030912042	57707.60	115.60	1.5	0.53 ± 0.02
Swift XRT	WT	00030912043	57708.80	116.80	1.4	0.33 ± 0.02
Swift XRT	WT	00030912044	57717.34	125.34	1.4	0.39 ± 0.02
Swift XRT	WT	00030912045	57717.73	125.73	1.5	0.48 ± 0.02
Swift XRT	WT	00030912046	57718.87	126.87	1.4	0.43 ± 0.02
Swift XRT	WT	00030912047	57727.02	135.02	1.4	0.39 ± 0.02
Swift XRT	WT	00030912048	57727.55	135.55	1.5	0.42 ± 0.02
Swift XRT	WT	00030912049	57728.45	136.45	1.5	0.42 ± 0.02
Swift XRT	WT	00030912050	57737.22	145.22	1.1	0.49 ± 0.02
Swift XRT	WT	00030912051	57737.45	145.45	1.3	0.43 ± 0.02
Swift XRT	WT	00030912052	57738.08	146.08	1.5	0.51 ± 0.02
Swift XRT	WT	00030912053	57747.15	155.15	1.4	0.46 ± 0.02
Swift XRT	WT	00030912054	57747.61	155.61	1.6	0.42 ± 0.02
Swift XRT	WT	00030912055	57748.77	156.77	1.5	0.27 ± 0.01
Swift XRT	WT	00030912057	57758.77	166.77	1.4	0.41 ± 0.02
Swift XRT	WT	00030912058	57759.49	167.49	1.3	0.39 ± 0.02
Swift XRT	WT	00030912059	57778.18	186.18	1.5	0.46 ± 0.02
Swift XRT	WT	00030912060	57778.57	186.57	1.4	0.45 ± 0.02
Swift XRT	WT	00030912061	57779.68	187.68	1.4	0.111 ± 0.009
Swift XRT	WT	00030912062	57785.06	193.06	1.6	0.40 ± 0.02
Swift XRT	WT	00030912063	57785.89	193.89	1.4	0.40 ± 0.02
Swift XRT	WT	00030912064	57786.09	194.09	1.5	0.41 ± 0.02
Swift XRT	WT	00030912065	57793.04	201.04	0.3	0.46 ± 0.04
Swift XRT	WT	00030912066	57794.92	202.92	1.5	0.39 ± 0.02
Swift XRT	WT	00030912067	57796.87	204.87	0.6	0.36 ± 0.02
Swift XRT	WT	00030912068	57797.82	205.82	1.1	0.38 ± 0.02
Swift XRT	WT	00030912069	57803.21	211.21	1.4	0.38 ± 0.02
Swift XRT	WT	00030912070	57803.86	211.86	1.5	0.43 ± 0.02

Table A18. Log of *Chandra* observations of SGR 1745−2900 following the 2013 April outburst. The outburst onset occurred on MJD 56407.80237269 (Barthelmy et al. 2013). All reported count rates are not corrected for pile-up. Part of these observations were already analysed by Rea et al. (2013b) and Coti Zelati et al. (2015a, 2017).

Instrument	Mode	Obs. ID	Mid-point of observation (MJD)	Time since outburst onset (d)	Exposure (ks)	Source net count rate (counts s^{-1})
Chandra/HRC -S	TE	14701	56411.70	3.90	9.7	0.081 ± 0.003
Chandra ACIS-S	TE	14702	56424.55	16.75	13.7	0.545 ± 0.006
Chandra/HETG	TE	15040	56437.63	29.83	23.8	0.150 ± 0.003
Chandra ACIS-S	TE	14703	56447.48	39.68	16.8	0.455 ± 0.005
Chandra//HETG	TE	15651	56448.99	41.19	13.8	0.141 ± 0.003
Chandra/HETG	TE	15654	56452.25	44.45	9.0	0.128 ± 0.004
Chandra ACIS-S	TE	14946	56475.41	67.61	18.2	0.392 ± 0.005
Chandra ACIS-S	TE	15041	56500.36	92.56	45.4	0.346 ± 0.003
Chandra ACIS-S	TE	15042	56516.25	108.45	45.7	0.317 ± 0.003
Chandra ACIS-S	TE	14945	56535.55	127.75	18.2	0.290 ± 0.004
Chandra ACIS-S	TE	15043	56549.30	141.50	45.4	0.275 ± 0.002
Chandra ACIS-S	TE	14944	56555.42	147.62	18.2	0.273 ± 0.004
Chandra ACIS-S	TE	15044	56570.01	162.21	42.7	0.255 ± 0.002
Chandra ACIS-S	TE	14943	56582.78	174.98	18.2	0.246 ± 0.004
Chandra ACIS-S	TE	14704	56588.62	180.82	36.3	0.240 ± 0.003
Chandra ACIS-S	TE	15045	56593.91	186.11	45.4	0.234 ± 0.002
Chandra ACIS-S	TE	16508	56709.77	301.97	43.4	0.156 ± 0.002
Chandra ACIS-S	TE	16211	56730.71	322.91	41.8	0.149 ± 0.002
Chandra ACIS-S	TE	16212	56751.40	343.60	45.4	0.135 ± 0.002
Chandra ACIS-S	TE	16213	56775.41	367.61	45.0	0.128 ± 0.002
Chandra ACIS-S	TE	16214	56797.31	389.51	45.4	0.118 ± 0.002
Chandra ACIS-S	TE	16210	56811.24	403.44	17.0	0.110 ± 0.003
Chandra ACIS-S	TE	16597	56842.98	435.18	16.5	0.097 ± 0.002
Chandra ACIS-S	TE	16215	56855.22	447.42	41.5	0.090 ± 0.001
Chandra ACIS-S	TE	16216	56871.43	463.63	42.7	0.085 ± 0.001
Chandra ACIS-S	TE	16217	56899.43	491.63	34.5	0.079 ± 0.002
Chandra ACIS-S	TE	16218	56950.59	542.79	36.3	0.071 ± 0.001
Chandra ACIS-S	TE	16963	57066.18	658.38	22.7	0.056 ± 0.002
Chandra ACIS-S	TE	16966	57156.53	748.72	22.7	0.045 ± 0.001
Chandra ACIS-S	TE	16965	57251.60	843.80	22.7	0.035 ± 0.001
Chandra ACIS-S	TE	16964	57316.41	908.60	22.6	0.026 ± 0.001
Chandra ACIS-S	TE	18055	57431.53	1023.73	22.7	0.0133 ± 0.0008
Chandra ACIS-S	TE	18056	57432.76	1024.96	21.8	0.0146 ± 0.0009
Chandra ACIS-S	TE	18731	57582.27	1174.47	78.4	0.0102 ± 0.0004
Chandra ACIS-S	TE	18732	57588.00	1180.20	76.6	0.0118 ± 0.0004
Chandra ACIS-S	TE	18057	57669.95	1262.15	22.7	0.0130 ± 0.0008
Chandra ACIS-S	TE	18058	57675.61	1267.80	22.7	0.0135 ± 0.00081

Table A19. Log of all X-ray observations of SGR 1935+2154 following the 2014 July outburst. The outburst onset occurred on MJD 56843.39777778 (Stamatikos et al. 2014). Part of these observations were already analysed by Israel et al. (2016).

Instrument	Mode	Obs. ID	Mid-point of observation (MJD)	Time since outburst onset (d)	Exposure (ks)	Source net count rate (counts s^{-1})
Swift XRT	PC	00603488000	56843.44	0.04	3.4	0.033 ± 0.003
Swift XRT	PC	00603488001	56844.72	0.32	9.9	0.027 ± 0.002
Swift XRT	PC	00603488003	56845.36	1.96	3.9	0.019 ± 0.002
Swift XRT	PC	00603488006	56846.77	3.37	3.7	0.028 ± 0.003
Swift XRT	PC	00603488007	56847.67	4.27	3.6	0.018 ± 0.002
Swift XRT	PC	00603488009	56851.39	7.99	3.0	0.025 ± 0.003
Swift XRT	PC	00603488008	56851.62	8.23	5.3	0.022 ± 0.002
Chandra ACIS-S	TE	15874	56853.66	10.26	9.1	0.110 ± 0.003
Swift XRT	PC	00603488010	56854.51	11.11	7.1	0.024 ± 0.002
Swift XRT	PC	00603488011	56858.54	15.14	2.9	0.019 ± 0.003
Chandra ACIS-S	CC	15875	56866.48	23.08	75.1	0.115 ± 0.001
Swift XRT	PC	00033349001	56869.76	26.36	2.1	0.019 ± 0.003
Swift XRT	PC	00033349002	56876.70	33.30	2.2	0.022 ± 0.003
Swift XRT	PC	00033349003	56883.75	40.35	1.5	0.023 ± 0.004
Swift XRT	PC	00033349004	56890.41	47.01	1.7	0.019 ± 0.003
Swift XRT	PC	00033349005	56894.65	51.25	3.7	0.020 ± 0.002
Swift XRT	PC	00033349006	56897.55	54.15	1.7	0.022 ± 0.004
Chandra ACIS-S	CC	17314	56900.21	56.81	29.0	0.107 ± 0.002
Swift XRT	PC	00033349007	56904.79	61.39	1.1	0.016 ± 0.004
Swift XRT	PC	00033349008	56906.51	63.11	1.5	0.022 ± 0.004
Swift XRT	PC	00033349009	56911.27	67.88	1.5	0.023 ± 0.004
Swift XRT	PC	00033349010	56914.31	70.91	2.4	0.024 ± 0.003
Swift XRT	PC	00033349011	56918.57	75.17	1.4	0.019 ± 0.004
Swift XRT	PC	00033349012	56924.50	81.10	2.3	0.019 ± 0.003
XMM–Newton EPN	FF	0722412501	56927.06	83.66	16.9	0.190 ± 0.003
XMM–Newton EPN	FF	0722412601	56928.32	84.92	17.8	0.189 ± 0.003
XMM–Newton EPN	FF	0722412701	56934.36	90.96	16.1	0.197 ± 0.004
XMM–Newton EPN	FF	0722412801	56946.17	102.77	8.6	0.194 ± 0.005
XMM–Newton EPN	FF	0722412901	56954.19	110.79	6.4	0.201 ± 0.006
XMM–Newton EPN	FF	0722413001	56958.03	114.63	11.2	0.189 ± 0.004
XMM–Newton EPN	FF	0748390801	56976.27	132.87	9.5	0.194 ± 0.005
Swift XRT	PC	00632158000	57075.59	232.19	7.3	0.039 ± 0.002
Swift XRT	PC	00632158001	57075.84	232.44	1.8	0.042 ± 0.005
Swift XRT	PC	00632158002	57076.59	233.19	5.9	0.028 ± 0.002
Swift XRT	PC	00033349014	57078.48	235.08	3.1	0.030 ± 0.003
Swift XRT	PC	00033349015	57080.35	236.95	5.9	0.022 ± 0.002
Swift XRT	PC	00033349016	57085.51	242.11	3.9	0.025 ± 0.003
Swift XRT	PC	00033349017	57092.69	249.29	3.9	0.023 ± 0.002
XMM–Newton EPN	FF	0764820101	57106.59	263.19	26.5	0.250 ± 0.003
Swift XRT	PC	00033349020	57127.83	284.43	3.0	0.014 ± 0.002
Swift XRT	PC	00033349023	57134.62	291.22	1.4	0.029 ± 0.005
Swift XRT	PC	00033349024	57221.00	377.60	2.0	0.025 ± 0.004
XMM–Newton EPN	FF	0764820201	57303.04	459.65	11.4	0.207 ± 0.004
Swift XRT	PC	00033349025	57377.77	534.37	3.9	0.017 ± 0.002
Swift XRT	PC	00686761000	57526.42	683.02	1.6	0.058 ± 0.006
Swift XRT	PC	00033349026	57527.81	684.41	2.9	0.020 ± 0.003
Swift XRT	PC	00687123000	57529.84	686.45	1.2	0.026 ± 0.005
Swift XRT	PC	00033349027	57534.44	691.04	2.3	0.017 ± 0.003
Swift XRT	PC	00033349028	57539.99	696.51	2.8	0.015 ± 0.002
Swift XRT	PC	00033349030	57548.89	705.49	1.7	0.014 ± 0.003
Swift XRT	PC	00033349031	57554.23	710.83	2.6	0.020 ± 0.003
Swift XRT	PC	00033349032	57561.42	718.02	1.6	0.020 ± 0.004
Swift XRT	PC	00033349033	57567.59	724.19	2.0	0.023 ± 0.003
Swift XRT	PC	00033349034	57569.82	726.42	2.4	0.019 ± 0.003
Swift XRT	PC	00033349035	57576.88	733.48	2.8	0.020 ± 0.003
Swift XRT	PC	00033349036	57586.36	742.96	2.5	0.020 ± 0.003
Swift XRT	PC	00033349037	57597.51	754.11	2.8	0.024 ± 0.003

Table A20. Log of all X-ray observations of PSR J1119−6127 following the 2016 July outburst. The outburst onset occurred on MJD 57597.06100694 (Kennea et al. 2016). Part of these observations were already analysed by Archibald et al. (2016a).

Instrument	Mode	Obs. ID	Mid-point of observation (MJD)	Time since outburst onset (d)	Exposure (ks)	Source net count rate (counts s^{-1})
Swift XRT	PC	00706396000	57597.08	0.01	2.2	0.544 ± 0.02
Swift XRT	WT	00034632001	57597.93	0.87	9.6	0.510 ± 0.008
Swift XRT	WT	00034632002	57601.02	3.95	4.8	0.53 ± 0.01
Swift XRT	PC	00034632003	57603.52	6.46	3.0	0.202 ± 0.008
Swift XRT	PC	00034632005	57606.54	9.48	3.0	0.212 ± 0.008
Swift XRT	WT	00034632007	57609.56	12.50	5.5	0.49 ± 0.01
Swift XRT	WT	00034632008	57610.26	13.20	1.3	0.39 ± 0.02
Swift XRT	PC	00034632009	57612.32	15.25	2.3	0.179 ± 0.009
Swift XRT	WT	00034632010	57627.32	30.26	3.0	0.40 ± 0.01
Swift XRT	WT	00034632011	57630.41	33.34	3.2	0.40 ± 0.01
Swift XRT	WT	00034632013	57637.45	40.38	2.1	0.30 ± 0.01
Swift XRT	WT	00034632014	57641.73	44.66	2.4	0.28 ± 0.02
Swift XRT	WT	00034632015	57647.07	50.01	2.1	0.33 ± 0.01
Swift XRT	WT	00034632016	57647.42	50.36	1.7	0.23 ± 0.01
Swift XRT	WT	00034632017	57648.07	51.01	1.9	0.40 ± 0.02
Swift XRT	WT	00034632018	57657.10	60.04	1.9	0.36 ± 0.01
Swift XRT	WT	00034632019	57657.70	60.63	1.9	0.31 ± 0.01
Swift XRT	WT	00034632020	57658.05	60.98	2.1	0.34 ± 0.01
Swift XRT	WT	00034632022	57667.67	70.61	1.6	0.25 ± 0.01
Swift XRT	WT	00034632023	57668.37	71.30	2.0	0.24 ± 0.01
Swift XRT	WT	00034632024	57679.05	81.98	2.0	0.17 ± 0.01
Swift XRT	WT	00034632025	57679.62	82.55	2.0	0.31 ± 0.01
Swift XRT	WT	00034632026	57680.17	83.11	1.8	0.19 ± 0.01
Swift XRT	WT	00034632027	57687.21	90.15	1.9	0.22 ± 0.01
Swift XRT	WT	00034632028	57687.42	90.36	1.9	0.34 ± 0.01
Swift XRT	WT	00034632029	57688.21	91.14	1.7	0.22 ± 0.01
Swift XRT	WT	00034632030	57693.19	96.12	2.1	0.23 ± 0.01
Swift XRT	WT	00034632037	57707.27	110.21	2.5	0.18 ± 0.01
Swift XRT	WT	00034632039	57708.31	111.25	2.0	0.18 ± 0.01
Swift XRT	WT	00034632040	57709.87	112.80	2.1	0.16 ± 0.01
Swift XRT	WT	00034632041	57714.19	117.12	1.9	0.22 ± 0.01
Swift XRT	WT	00034632042	57714.59	117.52	1.9	0.19 ± 0.01
Swift XRT	WT	00034632043	57715.18	118.12	2.1	0.146 ± 0.009
Swift XRT	WT	00034632044	57729.22	132.16	2.6	0.175 ± 0.009
Swift XRT	WT	00034632045	57729.65	132.59	5.5	0.211 ± 0.007
Swift XRT	WT	00034632046	57730.14	133.08	4.9	0.142 ± 0.006

APPENDIX B: *Swift* XRT LIGHT CURVES

This section reports a series of figures showing the cooling curves for magnetar outbursts as observed by the X-ray Telescope on board *Swift* and in terms of the count rate. The 0.3–10 keV light curves were created by exploiting both PC- and WT-mode data, and using the online *Swift* XRT data products generator (http://www.swift.ac.uk/user_objects/). This tool corrects for instrumental artefacts such as pile up and bad columns on the CCD (see Evans et al. 2007, 2009 for more details).

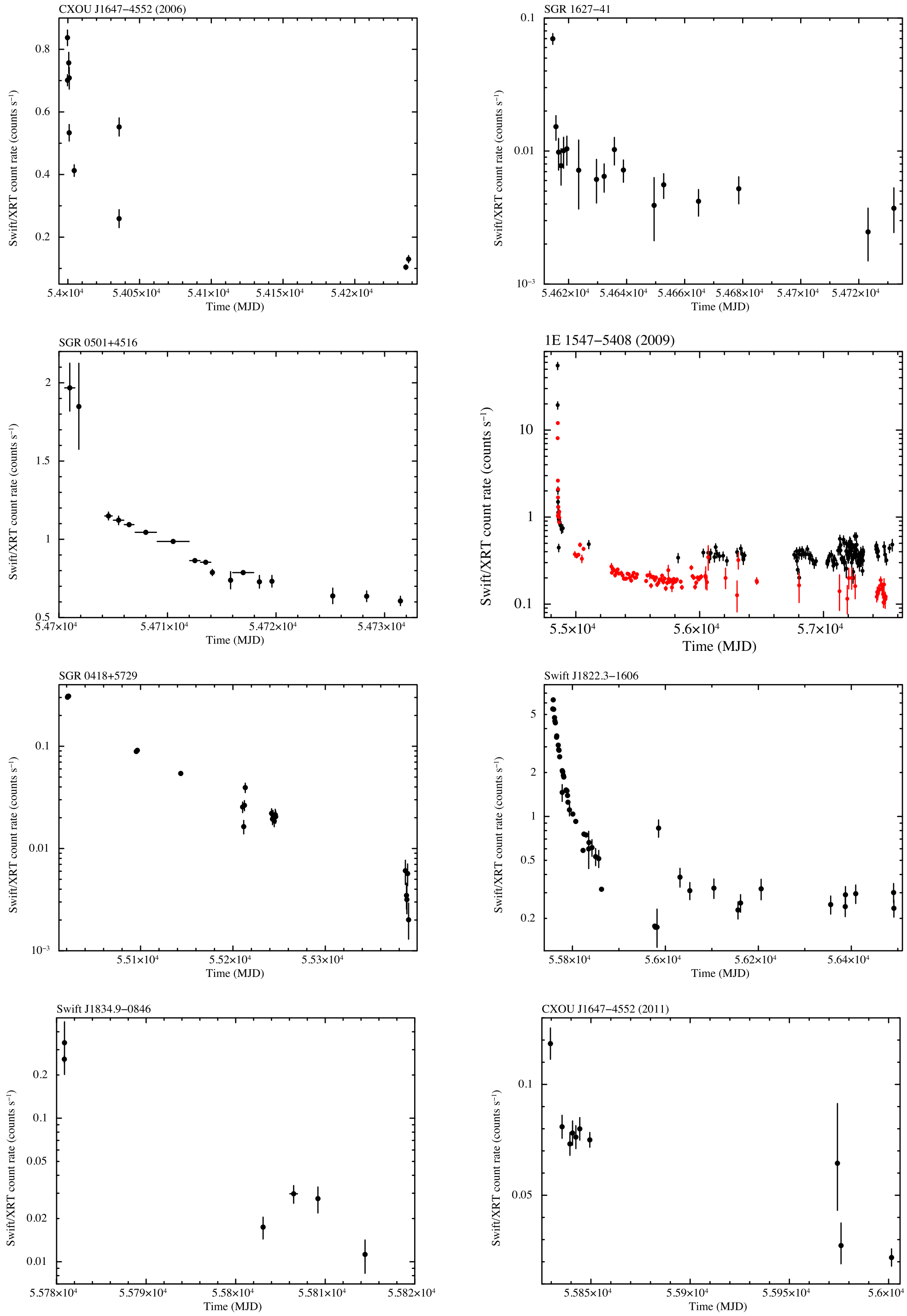

Figure B1. *Swift* XRT long-term 0.3–10 keV light curves of densely monitored magnetar outbursts, created using the online *Swift* XRT data products generator (Evans et al. 2009). In case both PC- and WT-mode data are available, black (red) dots refer to data acquired with the XRT set in WT (PC) mode.

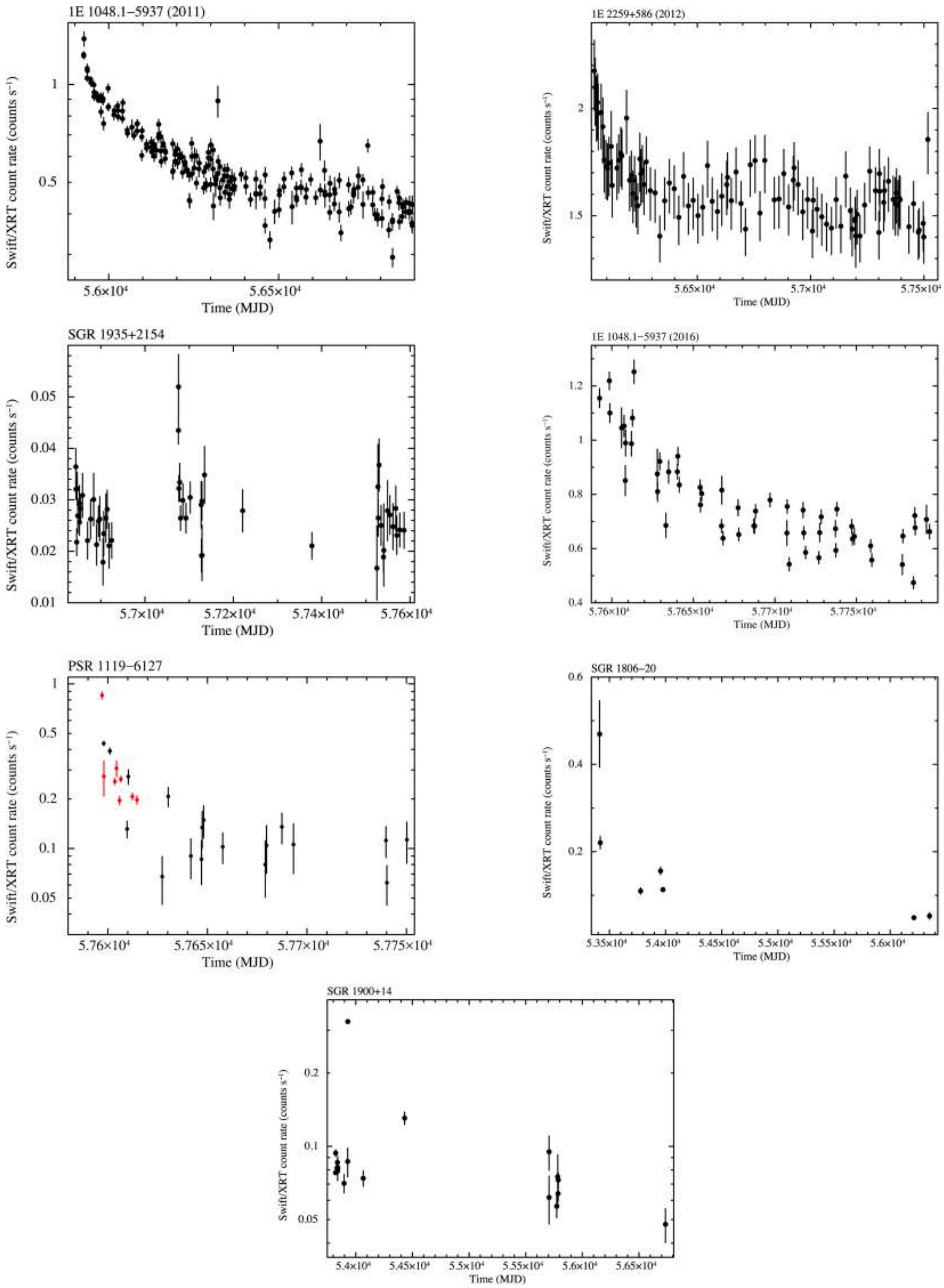

Figure B1 – *continued*

APPENDIX C: HIGH-STATISTICS QUALITY X-RAY SPECTRA AND FITTED MODELS

This section reports a series of figures showing several high-quality spectra and the best-fitting empirical models (see Table 2) for the outbursts that were repeatedly monitored by the *XMM–Newton* or *Chandra* observatories. In each case we plot the $E \times F(E)$ unfolded spectra and the models, to highlight the contributions of the different spectral components to the total X-ray emission (i.e. multiple blackbodies or blackbody plus power law; see the dotted lines in the figures) as a function of time. Post-fit residuals in units of standard deviations are also plotted at the bottom of each panel. In all cases, the data points were re-binned for plotting purpose, to better visualize the trend in the spectral residuals. The colours are associated with the chronological order of the observations according to the following code: black, red, green, blue, light blue, magenta, yellow, orange, yellow+green, green+cyan, blue+cyan, blue+magenta, red+magenta, dark grey, light grey.

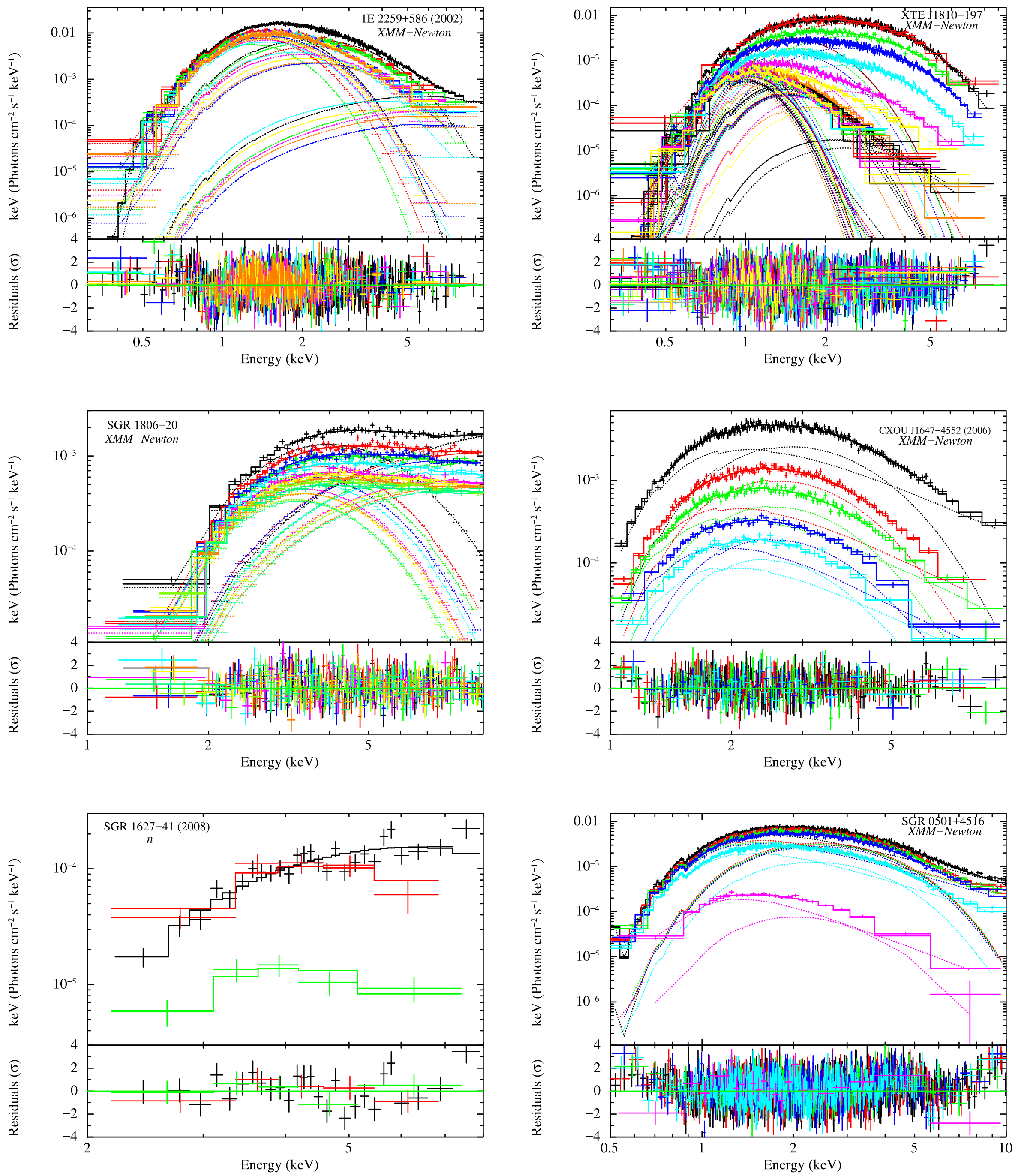

Figure C1. High-quality unfolded spectra for magnetar outbursts that were repeatedly monitored with the *XMM–Newton* or *Chandra* observatories. Best-fitting models are marked by the solid lines, whereas the contributions of the different spectral components are marked by the dotted lines (see Table 2 for more details on the models employed).

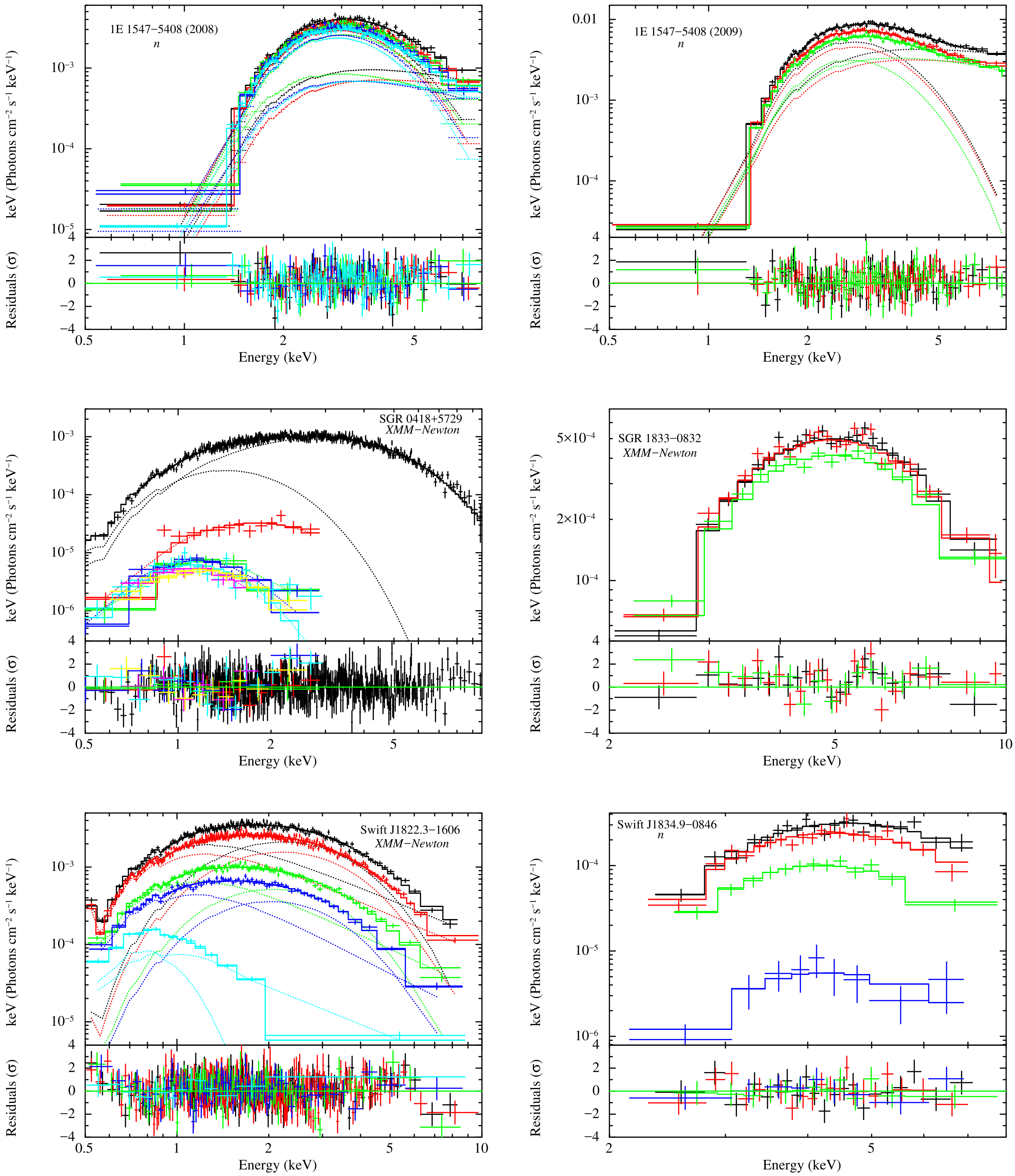

Figure C1 – *continued*

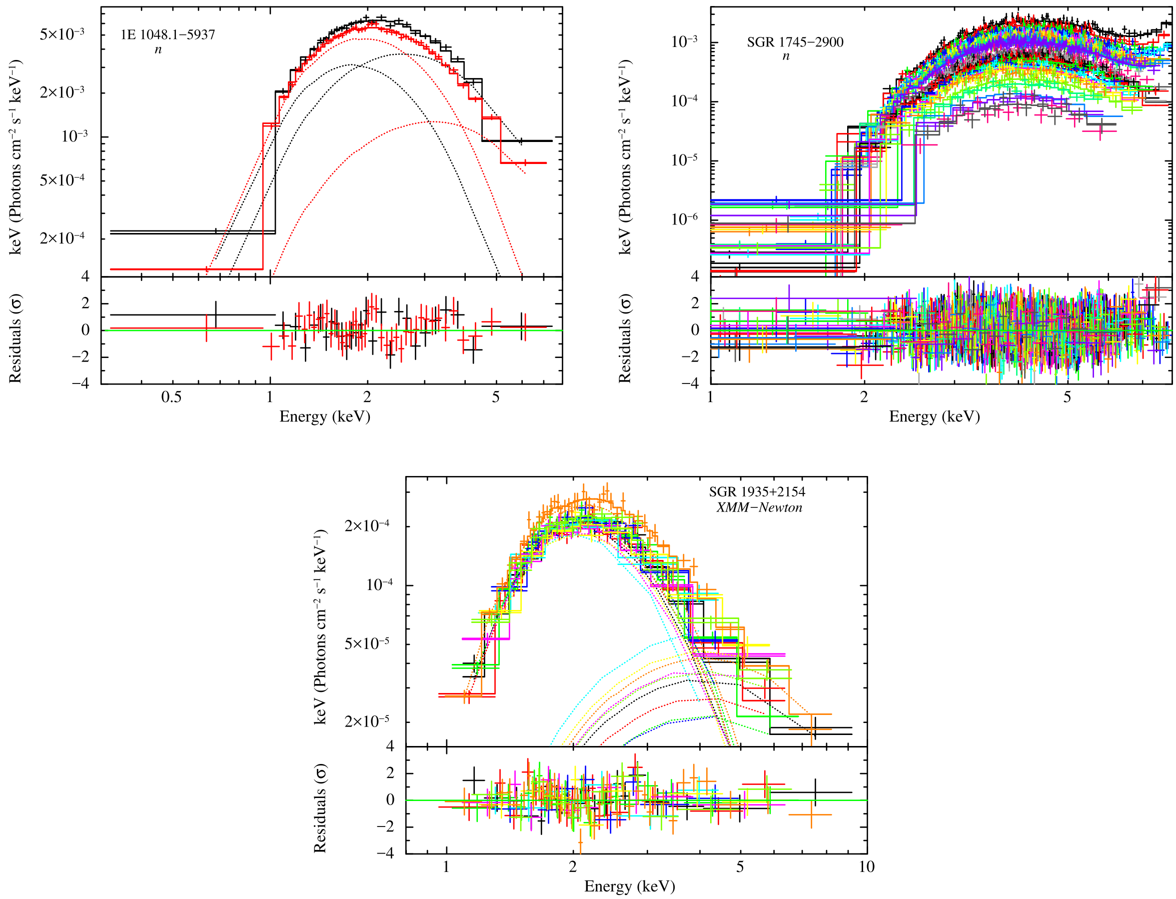

Figure C1 – *continued*

APPENDIX D: OUTBURST LIGHT CURVES

This section shows the cooling curves for all magnetar outbursts re-analysed in this study.

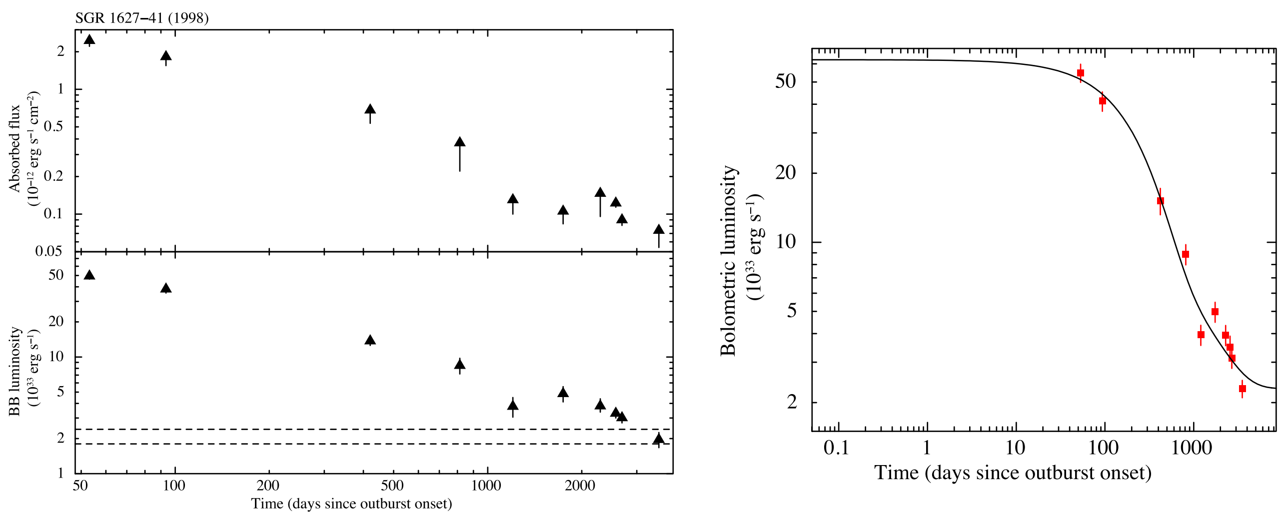

Figure D1. Left-hand panel: temporal evolution of the fluxes and luminosities for the BB model applied to the X-ray data of the 1998 outburst of SGR 1627−41. The dashed lines mark the 1σ c.l. range for the quiescent luminosity (see Table 4). A distance of 11 kpc was assumed. Right-hand panel: temporal evolution of the bolometric luminosity with the best-fitting decay model superimposed.

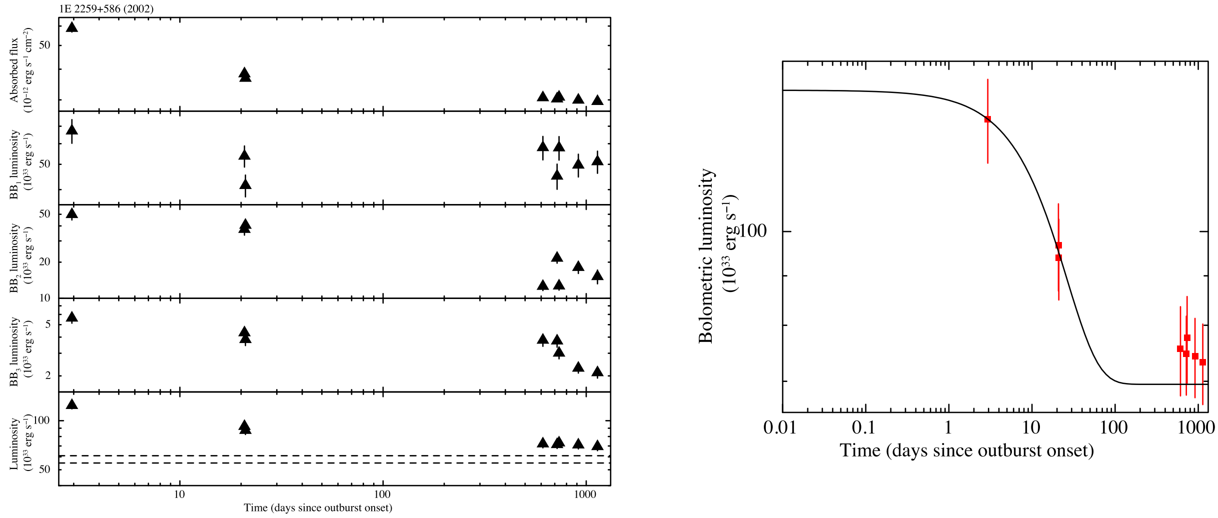

Figure D2. Left-hand panel: temporal evolution of the fluxes and luminosities for the 3BB model applied to the *XMM–Newton* data of the 2002 outburst of 1E 2259+586. The dashed lines mark the 1σ c.l. range for the quiescent luminosity (see Table 4). A distance of 3.2 kpc was assumed. Right-hand panel: temporal evolution of the bolometric luminosity with the best-fitting decay model superimposed.

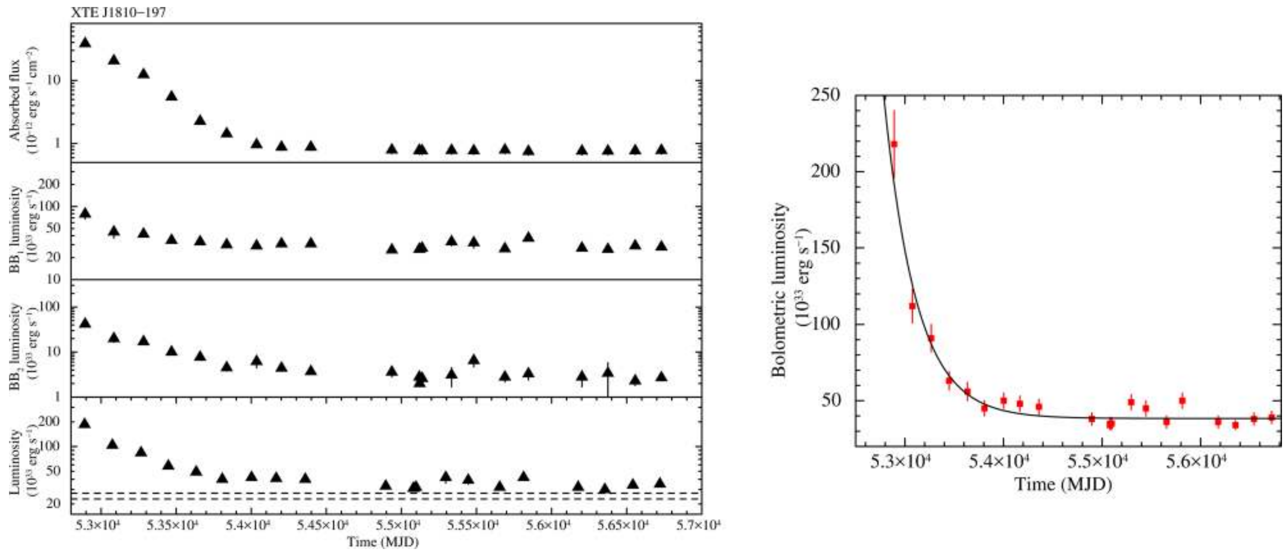

Figure D3. Left-hand panel: temporal evolution of the fluxes and luminosities of the cold and warm blackbody components for the 3BB+2BB model applied to the *XMM–Newton* data of the 2003 outburst of XTE J1810−197. The dashed lines mark the 1σ c.l. range for the quiescent luminosity (see Table 4). A distance of 3.5 kpc was assumed. Right-hand panel: temporal evolution of the bolometric luminosity with the best-fitting decay model superimposed.

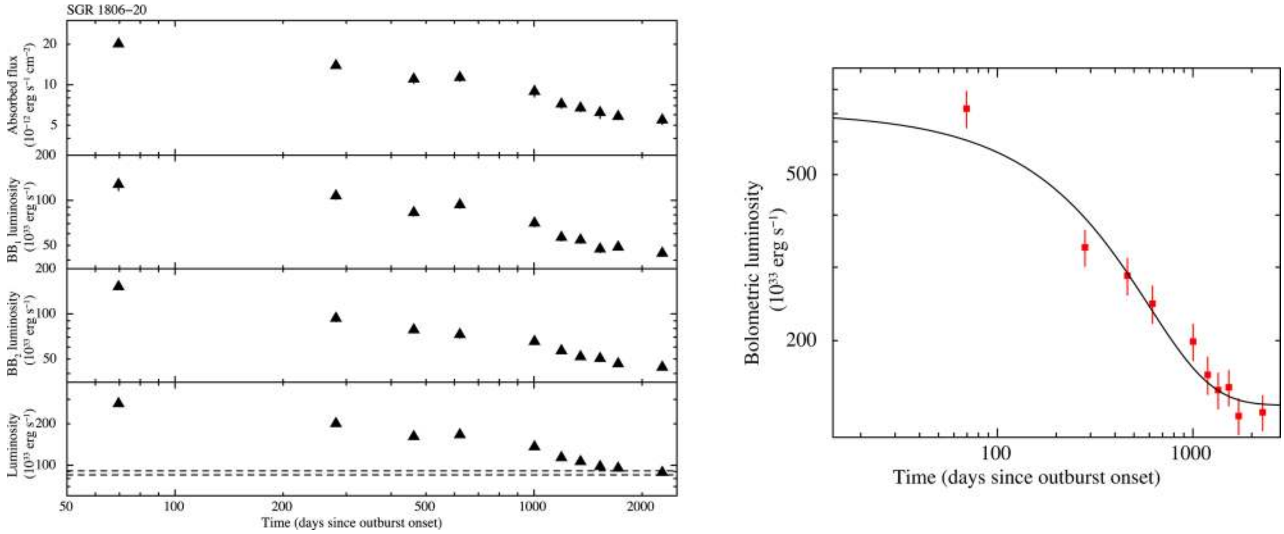

Figure D4. Left-hand panel: temporal evolution of the fluxes and luminosities for the 2BB model applied to the *XMM–Newton* data of SGR 1806−20. The dashed lines mark the 1σ c.l. range for the quiescent luminosity (see Table 4). A distance of 8.7 kpc was assumed. Right-hand panel: temporal evolution of the bolometric luminosity with the best-fitting decay model superimposed.

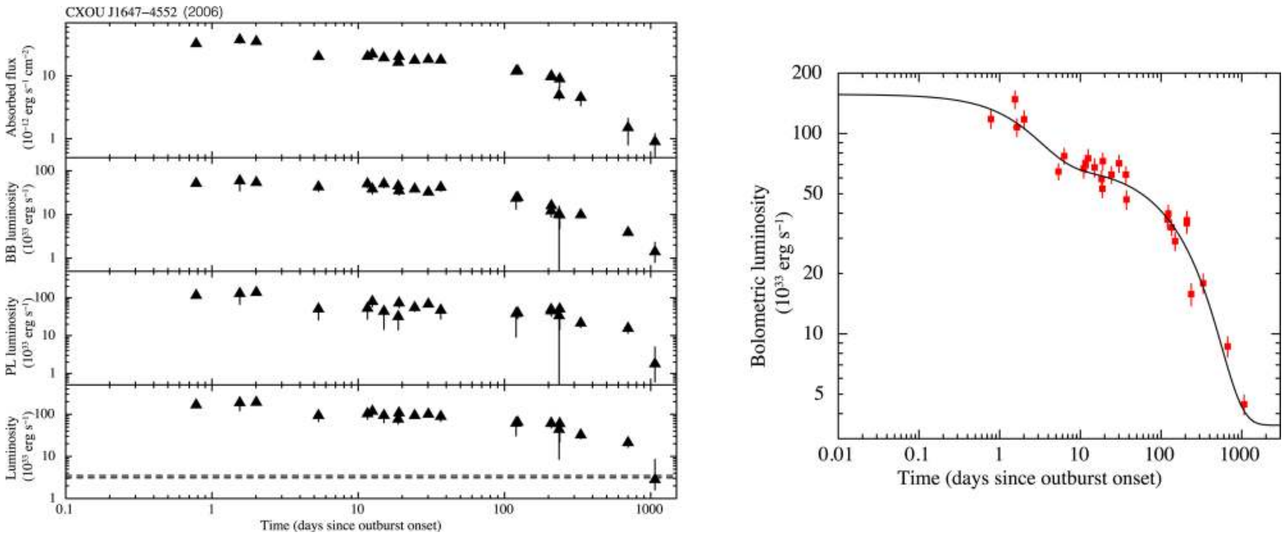

Figure D5. Left-hand panel: temporal evolution of the fluxes and luminosities for the BB+PL model applied to the X-ray data of CXOU J164710.2−455216. The dashed lines mark the 1σ c.l. range for the quiescent luminosity (see Table 4). A distance of 4 kpc was assumed. Right-hand panel: temporal evolution of the bolometric luminosity with the best-fitting decay model superimposed.

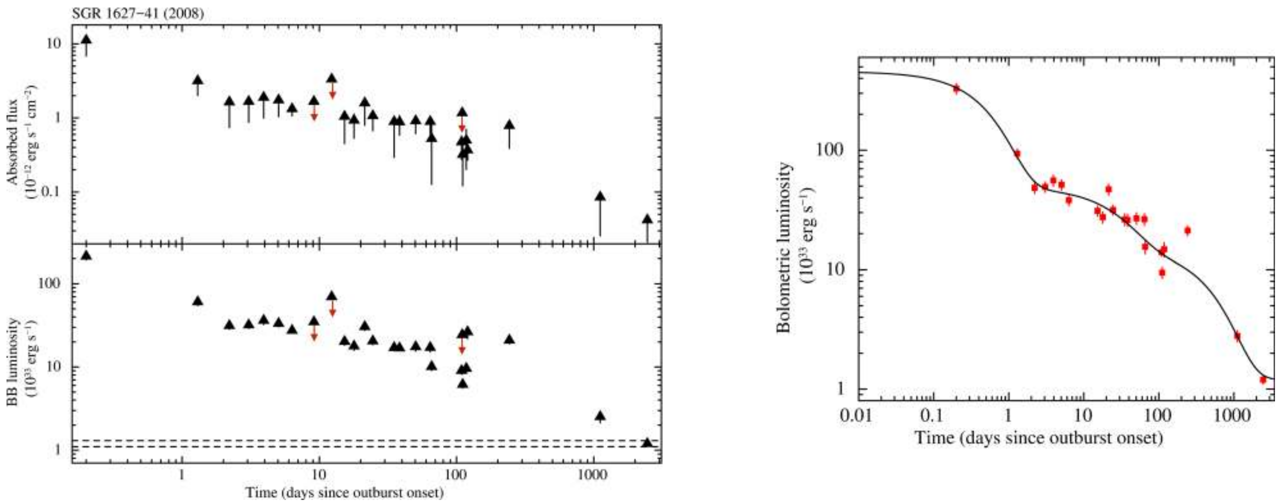

Figure D6. Left-hand panel: temporal evolution of the fluxes and luminosities for the BB model applied to the X-ray data of the 2008 outburst of SGR 1627−41. The dashed lines mark the 1σ c.l. range for the quiescent luminosity (see Table 4). The red downward arrowheads indicate the 3σ upper limits. A distance of 11 kpc was assumed. Right-hand panel: temporal evolution of the bolometric luminosity with the best-fitting decay model superimposed.

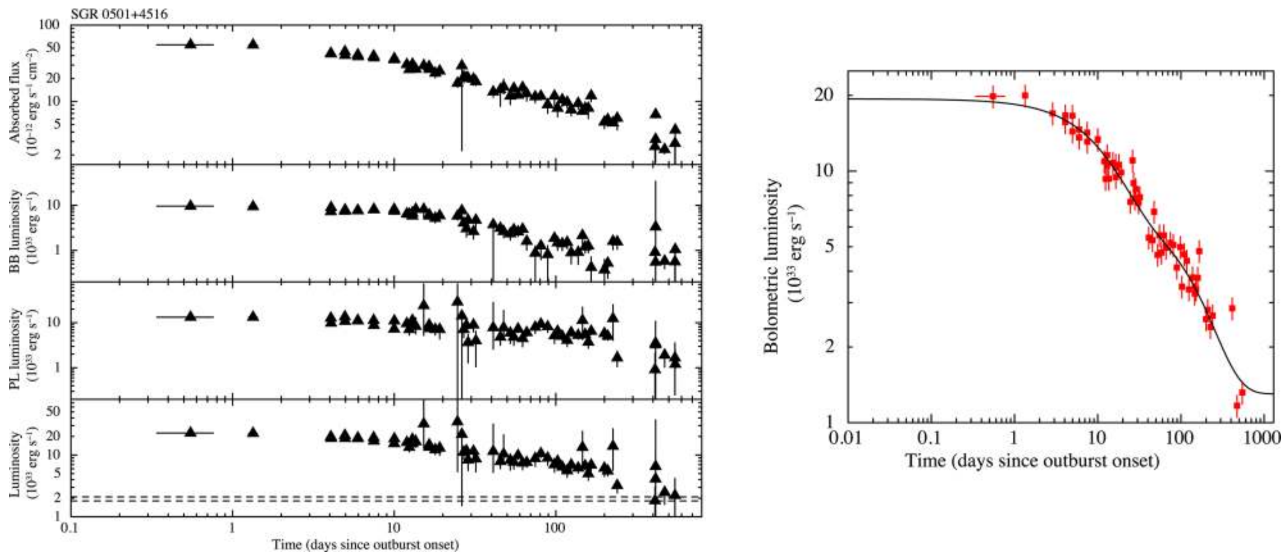

Figure D7. Left-hand panel: temporal evolution of the fluxes and luminosities for the BB+PL model applied to the *Swift* XRT data of SGR 0501+4516. The dashed line marks the approximate value for the quiescent luminosity (see Table 4). A distance of 1.5 kpc was assumed. Right-hand panel: temporal evolution of the bolometric luminosity with the best-fitting decay model superimposed.

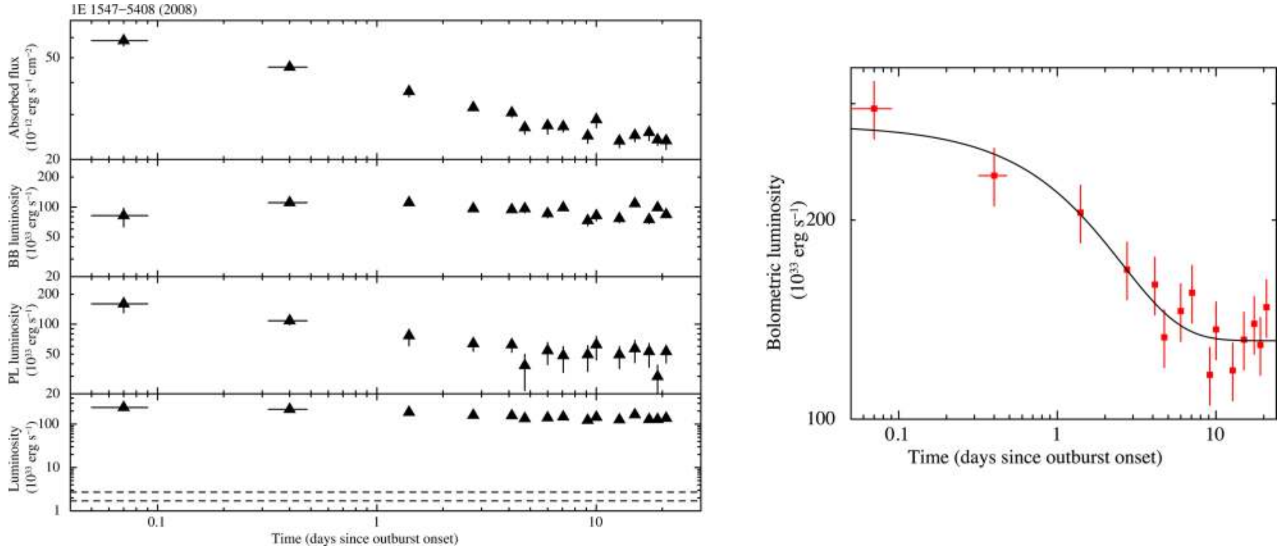

Figure D8. Left-hand panel: temporal evolution of the fluxes and luminosities for the BB+PL model applied to the *Swift* XRT data of the 2008 outburst of 1E 1547−5408. The dashed lines mark the 1-σ c.l. range for the quiescent luminosity (see Table 4). A distance of 4.5 kpc was assumed. Right-hand panel: temporal evolution of the bolometric luminosity with the best-fitting decay model superimposed.

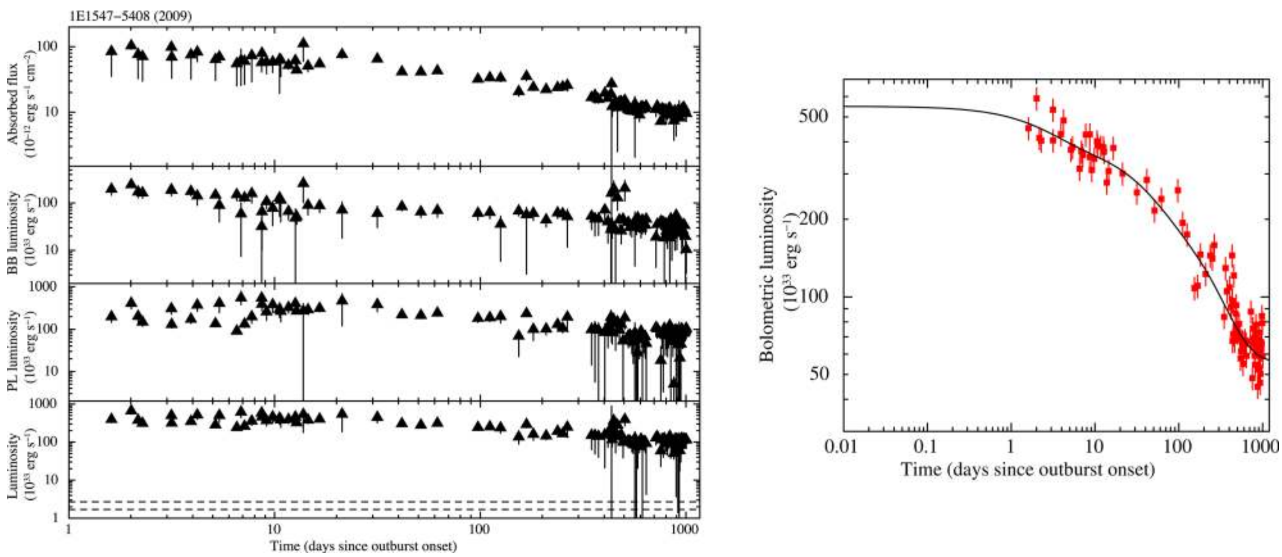

Figure D9. Left-hand panel: temporal evolution of the fluxes and luminosities for the BB+PL model applied to the *Swift* XRT data of the 2009 outburst of 1E 1547−5408. The dashed lines mark the 1-σ c.l. range for the quiescent luminosity (see Table 4). A distance of 4.5 kpc was assumed. Right-hand panel: temporal evolution of the bolometric luminosity with the best-fitting decay model superimposed.

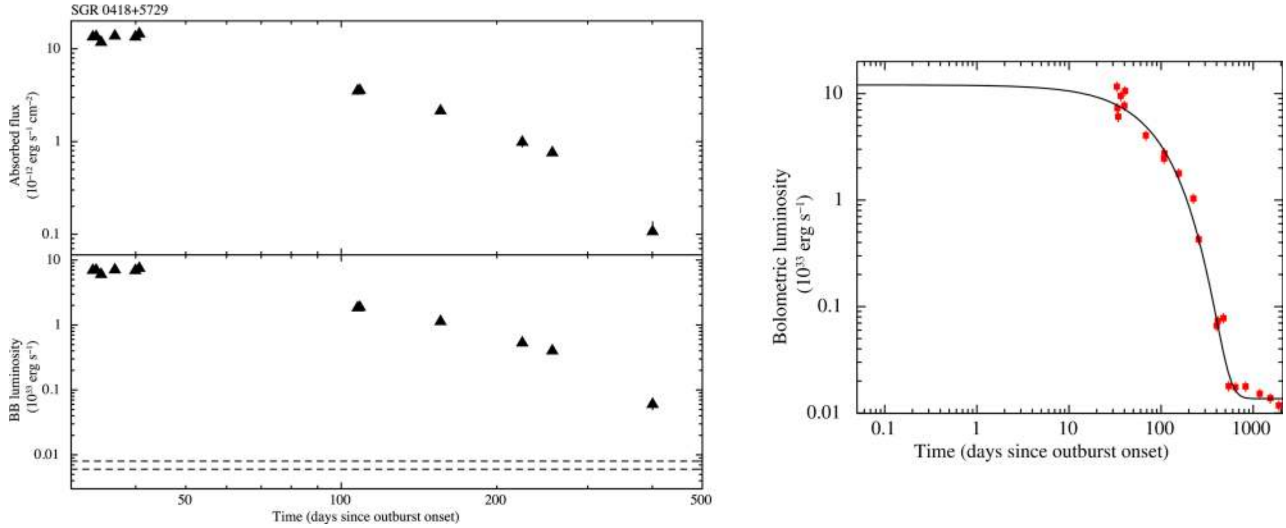

Figure D10. Left-hand panel: temporal evolution of the fluxes and luminosities for the BB model applied to the *Swift* XRT data of the outburst of SGR 0418+5729. The dashed lines mark the 1-σ c.l. range for the quiescent luminosity (see Table 4). A distance of 2 kpc was assumed. Right-hand panel: temporal evolution of the bolometric luminosity with the best-fitting decay model superimposed.

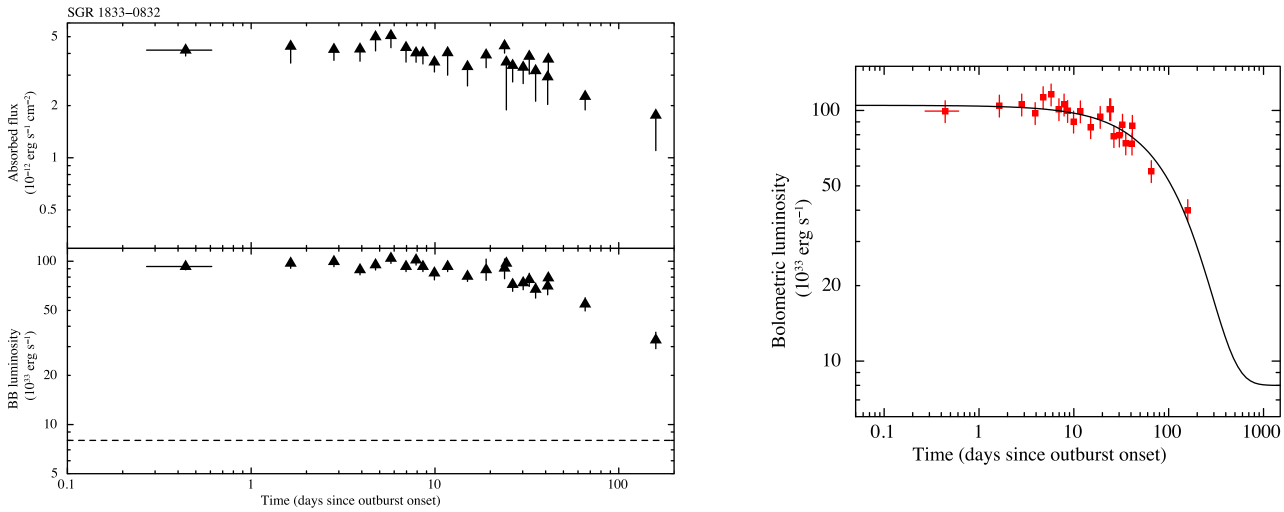

Figure D11. Left-hand panel: temporal evolution of the fluxes and luminosities for the BB+PL model applied to the *Swift* XRT data of the outburst of SGR 1833−0832. The dashed line marks the upper limit (at the 3σ c.l.) for the quiescent luminosity (see Table 4). A distance of 10 kpc was assumed. Right-hand panel: temporal evolution of the bolometric luminosity with the best-fitting decay model superimposed.

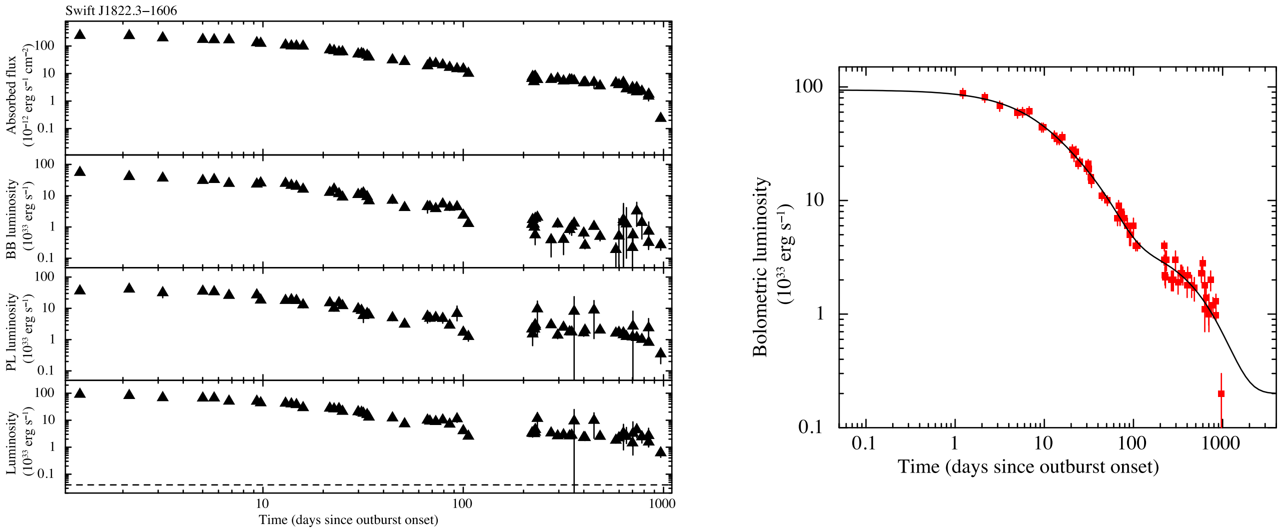

Figure D12. Left-hand panel: temporal evolution of the fluxes and luminosities for the BB+PL model applied to the outburst of Swift J1822.3−1606. The dashed line marks the value for the quiescent luminosity (see Table 4). A distance of 1.6 kpc was assumed. Right-hand panel: temporal evolution of the bolometric luminosity with the best-fitting decay model superimposed.

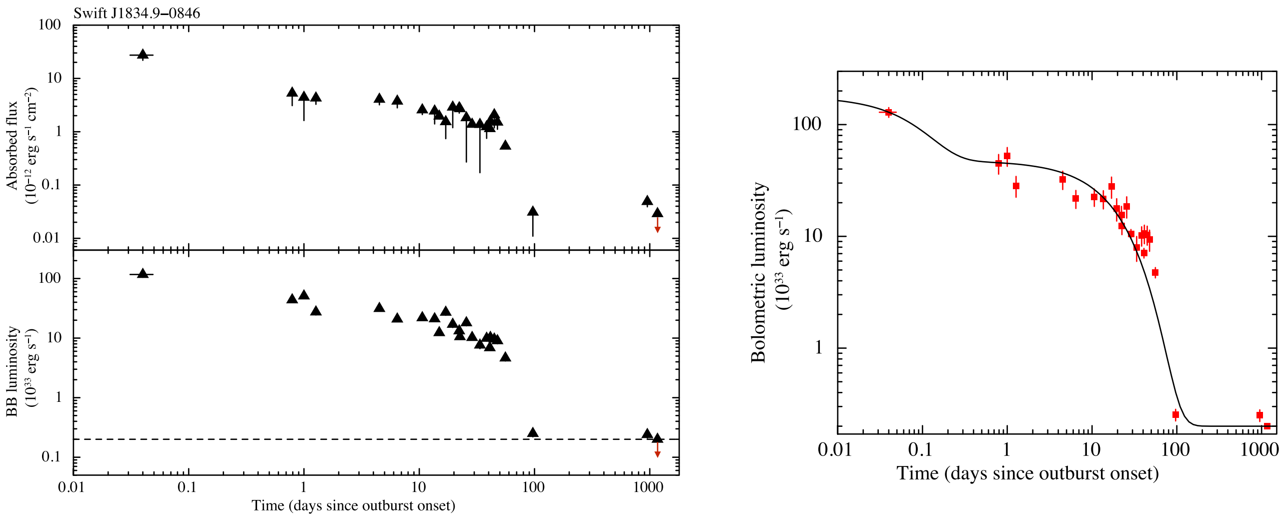

Figure D13. Left-hand panel: temporal evolution of the fluxes and luminosities for the BB model applied to the X-ray data of the outburst of Swift J1834.9−0846. The dashed line marks the upper limit (at the 3σ c.l.) for the quiescent luminosity (see Table 4). The red downward arrowheads indicate the 3σ upper limits. A distance of 4.2 kpc was assumed. Right-hand panel: temporal evolution of the bolometric luminosity with the best-fitting decay model superimposed.

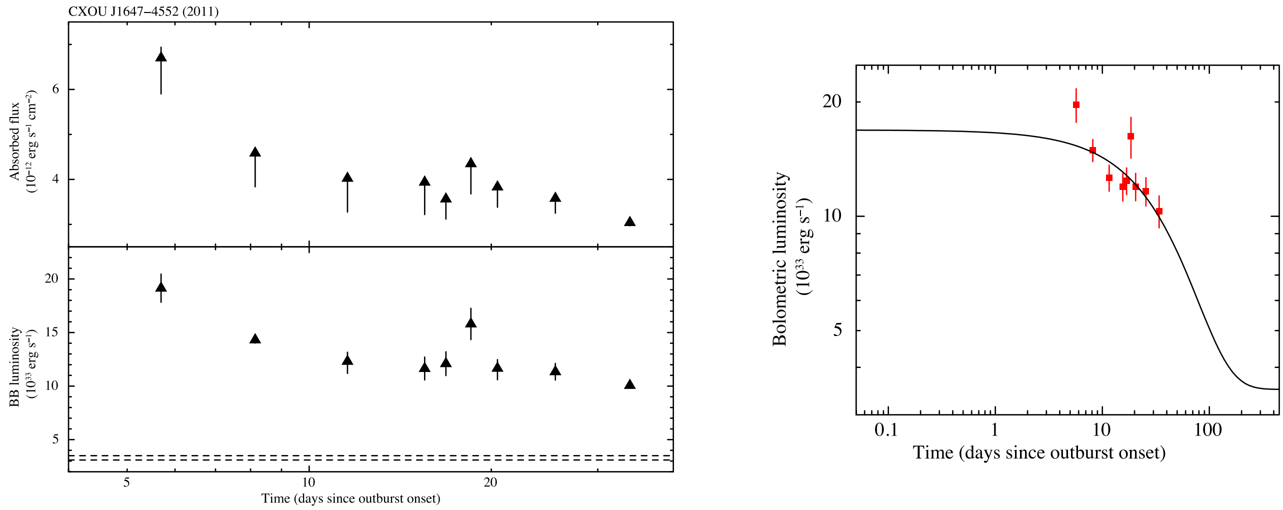

Figure D14. Left-hand panel: temporal evolution of the fluxes and luminosities for the BB model applied to the X-ray data of the 2011 outburst of CXOU J164710.2−455216. The dashed lines mark the 1σ c.l. range for the quiescent luminosity (see Table 4). A distance of 4 kpc was assumed. Right-hand panel: temporal evolution of the bolometric luminosity with the best-fitting decay model superimposed.

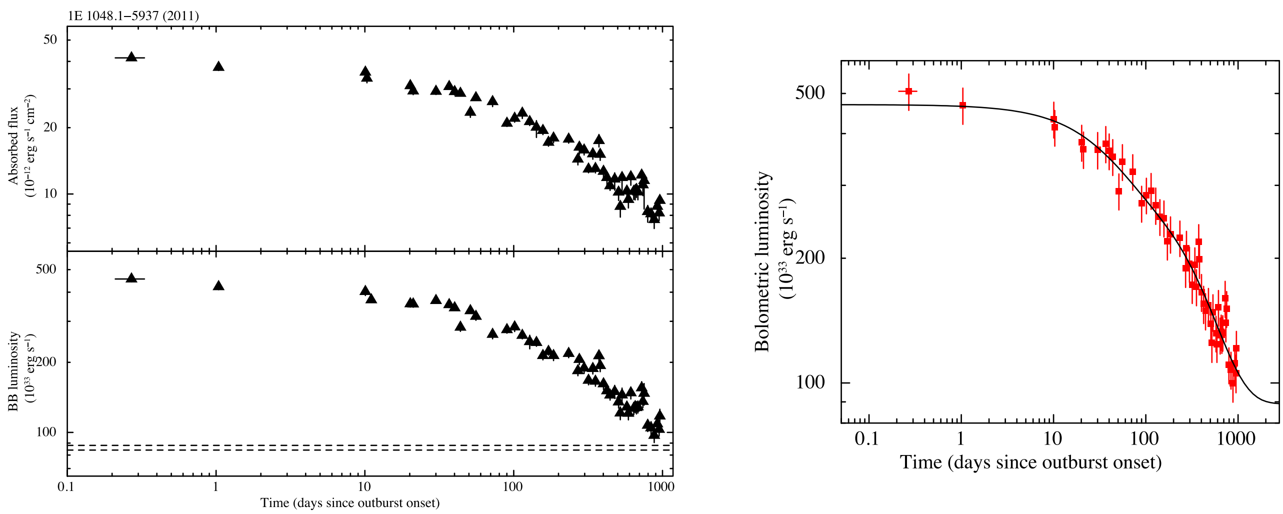

Figure D15. Left-hand panel: temporal evolution of the fluxes and luminosities for the BB model applied to the *Swift* XRT data of the 2011 outburst of 1E 1048.1−5937. The dashed lines mark the 1σ c.l. range for the quiescent luminosity (see Table 4). A distance of 9 kpc was assumed. Right-hand panel: temporal evolution of the bolometric luminosity with the best-fitting decay model superimposed.

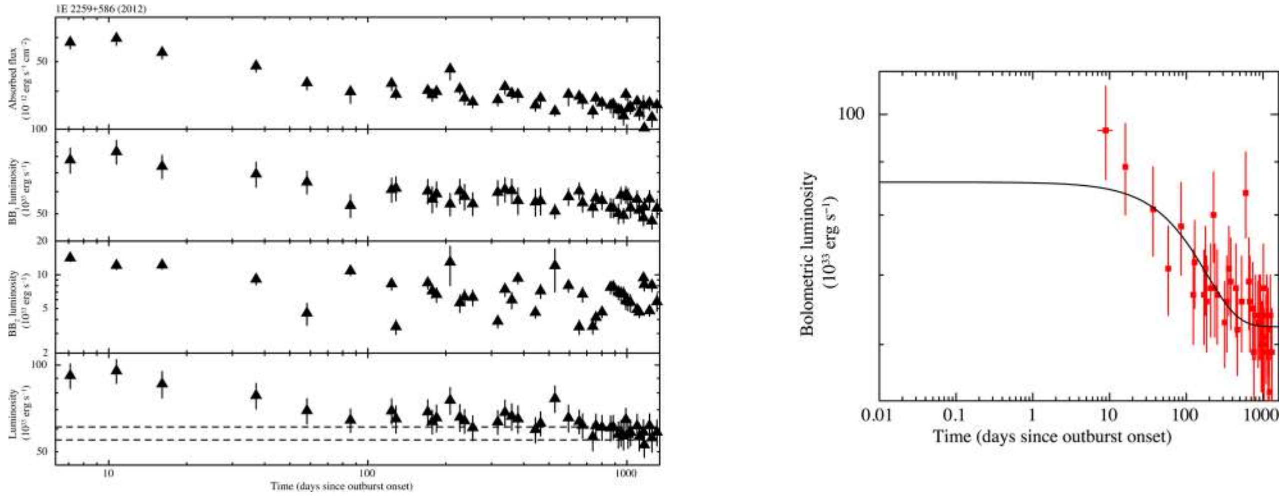

Figure D16. Left-hand panel: temporal evolution of the fluxes and luminosities for the 2BB model applied to the *Swift* data of the 2012 outburst of 1E 2259+586. The dashed lines mark the 1σ c.l. range for the quiescent luminosity (see Table 4). energy range. A distance of 3.2 kpc was assumed. Right-hand panel: temporal evolution of the bolometric luminosity with the best-fitting decay model superimposed.

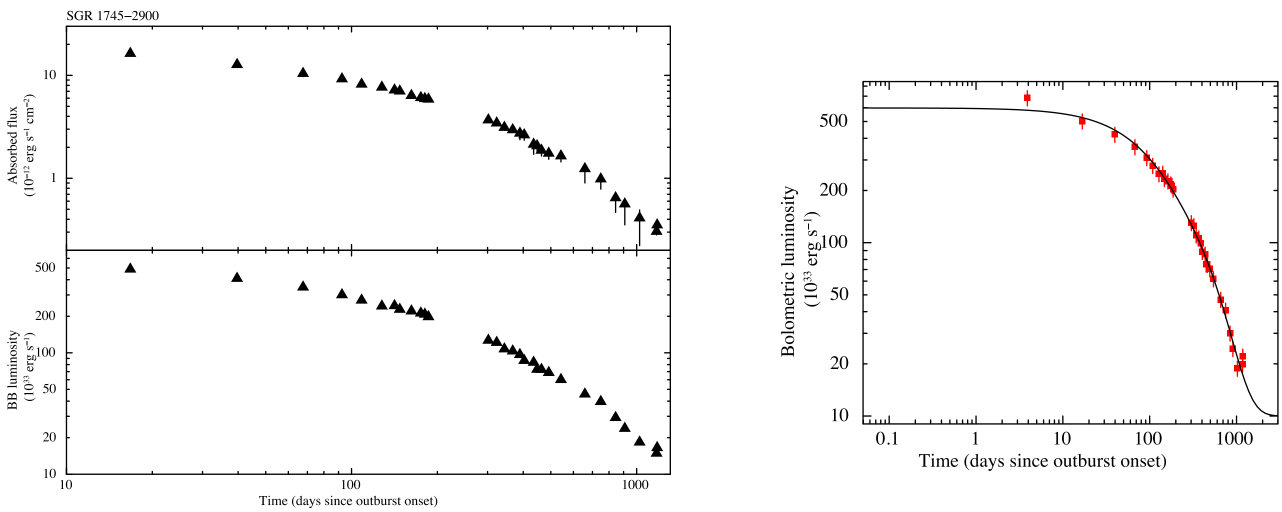

Figure D17. Left-hand panel: temporal evolution of the fluxes and luminosities for the BB+PL model applied to the *Chandra* data of the outburst of SGR 1745−2900. A distance of 8.3 kpc was assumed. Right-hand panel: temporal evolution of the bolometric luminosity with the best-fitting decay model superimposed.

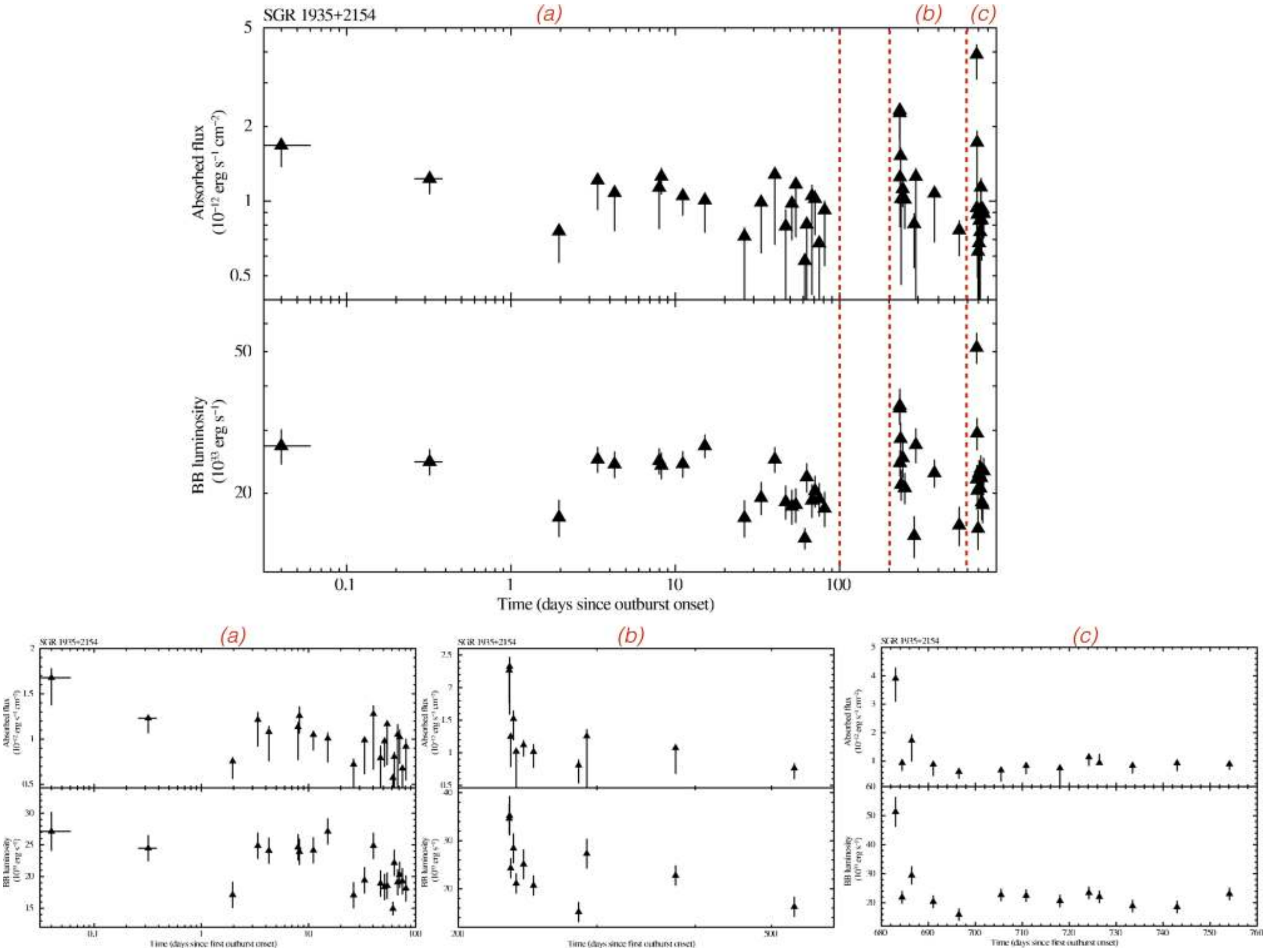

Figure D18. Temporal evolution of the fluxes and luminosities for the BB model applied to the *Swift* XRT data of the outbursts of SGR 1935+2154 (see the bottom panels for a zoom on the individual outbursts). A distance of 9 kpc was assumed (see Israel et al. 2016). The quiescent level is unknown.

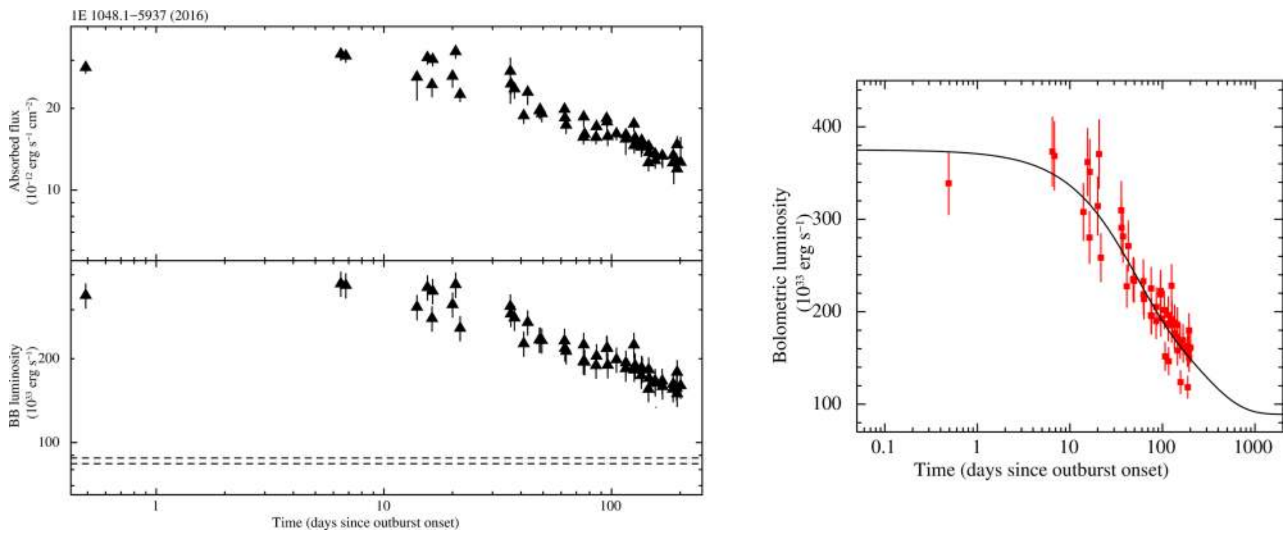

Figure D19. Left-hand panel: temporal evolution of the fluxes and luminosities for the BB model applied to the *Swift* data of the 2016 outburst of 1E 1048.1−5937. The dashed lines mark the 1σ c.l. range for the quiescent luminosity (see Table 4). A distance of 9 kpc was assumed. Right-hand panel: temporal evolution of the bolometric luminosity with the best-fitting decay model superimposed.

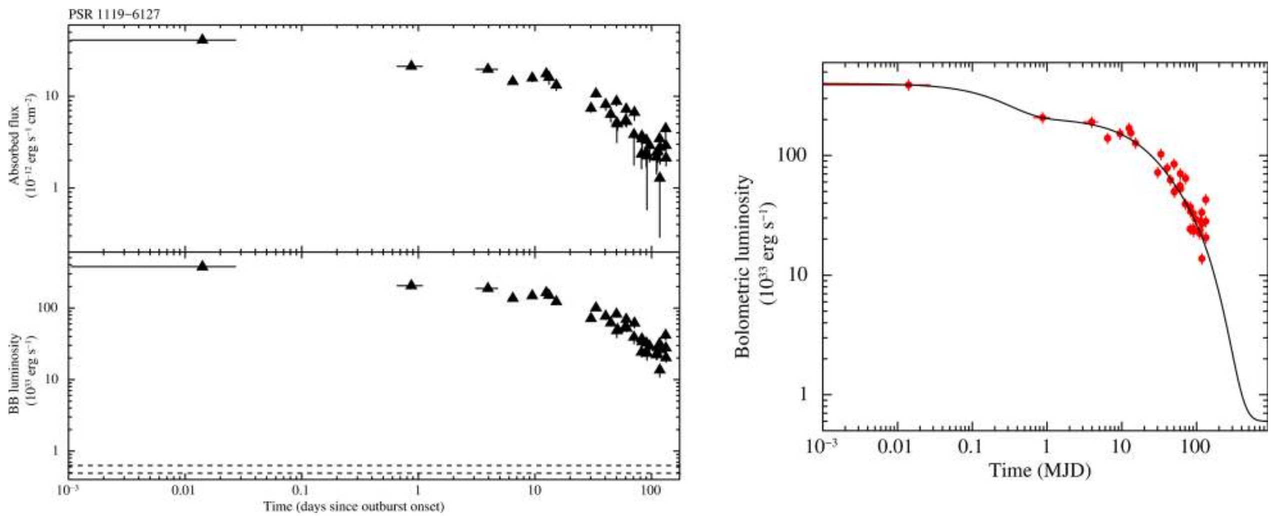

Figure D20. Left-hand panel: temporal evolution of the fluxes and luminosities for the BB model applied to the *Swift* XRT data of the outburst of PSR J1119−6127. The dashed lines mark the 1σ c.l. range for the quiescent luminosity (see Table 4). A distance of 8.4 kpc was assumed. Right-hand panel: temporal evolution of the bolometric luminosity with the best-fitting decay model superimposed.

This paper has been typeset from a TEX/LATEX file prepared by the author.